FRP-Concrete Hybrid Composite Girder Systems: Web Shear Strength and Design Guide Development

Final Project Report

08/31/2022

Andrew Schanck PE, PhD
Research Engineer, University of Maine Civil Engineering

Jacob Clark EI
Research Engineer, University of Maine Civil Engineering

William G. Davids, PhD, PE
Bodwell University Distinguished Professor of Civil and Environmental Engineering, University of Maine

Advanced Structures and Composites Center
35 Flagstaff Rd
University of Maine
Orono, ME 04469

Telephone: 207-581-2123
FAX: 207-581-2074
composites@maine.edu
www.composites.umaine.edu

ACKNOWLEDGEMENTS

Support for this research was provided by the Transportation Infrastructure Durability Center (TIDC) at the University of Maine under grant 69A3551847101 from the U.S. Department of Transportation's University Transportation Centers Program. Additional financial and logistical support was provided by AIT Bridges, whose assistance with specimen manufacturing is greatly appreciated. The results and opinions reported here are solely those of the authors and do not constitute a design guide or specification.

DISCLAIMER

Table of Contents

Index of Figures

Index of Tables

1 Introduction

Durable, reliable infrastructure is vital for local, state, and national economic growth and development. As the economy grows, so too do the demands placed on existing infrastructure, notably on roads and bridges. To keep up with the ever-increasing demand, new, durable, rapidly erected bridges are needed. Increasingly, these bridges utilize new materials and construction techniques to improve durability, reduce construction costs, and speed erection. To respond to this need, the University of Maine developed a novel, fiber reinforced polymer (FRP) tub girder (referred to as a "CT girder") for use in new bridge construction as an alternative to conventional steel and prestressed concrete structural members (Dagher et al. 2019; Davids et al 2022a, 2022b; Davids & Schanck 2022). CT girders have been identified as a promising technology to support sustainable and durable infrastructure development, as they are comparatively light and overcome many of the challenges associated with precast NEXT beam concrete structures by reducing shipping costs and camber variability caused by prestressing. Commercialization of this technology is underway, with the evaluation of the first CT girder bridge constructed for regular traffic, the Hampden Grist Mill Bridge (HGMB) completed (Davids and Schanck 2022), two more bridges to be completed this year, and other bridges in the design or pre-construction stage.

To more fully characterize the CT girder's behavior and to advance its acceptance and implementation in future bridge projects, two specific aspects of behavior and design must be addressed. First, a more complete picture of the CT girder system's web material shear strength must be established by experimental testing. Although previous testing has verified the models and assumptions used in flexural design (Davids et al. 2022a, 2022b, Diba & Hepler, 2019), no such testing has been successfully performed with regards to shear strength. Of particular importance, CT girder webs' composite fabric architecture and sandwich foam core design make strength estimation by conventional test methods challenging, leading to uncertainty in the level of conservatism in shear design. Web buckling capacity is also difficult to estimate with conventional calculations and tools available to most engineers. This project more accurately quantifies both web shear strength and buckling resistance through the shear testing of typical foam-core webs used in CT girders and via finite-element analysis.

Second, uniform procedures and recommendations for design must be created and ultimately accepted as a design code. This will both ensure consistency of future designs and provide engineers with the guidance required to assess the use of the CT girder for different applications. To this end, a basic design guide modeled after a typical American Association of State Highway and Transportation Officials (AASHTO) guide specifications has been drafted. This guide addresses design for load effects on CT girders such as moment and shear, as well as girder-deck connection and control of deflections. Importantly, appendices are also provided with detailed examples for design of CT girders using this guide. The intention is for this guide to serve as the basis for a future, official design guide for CT girder structures that can be developed under a university-industry partnership.

This final report consists of two primary sections. Section 2 details the experimental program run to better quantify web shear strength and puts the results of the tests in the context of CT bridge girders analysis and design. Section 3 contains the draft design guide. Included are results of 3D FE simulations of web buckling in the form of easily used design nomographs. Details of the FE simulations are provided in an Appendix.

2 FRP Foam-Core Web Shear Testing and Analysis

2.1 Introduction

The webs of a CT girder are assumed to provide the vast majority of its resistance to bending shear, and to maintain adequate distance between the lower flange and deck to develop adequate bending strength. For this reason an accurate prediction of the webs' shear strength and resistance to shear buckling is crucial to a safe and efficient CT girder design. CT girder webs are designed as a sandwich of thin glass fiber reinforced polymer (FRP) composite face sheets on either side of a thick foam core. The face sheets provide the web with in-plane strength, while the core separates the face sheets to increase resistance to out-of-plane movement and web buckling. However, the complex fabric architecture of the face sheets and the interaction between the face sheets and core make shear strength and buckling predictions challenging or impossible using conventional analytical techniques. To overcome these challenges, samples of CT girder webs were tested experimentally and numerically assessed to better understand their behavior.

Investigation of the shear characteristics of CT girder webs proceeded in two phases to approach shear strength and buckling resistance, respectively. First, representative panel specimens of CT girder webs were constructed and tested per ASTM D8067/D8067M-17 (2017) to evaluate their shear strengths and compare with the web shear strength used previously for design by AIT Bridges (2019). After this, representative numerical models were created and analyzed using the finite element (FE) method to evaluate their shear buckling resistance and help develop methods for shear buckling design.

2.2 Experimental Web Shear Testing

2.2.1 Testing Details

To establish an accurate estimate of available CT girder web shear strength, a series of representative specimens was manufactured and tested. These tests were based upon ASTM test method D8067/D8067M-17 (2017), which will hereafter be referred to as a "picture frame test". A representative picture frame specimen can be seen mounted in a modified fixture manufactured for this testing in Figure 1. A diamond-shaped specimen is clamped between the bars of the fixture, which are connected to one another by pins allowing free rotation. Tension is applied to the top and bottom pins which, due to the fixture's geometry, is transferred diagonally to the specimen along its edges. This creates a state of stress within the specimen approaching perfect pure shear, allowing straightforward calculation of shear strength upon specimen failure and shear modulus (provided shear strain is measured).

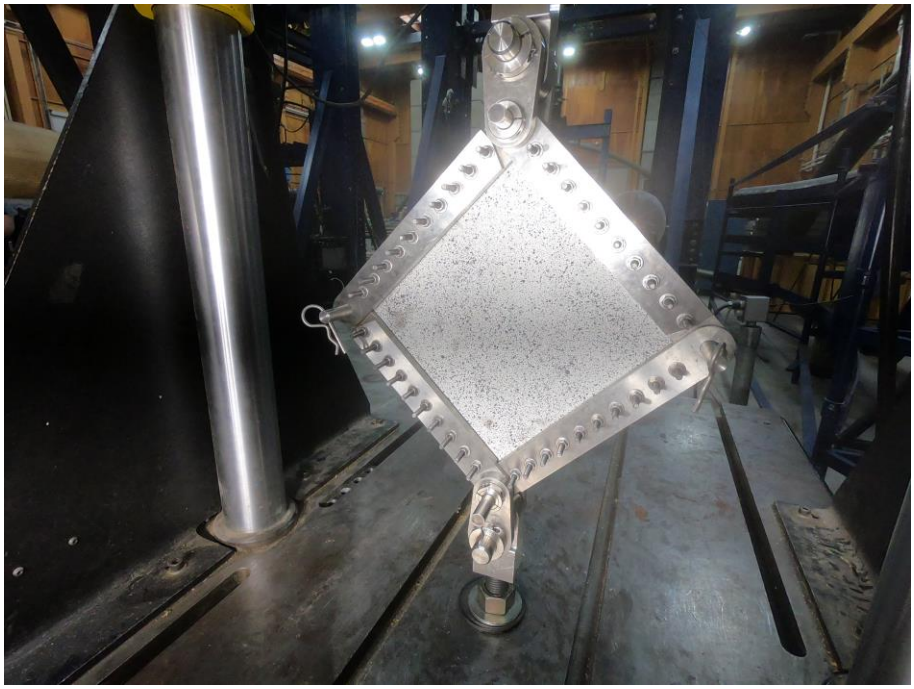

Figure 1: Picture Frame Specimen in Fixture

Preliminary analyses of the picture frame fixture established its maximum tensile capacity to equal 30 kip, and so specimens were designed to fail at or below this load with a factor of safety equal to 2. Simplified analysis of the webs making up the first, in-situ CT girder bridge (Schanck & Davids, 2021) suggested resistances in significant excess of this, and so rather than using the precise layup of that bridge's webs, representative specimens were designed using the 10 ksi shear strength assumed in the original bridge design (AIT, 209). These formed the test matrix shown in Table 1, in which both the number of laminae making up each face sheet and the thickness of the foam core were varied to give four distinct specimen variations. Six specimens were manufactured from each variation, for a total of 24 specimens, although a total of 22 were tested. Large plates utilizing the fiber architectures and sandwich layups described in Table 1 were manufactured by the vacuum infusion process by AIT Bridges. Specimens were cut from these plates by water-jetting, with attachment holes drilled by CNC. As will be explained below, later specimens were also provided with doubler plates adhered to their exterior edges to strengthen them against bearing failure around attachment holes. These were manufactured from 0.125 in. G10 fiberglass sheet and attached with PLEXUS MA300 methacylate adhesive. A specimen outfitted with doublers can be seen in Figure 2.

Table 1: Specimen Test Matrix

Specimen Code	Number of Plies per Face Sheet	Core Thickness (in.)
F2-C75	2	0.75
F2-C150	2	1.50
F4-C75	4	0.75
F4-C150	4	1.50

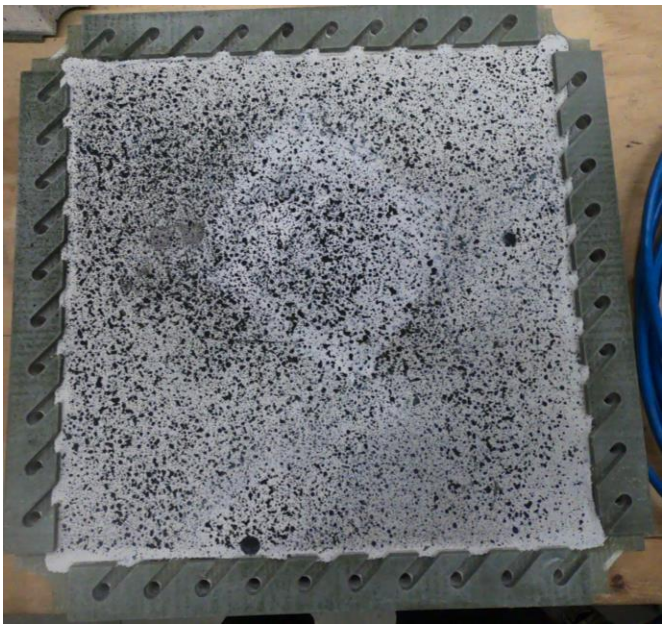

Figure 2: Specimen Outfitted with Doubler Plates

Specimens were tested in one of two Instron servo-hydraulic actuators depending on availability: a 55-kip capacity actuator mounted in a separate reaction frame, and a self-reacting 110-kip capacity actuator. These both used integrated load cells and linear variable differential transformers to record load and position data over the course of each test at a sampling rate of 2 Hz. In addition, each specimen was prepared with a stochastic, high-contrast speckle pattern for measurement by ARAMIS digital image correlation (DIC) (GOM, 2019) at a sampling rate of 1 Hz. This system automatically takes stereoscopic photographs of the specimen during testing and tracks the relative displacement of speckles between each stage. Using this system, full-field, 3-dimensional displacement and strain data were captured over the course of testing.

Numerous difficulties experienced over the course of testing required significant alterations to be made to the test fixture, the specimens, and the overall acceptance of test results. On multiple occasions during testing, the hardened steel pin at the top corner of the picture frame fixture fractured, requiring replacement and modification to the fixture itself to reduce bending stresses on the pin. Additionally, the tight tolerances to which the fixture were originally manufactured

caused significant difficulty in assembly and disassembly. This also caused frequent binding of the specimen clamping screws, requiring frequent drilling of sheared screws and rethreading of holes. To alleviate these difficulties, many of the fixture's parts were re-machined to relax tolerances and threaded holes were drilled to their respective clearance sizes, with clamping provided by nuts and washers on the fixture's exterior.

When fixture damage did not cause tests to be terminated, premature failure tended to limit the maximum loads applied to specimens, preventing determination of their full shear strength. During many tests, the bearing stress at the specimen mounting holes provided by mounting screws exceeded the face sheets' bearing strength, leading to bearing failure, with screws being pulled through the specimen. Damage from this type of failure can be seen in Figure 3. This was partially alleviated with the addition of the pre-manufactured FRP doubler plates but persisted through testing of the thinner (2-layer face sheet) specimens. It should be noted that the 4-layer face sheet specimens did not experience bearing failure, but were limited by the 30 kip capacity of the test fixture.

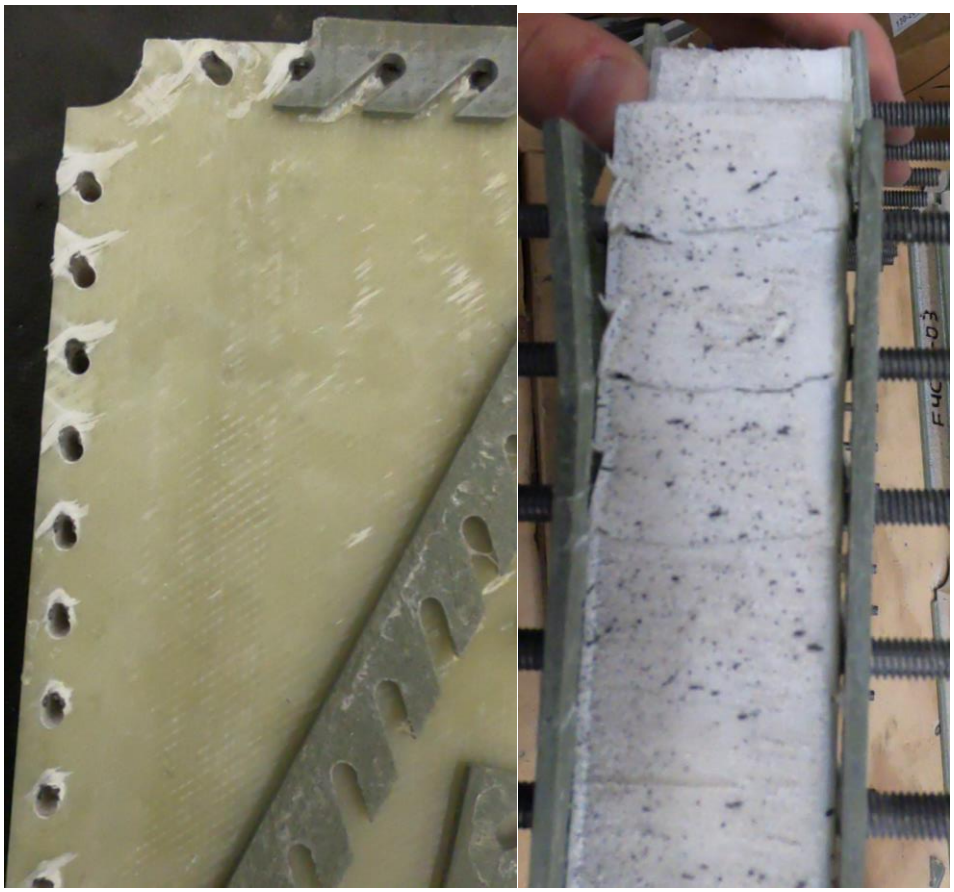

Figure 3: Damage from Bearing Failure

2.2.2 Results

Twenty-two of the original twenty-four specimens were tested using the method described above. Two specimens, both parts of the F4C150 series, were omitted from testing as all other members of the series were tested to the fixture's maximum load without failure, and a different outcome was deemed unlikely. Table 2 presents the failure mode and maximum load for each specimen tested. Additionally, the maximum shear stress experienced by each specimen is provided, which was calculated per ASTM D8067 (2017) as Equation 2.2.2-1

$$\tau_{max} = \frac{0.707 * P_{max}}{2 * t_f * L} \tag{2.2.2-1}$$

where P_{max} is the maximum recorded load during a test, t_f is the nominal thickness of one face sheet, and L is the inside distance between fixture bars.

Table 2: Picture Frame Shear Test Results

2-Lamina Face Sheets				
Specimen	Failure Mode	Doubler Plate	Maximum Load (kips)	Maximum Shear Stress (ksi)
F2C75-01	Bearing	No	17.6	13.6
F2C75-02	DNF	No	23.3	17.9
F2C75-03	Bearing	No	23.3	17.9
F2C75-04	DNF	Yes	30.0	23.1
F2C75-05	Bearing	Yes	25.9	19.9
F2C75-06	Bearing	Yes	23.7	18.3
F2C150-01	Bearing	No	23.3	17.9
F2C150-02	Bearing	Yes	26.1	20.1
F2C150-03	Bearing	Yes	24.9	19.2
F2C150-04	Bearing	Yes	22.9	17.6
F2C150-05	Bearing	Yes	23.3	17.9
F2C150-06	Bearing	Yes	23.2	17.9
		Average	24.0	18.4
		COV	11.9 %	
4-Lamina Face Sheets				
Specimen	Failure Mode	Doubler Plate	Maximum Load (kips)	Maximum Shear Stress (ksi)
F4C75-01	DNF	Yes	30.8	11.9
F4C75-02	DNF	Yes	30.0	11.6
F4C75-03	DNF	Yes	30.0	11.6
F4C75-04	DNF	Yes	30.0	11.6
F4C75-05	DNF	Yes	29.9	11.5
F4C75-06	DNF	Yes	30.0	11.6
F4C150-01	NT	-	-	-
F4C150-02	DNF	Yes	30.0	11.6
F4C150-03	NT	-	-	-
F4C150-04	DNF	Yes	30.0	11.6
F4C150-05	DNF	Yes	30.0	11.6
F4C150-06	DNF	Yes	30.0	11.6
		Average	30.1	11.6
		COV	0.86 %	

*DNF = Did not fail, NT = Not tested

Figure 4 presents load-displacement data recorded during testing of one member of each series of specimens. The load-displacement behavior of other specimens are similar. As is immediately apparent, specimens with the same face sheet thickness tended to behave very similarly to one another. For the thinner face sheet specimens, initial stiffness was comparatively low. At a load of between 15 and 18 kip, both experienced a slight drop in stiffness (presumably due to the initiation of bearing failure) leading to a maximum load between 22 and 24 kip and subsequent nonlinearity with damage progression. The thicker face sheet specimens were characterized by a higher initial stiffness wherein (after a small, initial nonlinear phase) displacement increased linearly with load up to the maximum allowable load of 30 kip. As load was thereafter released, displacement fell linearly with a stiffness similar to, but slightly higher than that of the upward path.

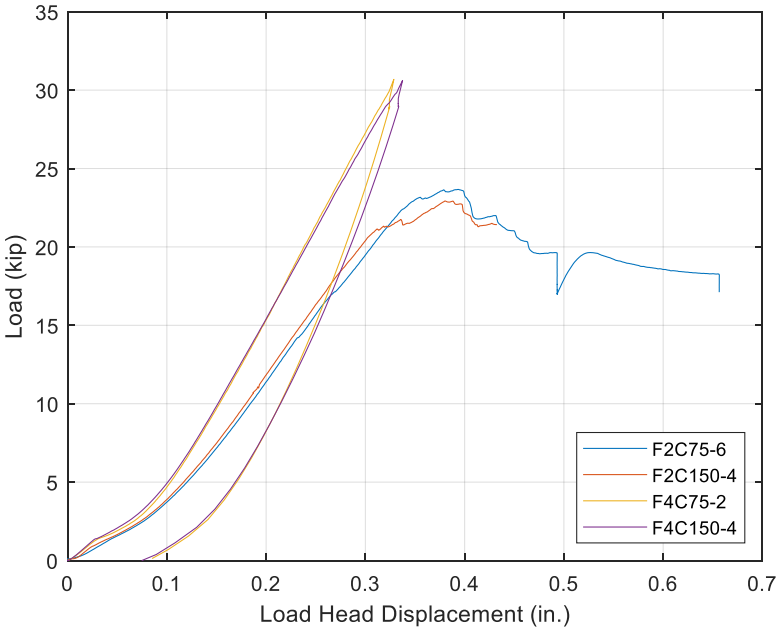

Figure 4: Load-Displacement for Each Specimen Series

As mentioned before, strain and out-of-plane displacement of each specimen under loading were measured using ARAMIS DIC (GOM, 2019). This allowed the normal and shear strain fields across the face sheet to be fully characterized, as well as any out-of-plane displacement indicating buckling. Additionally, these data were used to calculate average normal and shear strains across the face sheet. Figure 5, and Figures 6 and 7 present the measured out-of-plane displacement and calculated full-field strains for Specimen F2C75-02 at maximum load, respectively, while Figures 9 and 10 present average strains for the same specimen throughout the entire test. Plots similar to Figures 9 and 10 for each specimen can be found in Appendix A.

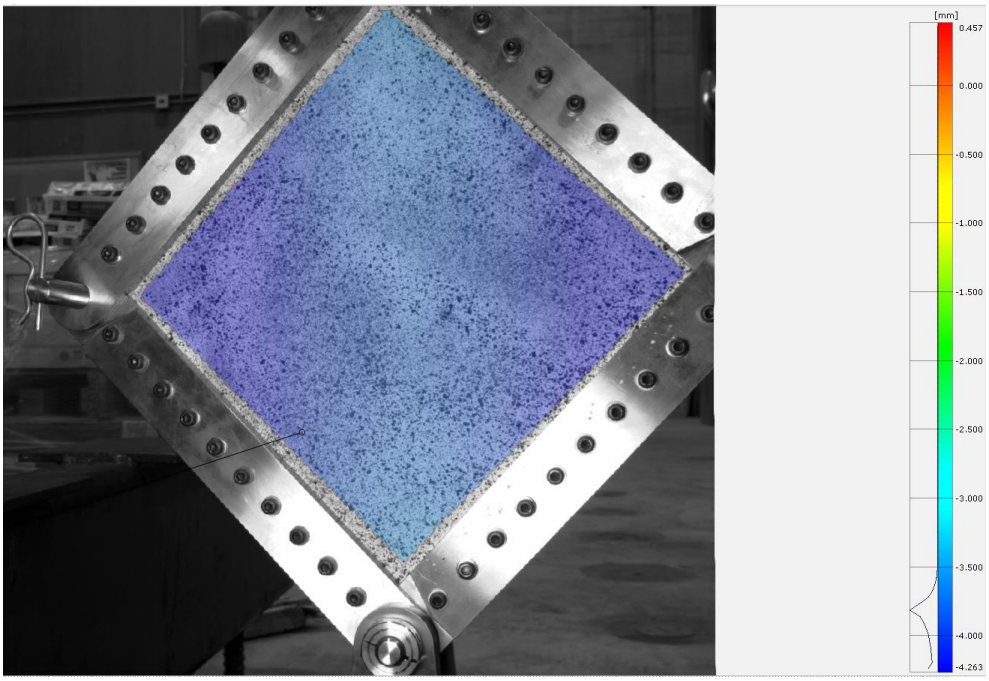

Figure 5: Specimen F2C75-02 - DIC Measured Out-of-Plane Displacement

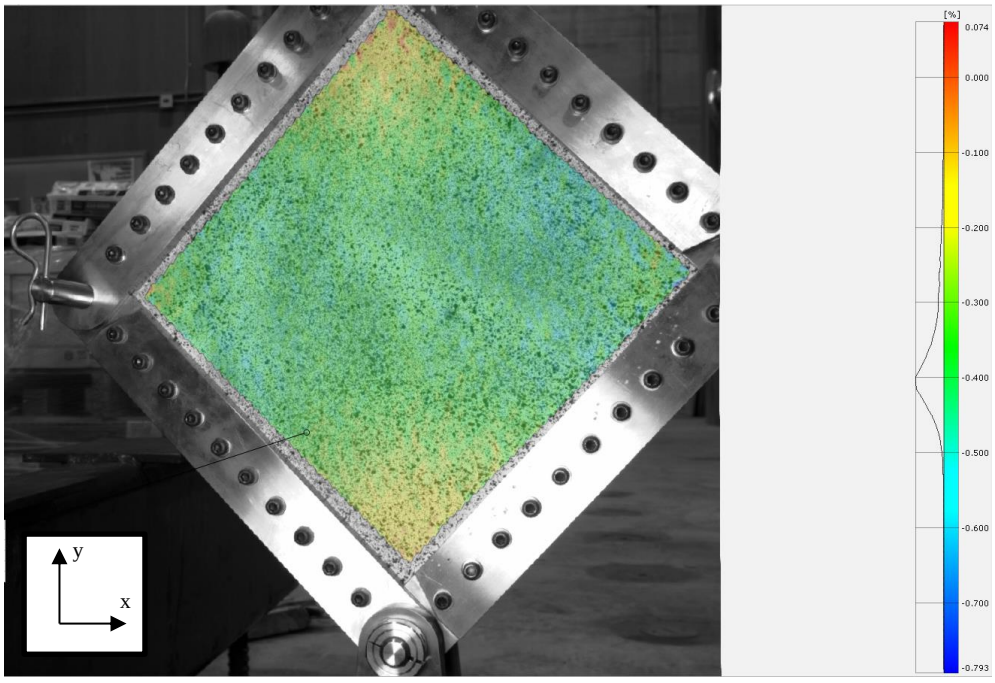

Figure 6: Specimen F2C75-02 - DIC Calculated Normal Strain in x Direction

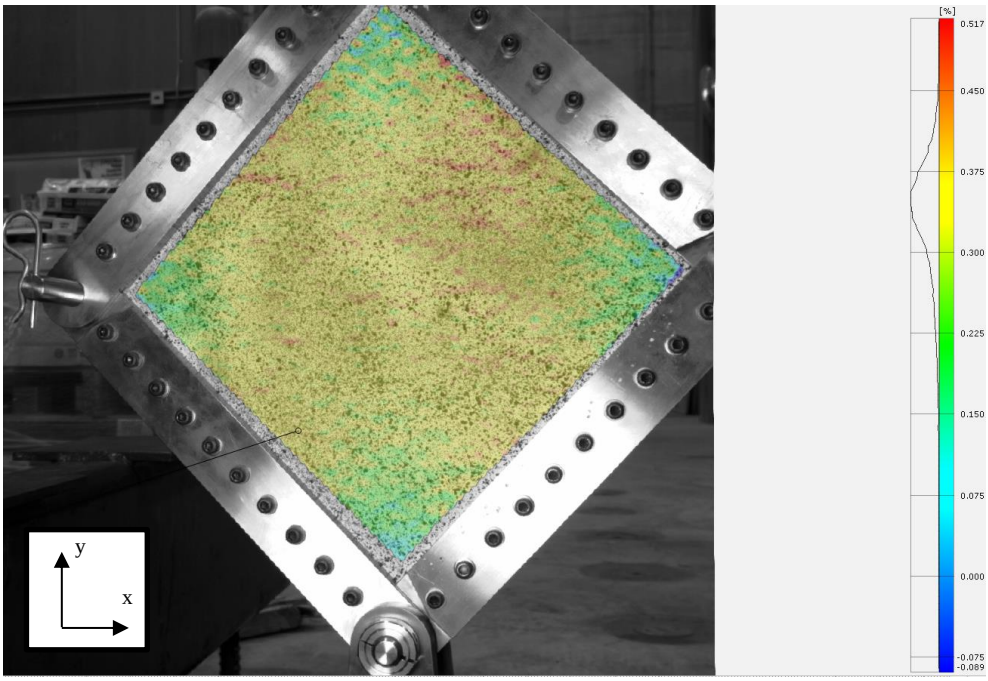

Figure 7: Specimen F2C75-02 - DIC Calculated Normal Strain in y Direction

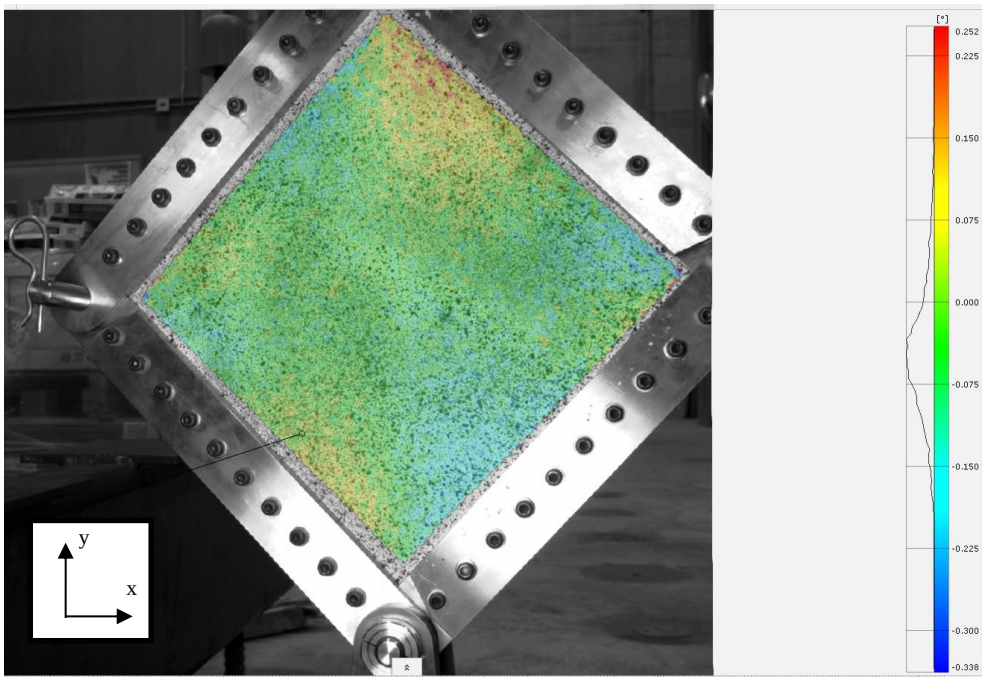

Figure 8: Specimen F2C75-02 - DIC Calculated Shear Strain

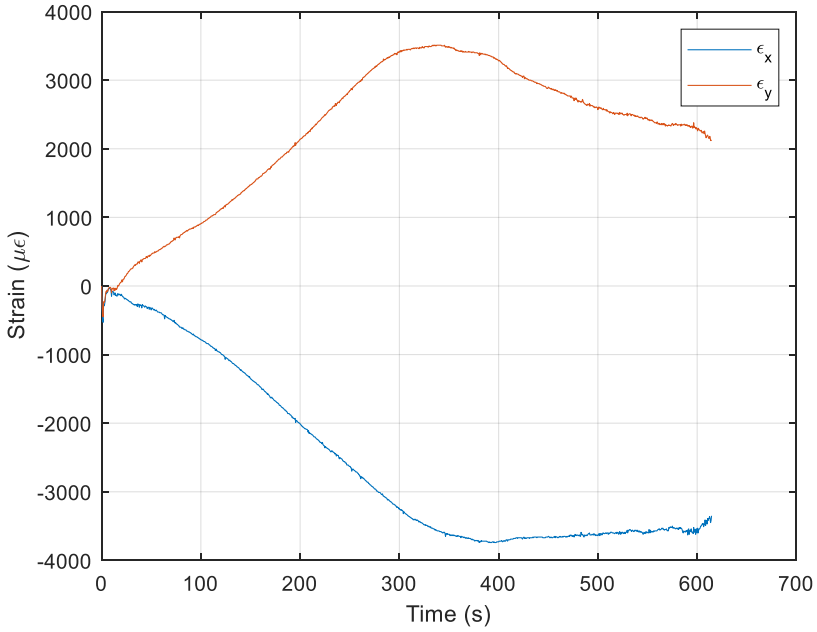

Figure 9: Specimen F2C75-02 - DIC Calculated Normal Strains

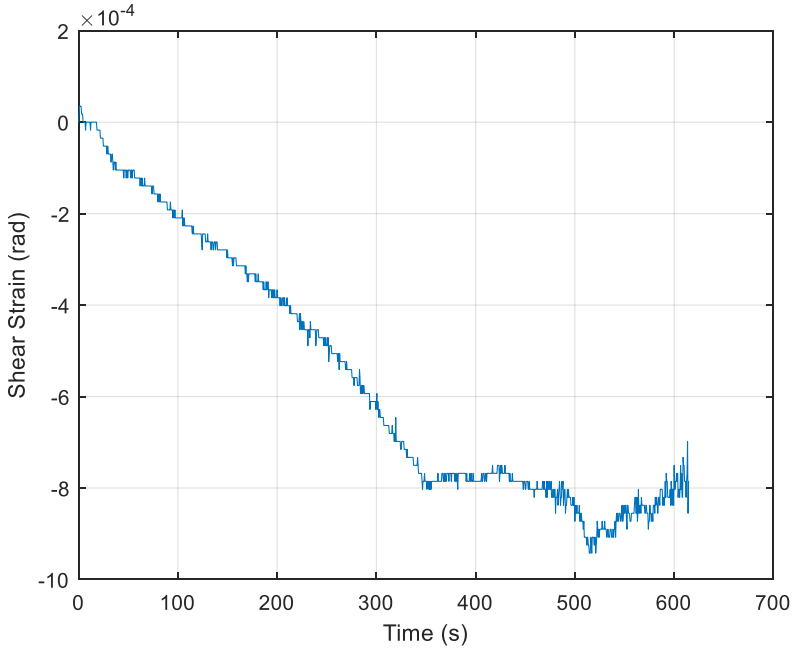

Figure 10: Specimen F2C75-02 - DIC Calculated Shear Strain

2.2.3 Discussion

Due to the numerous difficulties and oversights encountered and mentioned above, the testing performed here was unable to produce the desired failure modes (shear failure or buckling) and so no conclusions can be drawn regarding the specimens' actual, full strength. Although this

limits the conclusions that can be drawn, the results do provide useful information. First, the maximum shear stresses achieved for the thin face sheet are roughly consistent with the shear strengths found in previous studies. Table 3 lists the average glass FRP sandwich shear strengths found in three previous studies using the picture frame test and the constituent specimen materials, and compares them to the minimum and average peak shear stresses found for the thinner specimens from this study. As can be seen, the values found here are consistent with previous experience. Although true shear strengths could not be achieved, this positive comparison coupled with the fact that failure occurred in bearing, not shear, and justifies establishing a typical lower bound for mean shear strength of 18 ksi for design. It is important, however, to emphasize that this shear strength is based on results for what are believed to be essentially a defect-free material. Further, geometric imperfections and buckling could significantly reduce this value. Therefore, as is the case with any resistance used in design, appropriate reduction factors must also be applied to this strength, such as statistical, strength and environmental factors to achieve a conservative, uniform level of reliability.

Table 3: Comparison with Previous Studies

Study	Specimen Material		Reported Shear Strength (ksi)
	Face Sheet	Core	
Oludare & Toubia (2019)	E-Glass/Vinyl Ester	PVC Foam	15.7
Stoll & Johnston (2016)	E-Glass/Epoxy	PVC Foam	17.3
Morgenthaler et al. (2005)	E-Glass/Epoxy	PVC Foam	17.7
Present Study	E-Glass/Vinyl Ester	PVC Foam	13.6 (Min), 18.4

The load-displacement data presented in Figure 4 reveals some notable, additional behavior of the specimens relative to each other and more broadly. As would be expected, the specimens with thicker face sheets exhibited a stiffer response to loading than those with the thinner face sheets. However, the load-displacement response of specimens with the same face sheet but different core thickness was essentially identical in both cases. Between FxC75 and FxC150 specimens, the thickness of core is doubled, but the specimens' behavior remains essentially unchanged. This confirms the common assumption that, for sandwich structures the core does not contribute at all to the resistance of in-plane shear.

The displacements measured and strains calculated using DIC confirm that the specimens behave as expected under load. The relatively uniform out-of-plane displacements shown in Figure 5 confirm that the specimen does not experience shear buckling under the applied loads. The strains calculated and presented in Figures 6 through 10 present a fairly uniform state of strain and indicate that the specimen is undergoing near-pure shear. In the measured orientation, the "x" and "y" strains are close to equal to one another in magnitude and opposite in sign, and the shear strain is relatively negligible. This indicates that the normal strains are principal strains and the specimen

is oriented at its principal angle. If rotated 45 degrees, the specimen would be oriented to maximize shear strain – thus the specimen is in a state of near-pure shear.

2.3 Finite Element Simulation of Web Shear Testing

To build on the insight gained through experimental testing, a series of finite element (FE) models were created and analyzed. Two types of analyses were performed: stress analyses and Eigenvalue buckling analyses. The stress analyses were meant to directly replicate the experimental tests performed and reported upon above. The results of these analyses, when compared with actual test results, were intended to reveal additional insight into the specimens' behavior that could not easily be ascertained from the test results alone. The buckling analyses were performed to investigate the specimens' share buckling behavior, as well as to inform the design of future CT girder web sections. It must be emphasized that buckling analyses were only performed for models of the 12 in. by 12 in. test specimens and buckling loads can be expected to decrease for deeper girder webs.

2.3.1 Model Description and Development

Modeling and analysis were performed within the commercial FE software, *ABAQUS* (2019) due to its availability and capabilities. To increase the overall accuracy of predictions, the specimens' face sheets and core were modeled discretely rather than having properties smeared unto a single shell or solid section. Face sheets were modeled using S8R quadratic, reduced integration shell elements with eight nodes and six degrees of freedom per node. These elements were assigned a "composite layup" material definition, which integrates plane-stress layer constitutive behavior and laminar orientation through the element's thickness. Rather than modeling the biaxial laminae directly, two layers of unidirectional glass were modeled with lamina oriented at ±45°. The core was modeled with C3D20R quadratic continuum elements with twenty nodes and three degrees of freedom per node. These elements were assigned orthotropic constitutive behavior based on the material properties of the core material. However, this was done only to specify a shear modulus that was independent of the elastic modulus and Poisson's ratio, with no actual directional dependence on properties. The material properties used are provided in Table 4. The face sheets were attached to the core by kinematic constraints.

Table 4: Material Properties

Material	E_1 (ksi)	E_2 (ksi)	E_3 (ksi)	υ_{12}	υ_{13}	υ_{23}	G_{12} (ksi)	G_{13} (ksi)	G_{23} (ksi)
Laminae (Vectorply, 2015)	5340	1620	-	0.27	-	-	770	770	770
Core (Airtex, 2020)	16.0	16.0	16.0	0.30	0.30	0.30	3.19	3.19	3.19

To determine an appropriate level of discretization, a convergence study was performed. This study varied the number of elements making up each component (face sheets and core) while tracking maximum displacement magnitude under the specified loading and boundary conditions for stress analyses as described below. The results of this study can be seen in Figure 11. The final discretization uses 1132 elements for each face sheet and 2000 elements for the core, for a total of 4264 elements per model. A meshed model can be seen in Figure 12. It should be noted that because the face sheets use shell elements, they do not appear to be separated from the core elements. The models were analyzed under both monotonic static loads and under Eigenvalue buckling. As these analyses required separate considerations for loading and boundary conditions, these will be discussed separately.

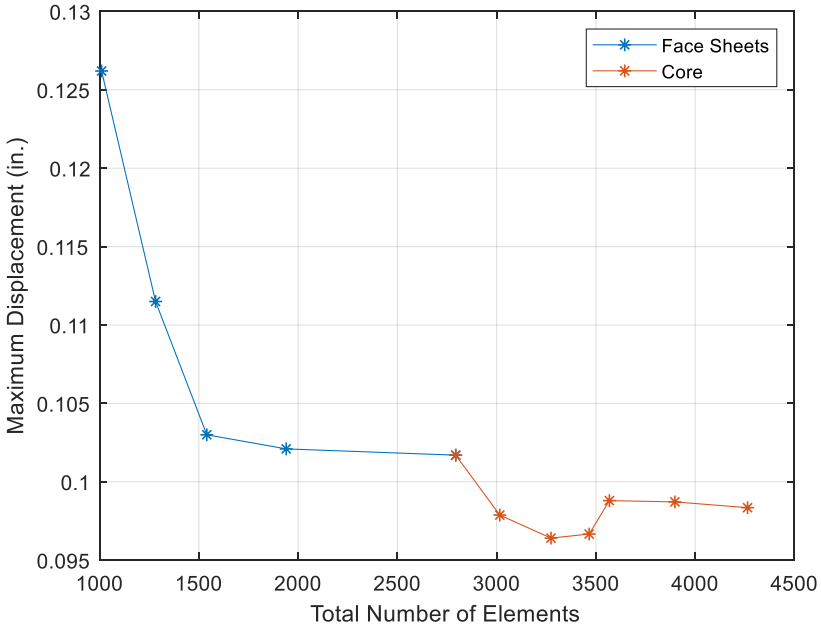

Figure 11: Discretization Convergence Study

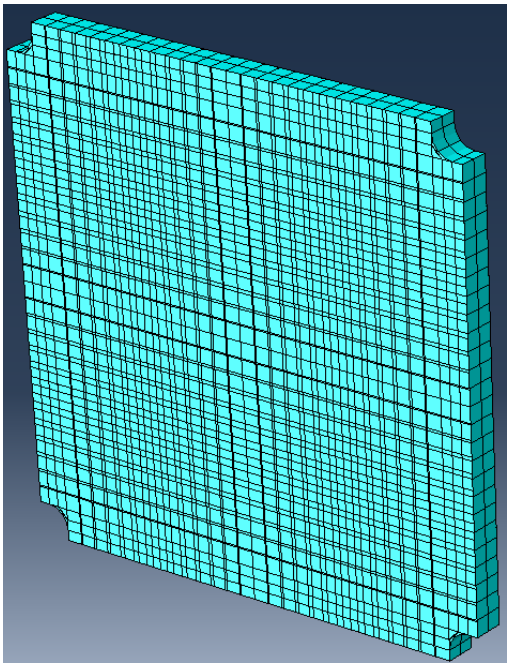

Figure 12: Meshed Panel Model

2.3.2 Stress Analysis

The stress analysis models' loading and boundary conditions were assigned to accurately mimic the conditions of testing, while also remaining computationally tractable. Rather than applying these directly, reference nodes were created at the specimens' upper and lower corners to which loads and boundary conditions were applied. The reference nodes at the specimens' bottom corners were fixed against all displacements and rotations, while the reference nodes at the specimens' top corners were fixed against all rotations and displacements except those in the direction of loading. Concentrated loads were applied to the top reference nodes in their free directions such that their vector sum was equivalent to loading during testing. Loads and restraint from boundary conditions were transferred to the specimens by kinematically constraining the degrees of freedom of the face sheets along the attachment lines to those of the reference nodes. These models were analyzed using a standard Newton-Raphson iterative solver.

The results of analyses can be compared with data collected during testing of the actual specimens. This not only can provide insight into the specimens' behavior, but also allow evaluation of the models' accuracy. Figures 13 through 16 present the predicted out-of-plane deflection, maximum in-plane principal strain, minimum in-plane principal strain, and shear strain for the model of specimen F2C75-02. These can be both qualitatively and quantitatively compared with Figures 5-8 respectively. Note that the results shown in Figures 13 through 16 should be rotated 45 degrees clockwise to match the testing configuration. Figure 13 shows the model's predicted out-of-plane displacement. Qualitatively, this appears similar to the measured displacement shown in Figure 5, with highest displacement occurring along the line-of-action of loading. However, where Figure 5 indicates a displacement of around 0.15 in., the model predicts

displacements between 0.00025 and 0.0006 in. (effectively no out-of-plane displacement). This may indicate that the model predicts too stiff a response in the out-of-plane direction from the core material. This does not seem to affect the stress models' other predictions, but should be considered when examining the results of buckling analyses.

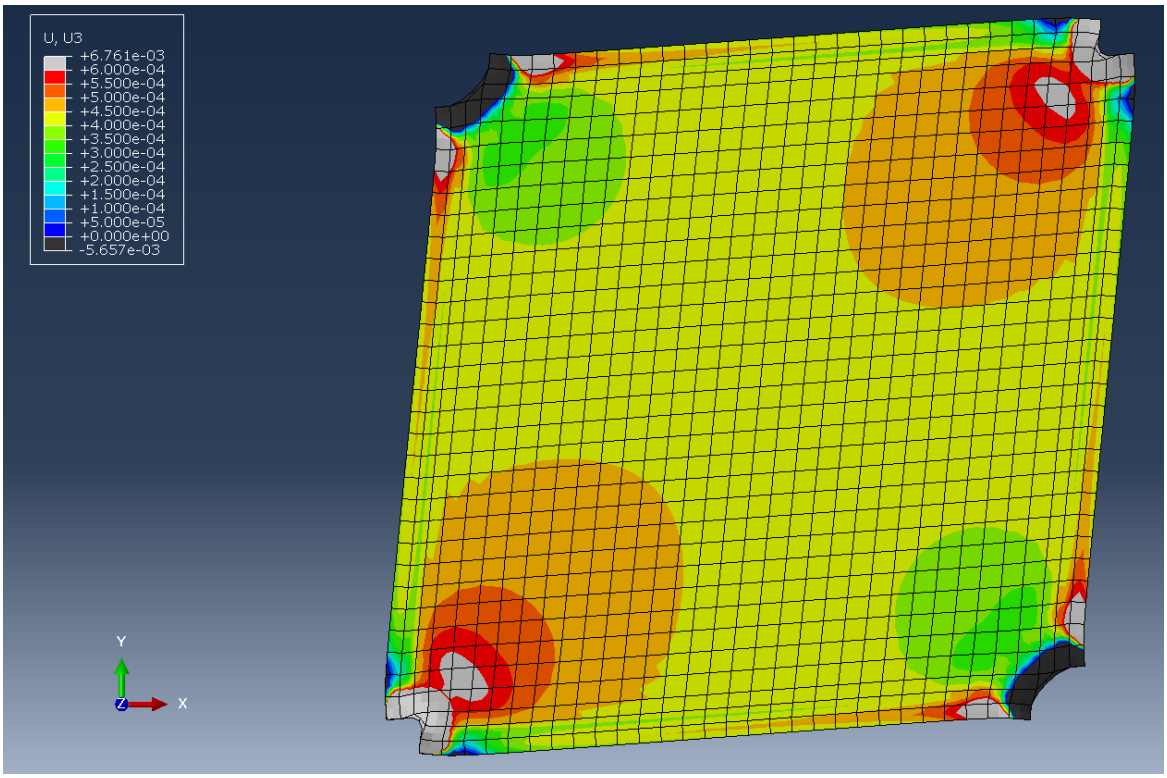

Figure 13: F2C75-02 FE Predicted Out-of-Plane Displacement

Figures 14 through 16 show predicted maximum in-plane principal strain, minimum in-plane principal strain, and shear strain, respectively, and can be compared directly with Figures 6, 7, and 8. Again, these strain fields compare well qualitatively. However, they also compare relatively well quantitatively. The predicted principal strains at the model's center node are ±4560 με with a shear strain of 0.00 rad, whereas the real specimen's calculated strains in the y and x directions were around ±3700 με with a shear strain of -0.0008 rad. This shows that the model's prediction of face sheet stiffness is reasonably accurate if somewhat low. Table 5 presents similar comparisons of measured and predicted out-of-plane displacement and in-plane strains for other specimens which show the same general trends with the exception of a few outliers.

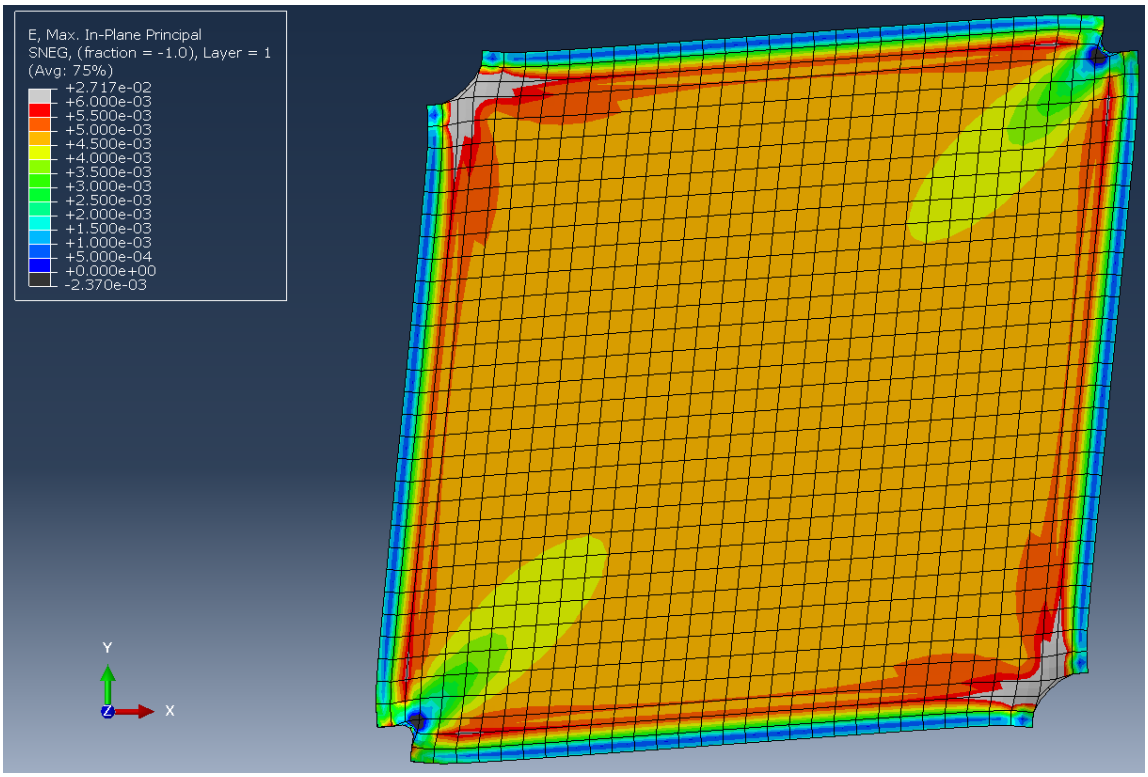

Figure 14: F2C75-02 FE Predicted Maximum in-Plane Principal Strain

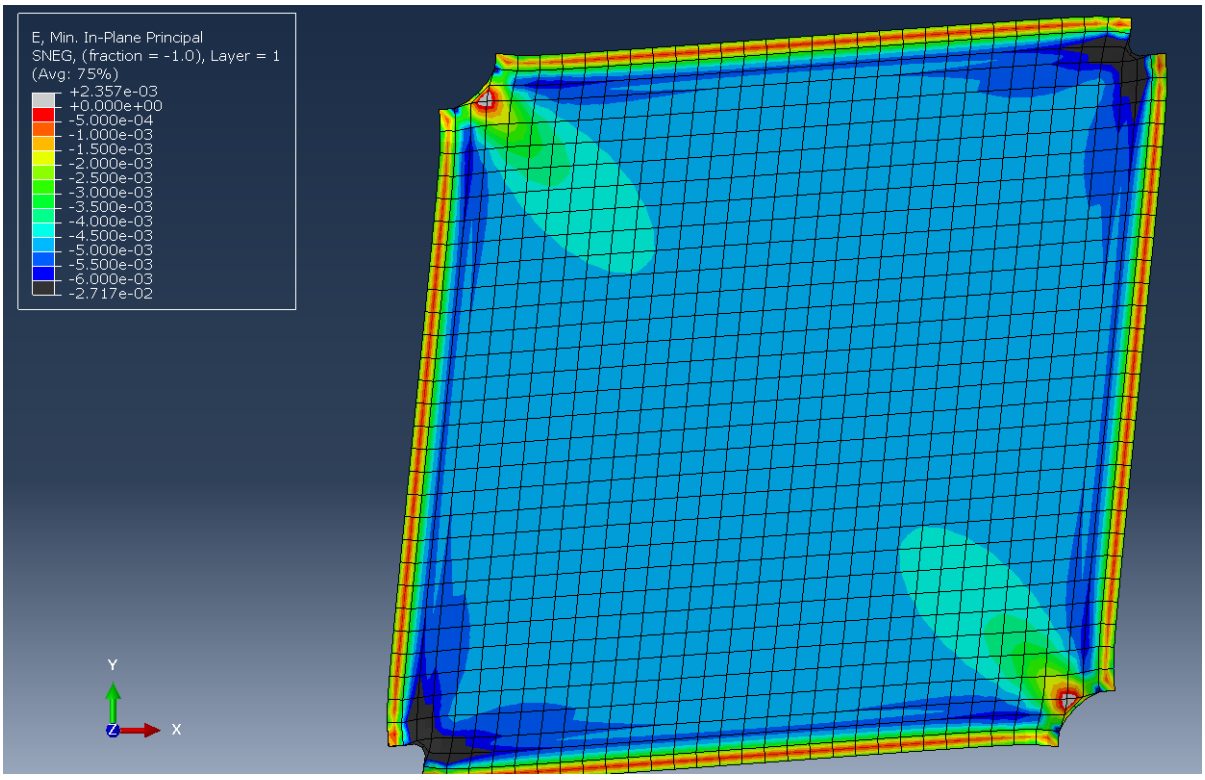

Figure 15: F2C75-02 FE Predicted Minimum in-Plane Principal Strain

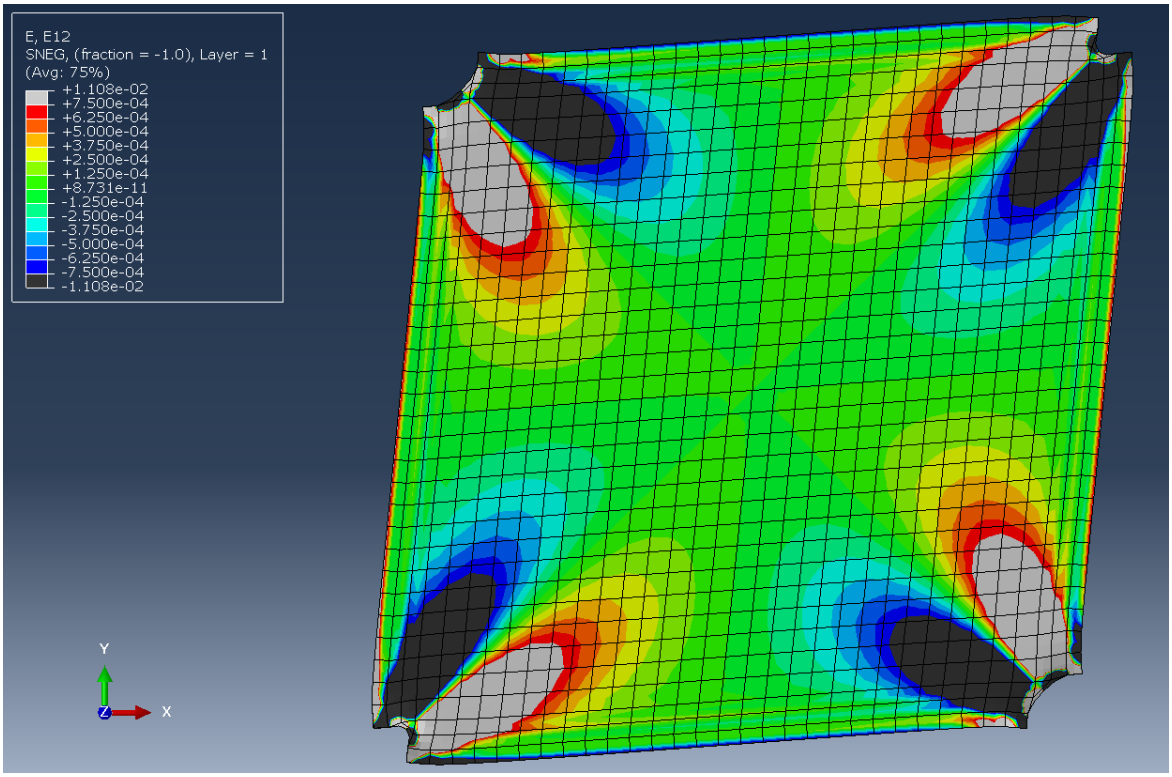

Figure 16: F2C75-02 FE Predicted Shear Strain

Table 5: Comparison of Test Specimens and FE Model Results

Specimen	Out-of-Plane Displacement (in.)		Maximum Principal Strain (με)		Minimum Principal Strain (με)		Shear Strain (rad*10^{-4})	
	Test	FE	Test	FE	Test	FE	Test	FE
F2C75-01	0.011	0.0003	2750	3450	-2680	-3450	0.70	0.000
F2C75-02	-0.150	0.0004	3480	4560	-3740	-4560	6.28	-0.000
F2C75-03	-0.079	0.0004	3560	4560	-3320	-4560	0.52	-0.000
F2C75-04	-0.079	0.0006	5440	5880	-5110	-5880	-1.22	-0.002
F2C75-05	-0.070	0.0005	3820	5070	-3750	-5070	3.84	-0.001
F2C75-06	-0.122	0.0004	4070	4640	-3370	-4640	1.92	-0.001
F2C150-01	-0.031	0.0006	3400	4490	-4080	-4490	-4.53	0.002
F2C150-02	-0.041	0.0006	4540	5030	-4330	-5030	-3.14	0.002
F2C150-03	0.003	0.0006	4530	4800	-3820	-4800	0.698	-0.002
F2C150-04	0.040	0.0006	3970	4420	-3800	-4420	0.872	0.000
F2C150-05	0.018	0.0006	7130	4480	-1240	-4480	-28.6	-0.002
F2C150-06	0.045	0.0006	3250	4480	-3310	-4480	2.97	-0.002
F4C75-01	0.018	0.0002	2120	3030	-1810	-3030	3.45	-0.004
F4C75-02	0.060	0.0002	3160	2950	-3020	-2950	-3.84	-0.010
F4C75-03	0.010	0.0002	2750	2950	-2630	-2950	-0.873	-0.010
F4C75-04	0.041	0.0002	2820	2950	-2950	-2950	-1.22	-0.010
F4C75-05	0.027	0.0002	2880	2940	-2720	-2940	-2.62	0.010
F4C75-06	0.031	0.0002	2860	2950	-2770	-2950	-2.62	-0.010
F4C150-02	0.010	0.0003	2670	2920	-2670	-2920	0.00	-0.006
F4C150-04	-0.036	0.0003	2780	2920	-2390	-2920	1.05	-0.006
F4C150-05	0.049	0.0003	3160	2920	-2860	-2920	-2.09	-0.006
F4C150-06	0.060	0.0003	2360	2920	-2240	-2920	0.349	-0.006

2.3.3 Buckling Analysis

The models analyzed for shear buckling were similar to the stress analysis models in constitutive behavior and kinematic constraint of face sheets and core, and discretization. However, several changes were made to the model formulation to facilitate analysis and extraction of buckling load and modes. First, the geometry of the models was altered slightly by removing a small amount of material from each of the edges. This allowed loads and boundary conditions to

be applied directly to the face sheets along the attachment lines rather than by kinematic constraint to reference nodes. All face sheet edges were restrained from out-of-plane displacement, and the central node of each face sheet was restrained against rotation about the axis normal to the plane of the face sheet. Additionally, the bottom and left-hand edges of the face sheets were restrained against displacement in the horizontal and vertical directions, respectively. A unit shear stress resultant load was applied to the top and right-hand edges. This, in combination with the displacement boundary conditions, applied pure shear conditions. The models were solved using a subspace algorithm Eigensolver, with the critical shear buckling load-per-unit-thickness taken as twice the resulting Eigenvalue to account for the fact that unit loads were applied separately to each face sheet.

Models with composite and sandwich layups mimicking the four types of specimen tested experimentally were analyzed, with resulting critical buckling load-per-unit-thickness, $N_{xy,cr}$ given in Table 6, along with the corresponding critical buckling loads, P_{cr} and critical buckling shear stresses, τ_{cr}. Additionally, it is noted whether the predicted buckling mode was a global mode or a local wrinkling mode. Examples of these buckling modes are shown in Figure 17. As can be seen, increases in core thickness tended to increase critical buckling load and stress, whereas increases in face sheet thickness tended to increase critical buckling load but decrease critical buckling stress. This implies that, as the thickness of the face sheets increases, the core's ability to restrain face sheet buckling decreases due to a reduced relative stiffness.

Table 6: Base Buckling Analysis Results

Model	$N_{xy,cr}$ (kip/in)	P_{cr} (kip)	τ_{cr} (ksi)	Mode Type
F2C75	3.19	51.9	33.3	Global
F2C150	4.32	70.3	45.0	Local
F4C75	4.45	72.5	23.2	Global
F4C150	7.15	116.3	37.2	Global

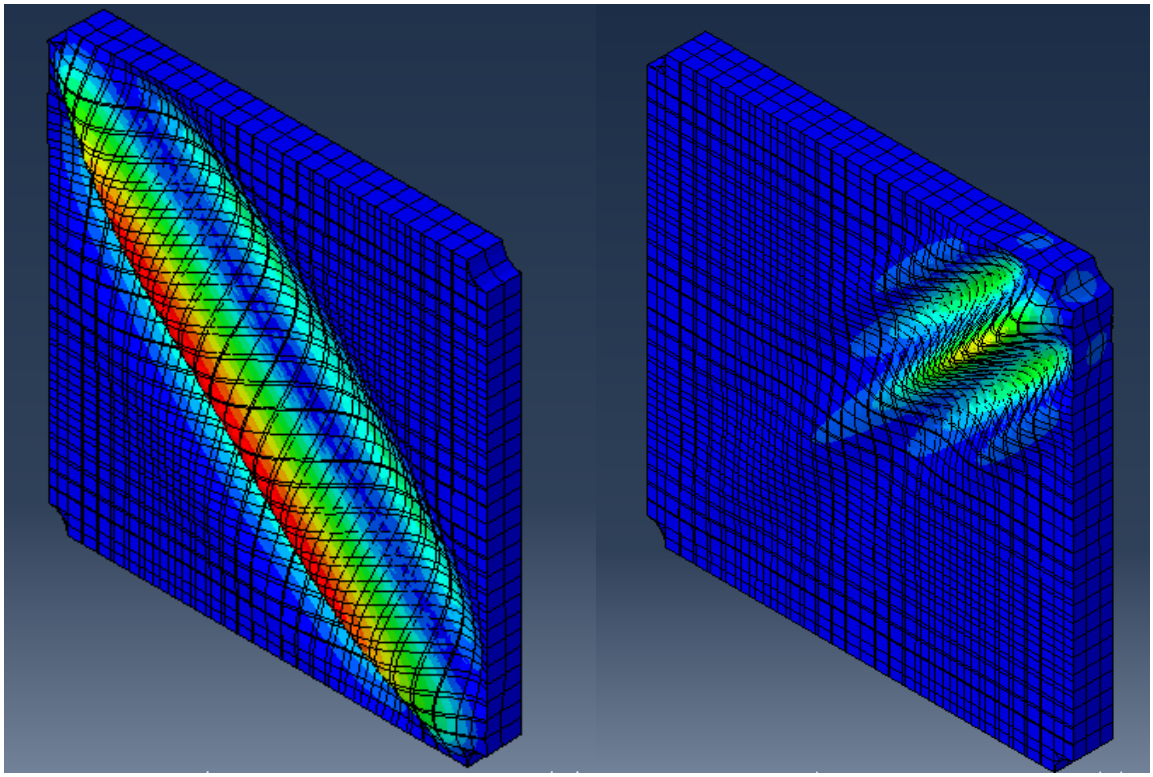

Figure 17: Examples of Shear Buckling Mode (Left: Global, Right: Local/Wrinkling)

To further investigate the results given in Table 6, two additional studies were performed in which core and face sheet thickness were again varied, but with a larger range and finer granularity of samples. With the exception of these variables, the models were left unchanged from before. Figure 18 presents the variation in critical buckling shear stress with core thickness between 0.5 in. and 1.7 in., keeping a constant 2-lamina face sheet. As can be seen, critical shear buckling stress increases with core thickness following a roughly bilinear function with a transition region between. Variation in critical buckling load and critical buckling load-per-unit-thickness follow the same trend. Interestingly, this transition region (occurring for a core thickness between 1.0 in. and 1.2 in.) corresponds to a transition between global and local buckling modes and includes some mixed modes as well. This suggests that, keeping the face sheet constant, there is a point at which a sandwich's shear buckling mode will become a local, wrinkling mode, after which an increase in core thickness does not lead to significant additional buckling resistance.

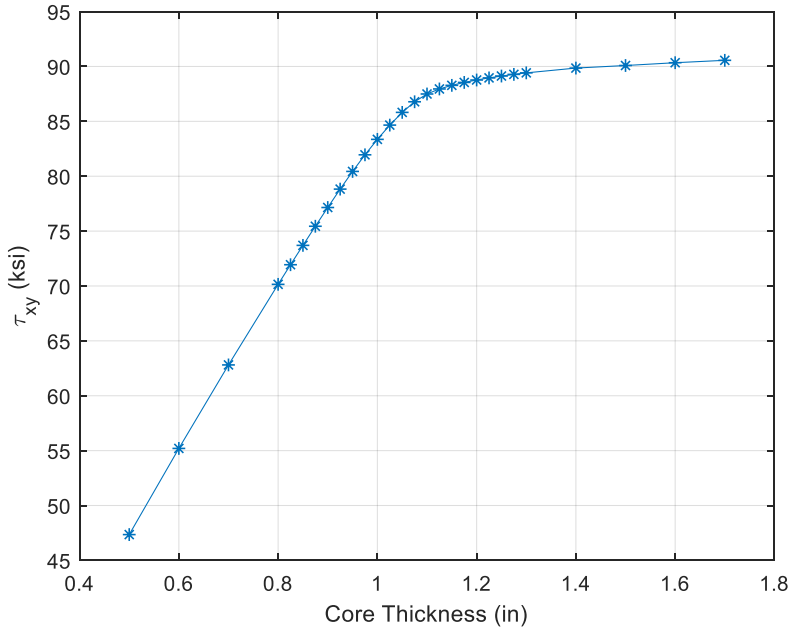

Figure 18: Variation of Critical Shear Stress with Core Thickness

The second shear buckling study was performed as the inverse of the first, with a constant 0.75 in. core and increasing numbers of face sheet laminae. The variation in critical buckling shear stress with increasing face sheet laminae (increasing face sheet thickness) is shown in Figure 19. This shows that for a constant core thickness, there exists a number of face sheets (in this case 5) for which critical shear stress is minimized. However, as seen in Figure 20, this trend is not carried through with critical shear stress resultant and critical load. As can be seen here, shear stress resultant increases with number of face sheet laminae and is minimized for zero, as expected. It is interesting to note from Figure 20 that the shear stress resultant curve appears to be a smooth function, except for the sandwich with a single layer laminate. This is also the only model analyzed in this study which resulted in a wrinkling mode rather than a global buckling mode. This suggests that for a constant core thickness, there is a minimum number of face sheet laminae to ensure a global shear buckling mode.

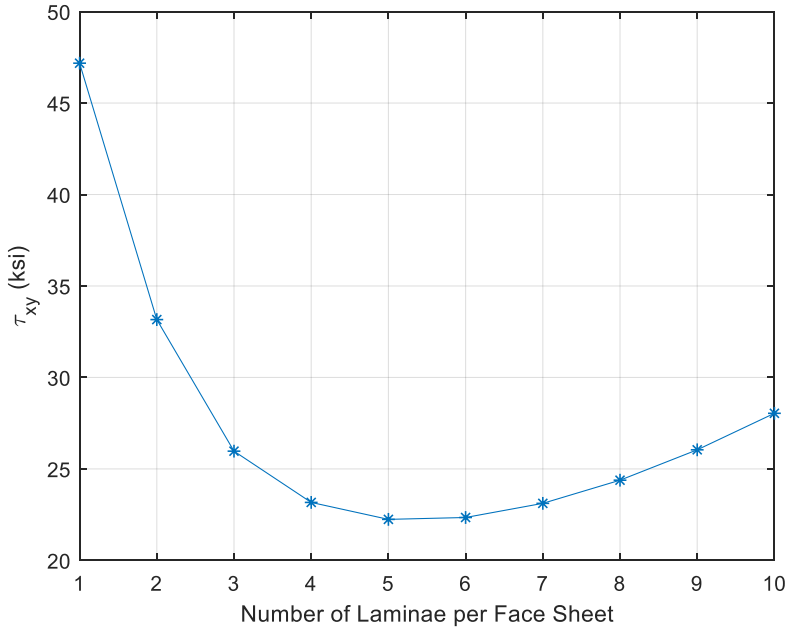

Figure 19: Variation in Critical Shear Stress with Face Sheet Thickness

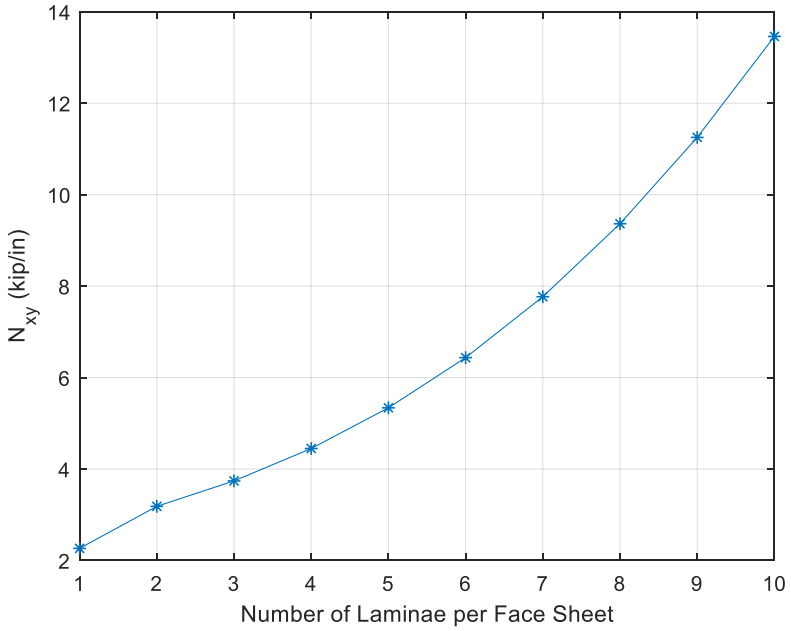

Figure 20: Variation in Critical Shear Stress Resultant with Face Sheet Thickness

As a final investigation of shear buckling, the FE models simulated initial geometric imperfections and the reduction in critical shear buckling loads were examined. As the presence and form of geometric imperfections in actual members and structures is inherently variable, it is prohibitively impractical to investigate every possible form that these imperfections may take. To

introduce a reasonable worst-case, models were created which incorporated single and double initial curvature with amplitude equal to the maximum allowable out-of-flatness for pultruded FRP plates taken equal to 0.096 in. (ASTM, 2015). A model of each test specimen type was created with both single and double curvature imperfections (as seen in Figure 21) and analyzed with loads, boundary conditions, and mesh similar to previous analyses. Table 7 presents the critical shear buckling loads, stress resultants, and stresses from these analyses as well as the modality.

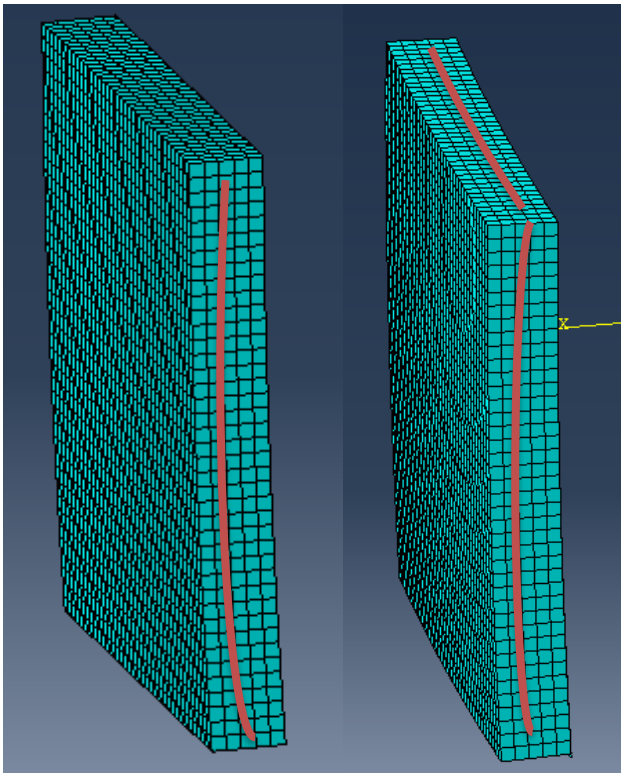

Figure 21: Simulated Geometric Imperfections (Left: Single Curvature, Right: Double Curvature)

Table 7: Buckling Analysis Results with Included Imperfections

Model	$N_{xy,cr}$ (kip/in)		P_{cr} (kip)		τ_{cr} (ksi)		Mode Type	
Curvature	Single	Double	Single	Double	Single	Double	Single	Double
F2C75	2.85	2.60	48.5	44.1	29.7	27.1	G	G
F2C150	4.04	3.36	68.5	57.1	42.0	35.0	M	L
F4C75	3.90	3.75	66.2	63.6	20.3	19.5	G	G
F4C150	6.32	5.96	107.3	101.2	32.9	31.1	G	G

*G = Global Mode, M = Mixed Mode, L = Local Mode

As can be seen by comparing the results shown in Table 7 with those in Table 6 (and between one another in 7), the inclusion of additional imperfections tended to reduce the critical shear buckling load by a decreasing amount. This is consistent with expected behavior in which initial geometric imperfections tend to significantly decrease a structure's critical buckling load.

Interestingly, the mode shapes of imperfect models and general modality were similar to the perfect models as seen in Figure 22. The only non-globally buckled model was again the model of F2C150, which displayed a mixed and local buckling mode for the single and double curvature imperfect models, respectively.

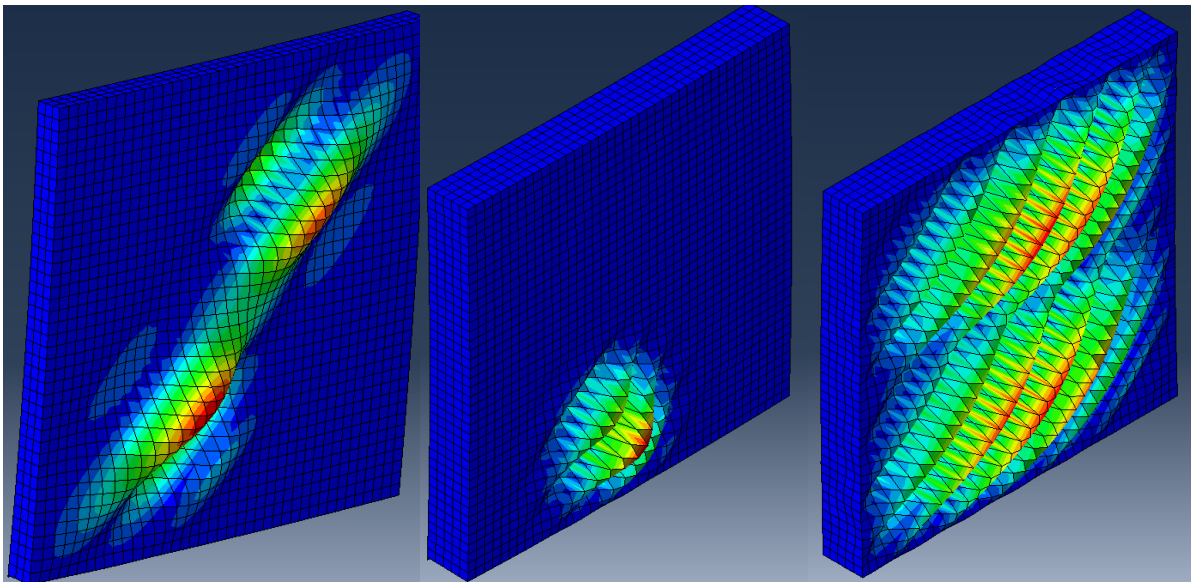

Figure 22: Buckling Models of Models with Imperfections (Left: Global, Center: Local, Right: Mixed)

Two additional types of imperfection common in composites manufactured by wet layup and resin infusion were investigated to assess their effects on sandwich panel buckling. These were a local loss of adhesion between the face sheets and core (a delamination) and a localized lack of full fiber wet-out (a "dry-spot"). These were investigated separately to isolate their effects but are likely to occur simultaneously within an actual sandwich. To incorporate a delamination, the kinematic constraints coupling the degrees of freedom of the face sheet and core in the local defect area were relaxed, allowing face sheet and core to displace independently. Similarly, to incorporate a dry spot, the elastic properties of the face sheet in the defect area were taken as effectively nil. As a preliminary investigation, and as no specific defect data were available on which to base analyses, defects were taken as square patches at the center of face sheets, with side-lengths of increasing 1 in. increments. Analyses were conducted for each specimen size and assuming a defect on one face sheet and on both face sheets.

Figures 23 and 24 present the effect of delamination on critical shear buckling stress resultant for each sandwich type assuming a defect on one and both face sheets. As can be seen, delaminations tended to decrease critical shear buckling resultant in every case, with the largest decreases occurring for delaminations between 1 and 3 in. As delamination sizes continued to increase, critical shear buckling stress resultants tended toward constant values, the shear stress resultants of the face sheets themselves devoid of support from the core. Interestingly, very little difference exists between the predicted buckling of the models with one face sheet delamination

and two delaminations. This may result from the fact that these buckling modes tended to be localized, with little interaction between the face sheets.

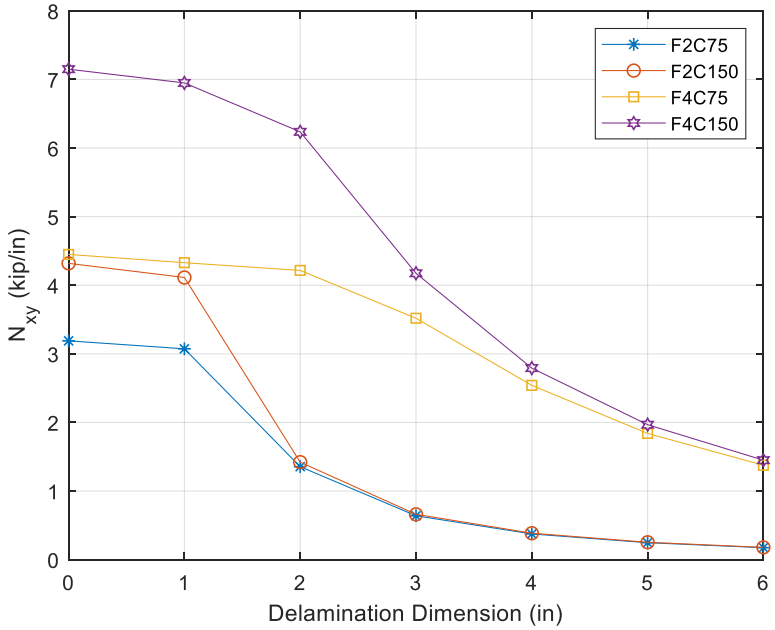

Figure 23: Effect of One-Side Delamination on Critical Shear Buckling Stress Resultant

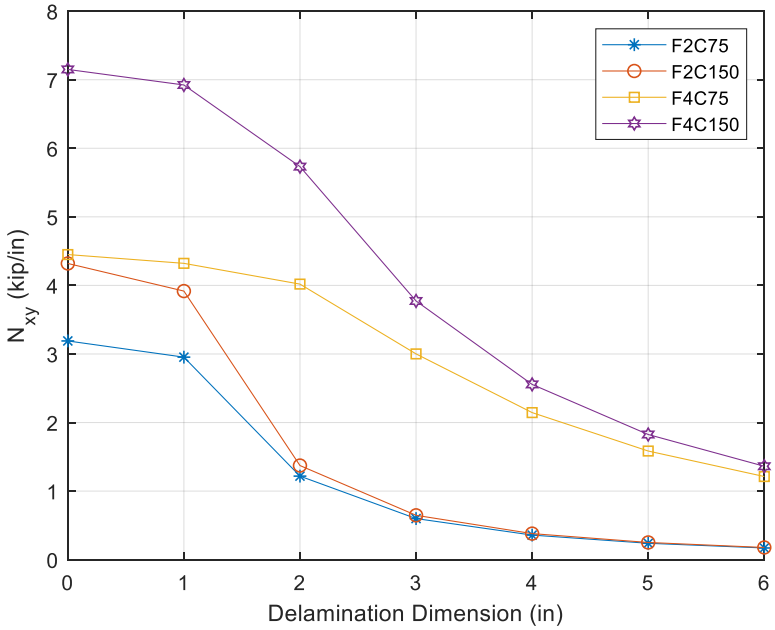

Figure 24: Effect of One-Side Delamination on Critical Shear Buckling Stress Resultant

Figures 25 and 26 present the effects of face sheet dry spots on critical shear buckling stress resultant. As expected, localized lack of stiffness led to decreases in buckling stress, with larger defect zones leading to larger decreases in buckling. However, the effect tended to be less severe than the effect of delaminations as seen in Figures 23 and 24. Additionally, and in contrast to delamination, a dry spot occurring on both face sheets tended to have a much more severely detrimental effect on critical buckling stress resultant than on a single face sheet. It is possible that this results from the fact that the constraint between face sheets and core remains intact, allowing more complex interaction between the face sheets than in the case of delamination.

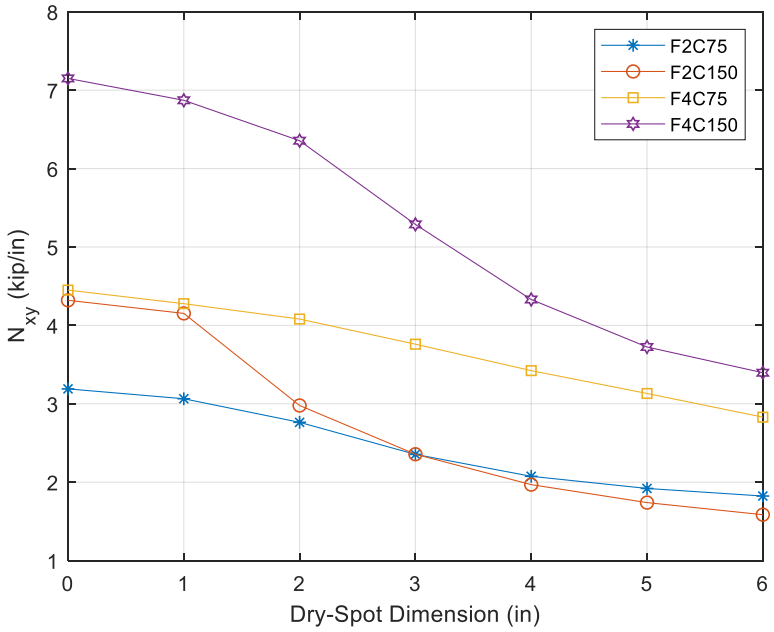

Figure 25: Effect of One-Side Delamination on Critical Shear Buckling Stress Resultant

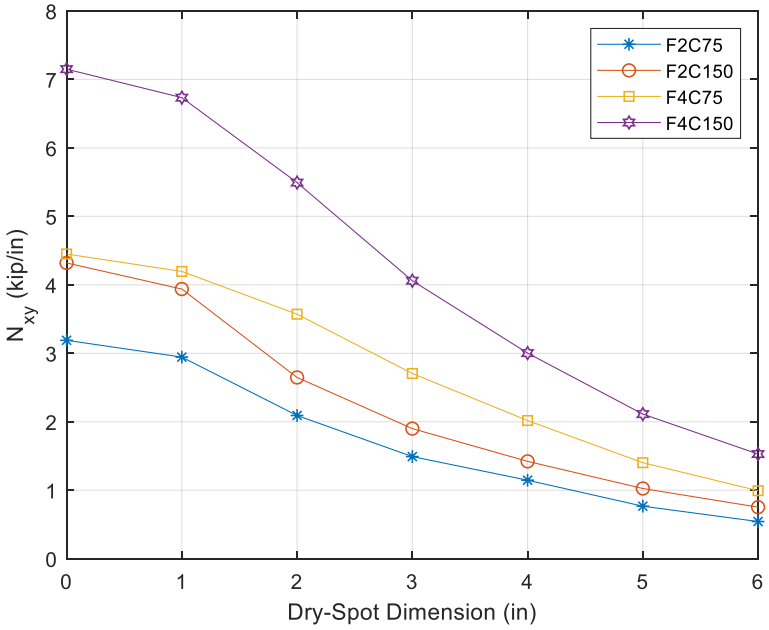

Figure 26: Effect of One-Side Delamination on Critical Shear Buckling Stress Resultant

2.4 Finite Element Simulation of Full CT-Girder Bridge Shear Response

The experiments and analyses described to this point were performed to better characterize the strength of CT girder webs in shear thus improving the accuracy of the predicted shear resistance used in their design. The efficiency of designs can be further improved by accurately predicting to shear demand on CT girder webs, especially live-load shear demand. Currently, the shear demand placed on CT girder bridges is determined based on general AASHTO design provisions (2017), which use empirical distribution factors (DFs) to distribute live-load shear to individual girders. Use of these DFs leads to inherently conservative predictions for the superstructure types for which they were designed, with the conservatism of predictions for CT girder superstructures in question. More accurate predictions of live-load distribution can be achieved through analysis of 3D FE models of full bridges, regardless of superstructure type. To assess the predictions of shear demand placed on CT girder bridges using AASHTO DFs, a detailed FE model of the HGMB the first CT girder bridge designed and constructed, was analyzed under design shear loads, with the resulting web shear stresses compared to predictions using conventional beam-line analysis and AASHTO DFs.

2.4.1 Model and Analysis Details

Modeling and analysis of the HGMB FE model were again performed with *ABAQUS* (2019). Development was described extensively in a previous report (Schanck & Davids, 2021)

and so will not be further described here, with the exception of details specific to these analyses. Figure 27 presents an image of the final, meshed model with specific bridge components noted.

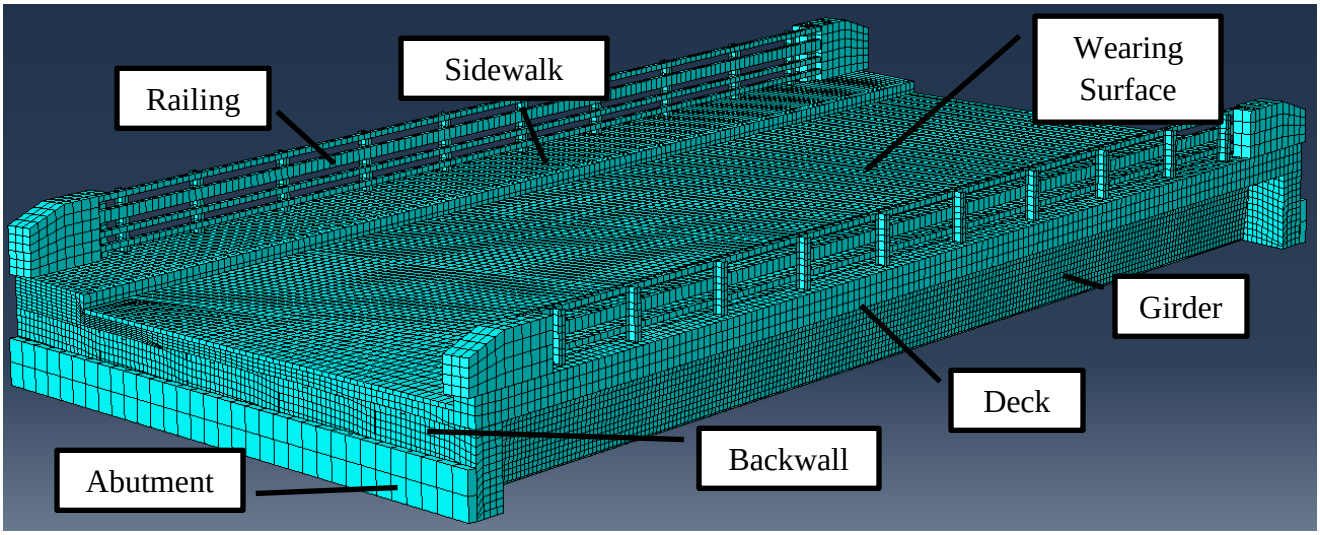

Figure 27: Meshed HGMB FE Model

The model was loaded to mimic AASHTO HL-93 shear loading (2017). This included a uniform lane load and HL-93 truck in each lane. Each of these loads was applied as a uniform patch pressure load, to produce maximum shear load in the center girder. To capture the highest estimated live-load shear stresses, ten load cases were investigated with the trucks' back wheels positioned between 0.5 girder depths and 5.0 girder depths from the backwall in 0.5 depth increments. The loads applied to the model's wearing surface and producing the largest shear stresses (at one girder depth from the backwall, determined as explained below) can be seen in Figure 28. Load factors were not applied to the loads as the geometric and material linearity of the analysis (as explained below) allowed loads to be factored and superimposed afterward. However, an impact factor of 33% was added to the truck loads.

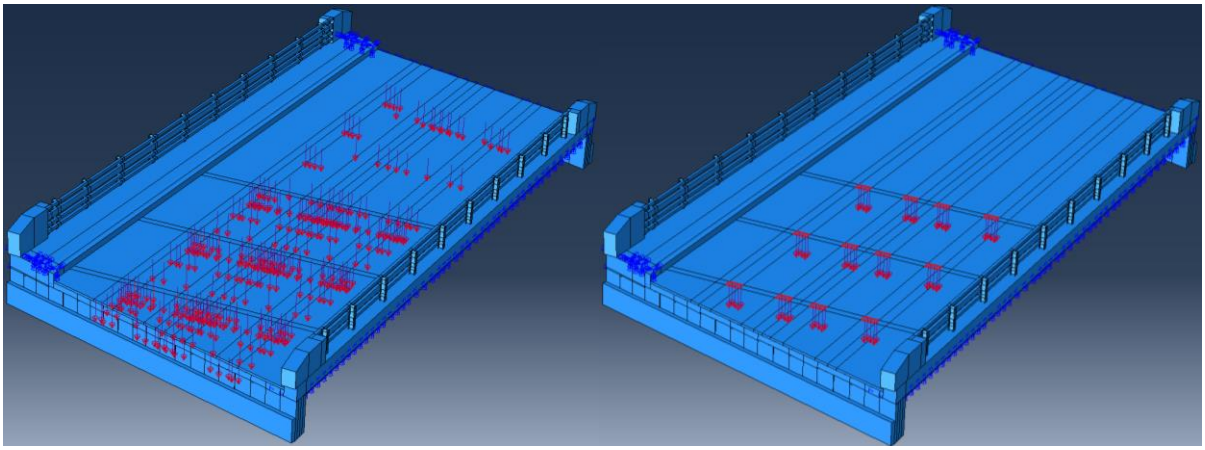

Figure 28: Application of HL-93 Shear Load (Left: Lane, Right: Truck)

In its initial implementation (Schanck & Davids, 2021) the HGMB FE model employed a two-step solution process wherein dead and live-load effects were determined sequentially. This allowed geometric nonlinearity to be incorporated as the solution did not rely on superposition. However, this did not allow the effects of staged construction to be taken into account. For this analysis, it was important that the shear stresses locked into the CT girder before deck curing were considered. Therefore, the FE model was used for live-load effects only and geometric nonlinearity was not considered. Dead-load shear stresses, both before and after the concrete deck had cured were determined by elementary mechanics, assuming girders to be loaded by material within a tributary area. This also allowed service-level and strength-level loading to be considered with a single set of analyses by multiplying results by appropriate load factors.

2.4.2 Results

To determine the controlling live-load shear stresses predicted under each of the investigated load cases, stresses through the girder were recovered at ten positions along the span, again between 0.5 girder depths and 5.0 girder depths from the backwall in 0.5 depth increments. However, due to the girder's fiber orientation, the shear stress in local coordinates was determined through plane-stress stress transformation, as described by Equation 2.4.2-1.

$$\begin{Bmatrix}\sigma_{11}\\ \sigma_{22}\\ \tau_{12}\end{Bmatrix} = [T]^{-1}\begin{Bmatrix}\sigma_{xx}\\ \sigma_{yy}\\ \tau_{xy}\end{Bmatrix} \tag{2.4.2-1}$$

Here, σ_{ii} is a normal stress, τ_{ij} is a shear stress, T is a transformation matrix based on the web's outermost fiber orientation, and the subscripts x and y and 1 and 2 denote the global and local coordinate systems, respectively. τ_{xy} represents the live-load shear stress in global coordinates, the quantity of interest. Applying Eq. 2 to the stresses recovered at each of the ten sections for each of the ten load cases, it was found that the maximum shear stresses in the webs were predicted to occur at 0.5 girder depths from the backwall under the load-case with trucks positioned 1 girder depth from the backwall. Dead-load shear stresses were determined though the girder at the heights corresponding to web nodal locations using Equation 2.4.2-2:

$$\tau(y) = \frac{VQ(y)}{It(y)} \tag{2.4.2-2}$$

where $\tau(y)$ is the shear stress at a height y from the bottom of the section, V is the shear load at one girder depth from the backwall due to structural (DC) or nonstructural (DW) dead load, $Q(y)$ is the first moment of area about the composite neutral axis at a height y (before or after concrete cure as required), I is the moment of inertia of the section (again, before or after concrete cure as required), and $t(y)$ is the width of the section at a height y from the section's base. For service-level loading, these shear stresses were taken as is and summed for the total service shear stress, and for strength-level loading, were multiplied by appropriate load-factors and then summed. Dead, live, and combined shear stresses through the height of the web determined through the

combination of strength-of-materials and FE analysis are presented in Figures 29, 30, and 31, respectively.

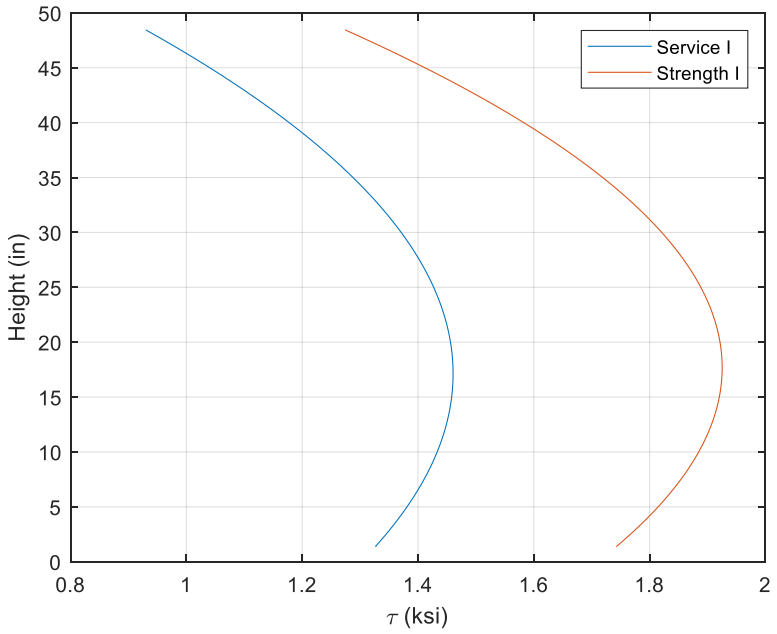

Figure 29: Dead-Load Shear Stress Distribution

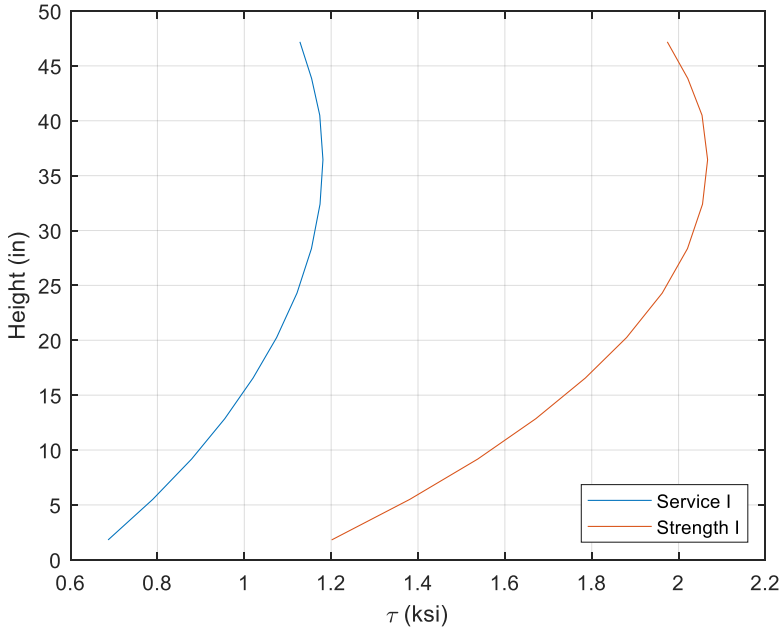

Figure 30: Live-Load Shear Stress Distribution

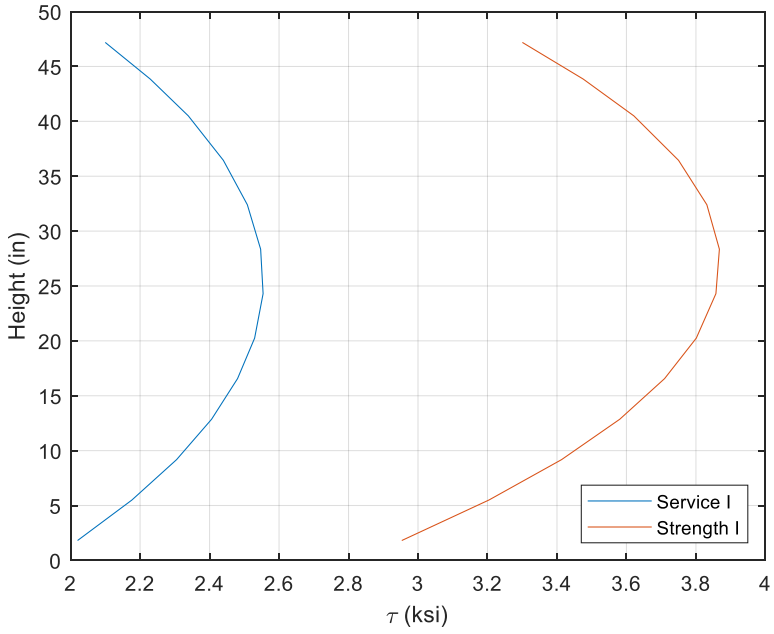

Figure 31: Total Load Shear Stress Distribution

2.4.3 Comparison with Conventional Analysis

The results of FE analysis of HL-93 shear stresses on the HGMB can be directly compared with those found using conventional analysis by AASHTO (2017) to assess their relative conservatism. Dead-load shear stresses were taken equal to those found in the previous analysis, and live-load shear stresses were found again using Eq. 3, with V taken as the live-load shear force produced by HL-93 loading at one girder depth from the backwall multiplied by the appropriate DF. This DF, was taken as 1.10 as calculated in the bridge's original design (AIT, 2019) and based on Table 4.6.2.2.3c of AASHTO LRFD (2017) with an included skew correction factor. Combined shear stresses for service and strength-level loading were taken as the sum of dead and live-load stresses, and the sum of dead and live-load stresses multiplied by appropriate load factors, respectively. These live-load and combined stresses are plotted through the depth of the girder, along with the stresses determined before using FE analyses in Figures 32 and 33, respectively. Table 8 presents the maximum live-load and total shear stresses under service and strength conditions predicted by both methods. It is immediately clear from the results presented that conventional analysis leads to highly conservative predictions in comparison with FE analysis. Using the more accurate prediction of live-load shear distribution and shear stress distribution available from 3D FE analysis leads to reductions in predicted maximum live-load shear stress of 74% and maximum total shear stress of 57% respectively relative to predictions using AASHTO DFs (2017) and strength-of-materials shear stress distribution.

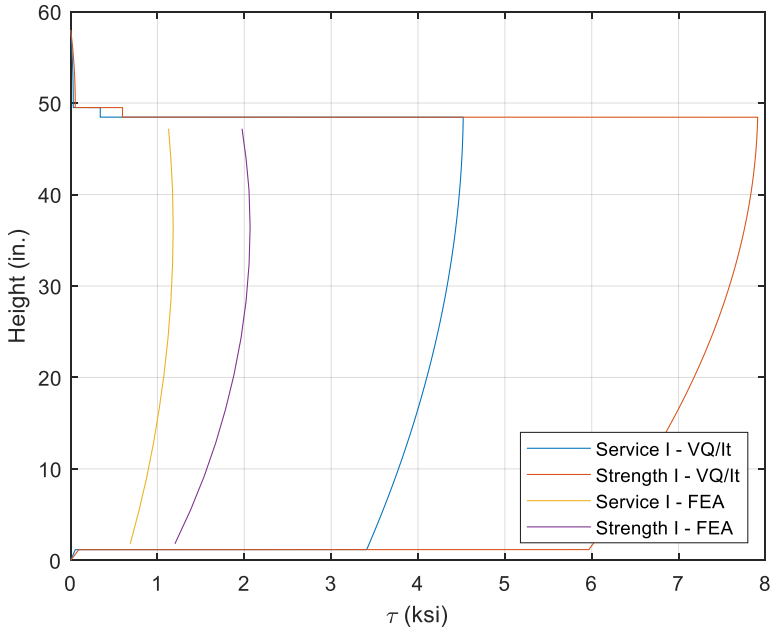

Figure 32: Comparison of Live-Load Shear Stress Distribution

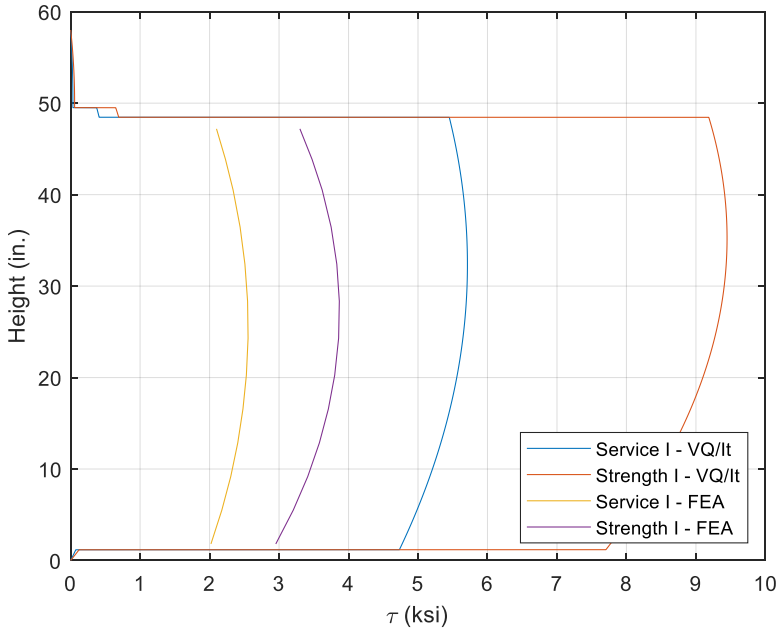

Figure 33: Comparison of Total Load Shear Stress Distribution

Table 8: Comparison of Predicted Maximum Shear Stress

Analysis Method	Load Level	Shear Stress (ksi)	
		Live – Load	Total Load
$\frac{VQ}{It}$	Service I	4.52	5.71
	Strength I	7.91	9.45
FE	Service I	1.18	2.55
	Strength I	2.07	3.86

Because the FE analyses were able to take the full, three-dimensional behavior of the bridge into account, a more accurate prediction of live-load shear distribution was incorporated into shear stress predictions than is provided by AASHTO shear load DFs (2017). This, along with the simplifying assumptions made when using Eq. 3 to predict shear stress in conventional analysis, combine to produce the significant differences in predicted maximum shear stress presented in Table 8.

To explore this further, girder end reactions predicted by the model were used to compute bridge-specific live-load distribution factors for comparison with the AASHTO-specified distribution factors used for design of the HGMB. Doing this for each of the analyses (i.e. with the trucks positioned at each of the ten points along the span), the most severe interior girder shear DF was found to equal 0.490, 55% smaller than the value used for the design of the HGMB (AIT,2019) as specified by AASHTO (2017). This suggests that conservative shear load distribution contributes around 75% of the difference between conventional and FE analysis of the HGMB under shear loading with the remainder likely contributed by the simplifying assumptions inherent in the use of Eq. 3 and transformed section analysis.

2.5 Conclusions, Implications, and Future Work

This study examined and addressed CT girder web shear strength in three phases, namely experimental investigation, numerical simulation of the results of experimental testing, and expanded numerical analysis into stability and full-scale structures. Owing to a number of unforeseen complications and oversights, the primary goal of characterizing CT web shear strength was not fully realized. Despite this however, the results of this investigation lead to a variety of conclusions which hold important implications for future development and implementation of CT girder bridges.

Due to the limitations of the ASTM D8067/D8097M-17 (2017) picture frame testing fixture used for experimental testing, as well as their susceptibility to bearing failure, none of the picture frame shear specimens were able to be loaded to their full shear rupture or shear buckling capacity. It is therefore not appropriate or possible for conclusions to be drawn from this study regarding the actual, full strength of CT girder webs. However, importantly, the results of this testing are

internally consistent. With the exception of the first specimen tested (F2C75-01), each of the thinner specimens were tested to a shear greater than 18 ksi without exhibiting signs of significant shear damage. This value of 18 ksi can therefore serve as a reasonable lower bound to the web shear strength. Additionally, all of the thicker specimens were able to withstand the maximum allowable load on the test fixture, at which point they were under a state of shear stress greater than the shear strength assumed during design of the HGMB (AIT, 2019) without sign of distress. It can therefore be concluded that, from a material strength standpoint, the shear design of the HGMB is conservative as its maximum shear stress limit (before application of statistical and environmental reduction factors) was exceeded by every specimen. One caveat is that the HGMB girder webs are much deeper than the dimensions of the test specimen, and web buckling must also be considered in design.

Again from the inability to reach a state of shear failure during experimental tests, limited conclusions can be drawn from the results of stress FE simulation of the picture frame shear tests. However, by comparing the specimens' strain fields calculated from measured DIC data with the calculated strain fields from FE analysis, it can be concluded that the picture frame test itself produces a near-pure state of shear and so the results of future testing can be considered high-quality. The FE models were designed to be inherently flawless, under a state of pure shear, and used nominal material properties for constitutive behavior. Despite these simplifications, their predictions matched testing results reasonably well. This then implies that the picture frame test itself produces reliable and useful data despite the presence of these complicating factors.

FE buckling simulations of the picture frame specimens revealed various components of CT girder web shear buckling behavior that may have broad implications for design. First, and perhaps most applicably in the near-term, comparison of results of testing and shear buckling simulation suggest that shear buckling is a moderate concern but can be addressed through conservative design. Of the analyses used, the minimum critical shear buckling stress was around 22 ksi, 22% greater than the 18 ksi lower-bound shear strength suggested above. However, the analyses were performed for models with perfect geometry, boundary conditions, and loading, and so the behavior of actual structures may be different. Additionally, as mentioned above, comparison of predicted and measured out-of-plane displacement indicates an imperfect characterization of the core, which also affects results. A conservative design basis with adequate safety and reliability factors can address his uncertainty, significantly reducing its effect. Second, the analyses performed show that both the core and face sheets of a sandwich play important roles in web shear buckling behavior. The thickness of the face sheet appears to have greater control over the critical shear buckling stress, whereas the thickness of the core seems to control the mode (global or local buckling). Therefore, in the design of CT girder webs, the effects of both the face sheets and core must be considered. Finally, as with any elastic buckling analysis, careful consideration should be given to geometric imperfections and defects as was demonstrated by analyzing models with imperfect curvature, delamination, and dry spots. These and other deviations have been shown to affect buckling behavior, reducing critical loads significantly.

Analysis of the HGMB under shear loading suggests that the analytical design of the structure is conservative, especially concerning shear load distribution and maximum predicted shear stress. It is evident from the analyses performed here that, at least for the HGMB, the shear distribution factors used in design (AIT, 2019) are inaccurate for CT girder bridges, leading to conservative design loads. However, once those loads are distributed to individual girders, the stress distribution predicted by elementary strength-of-materials (Eq. 2.4.2-2) is reasonably accurate, as evidenced by the similar shapes of curves seen in Figures 32 and 33 and the much smaller role the simplifying assumptions of Eq. 3 played in the difference between maximum predicted shear stresses. It can therefore be concluded that, with the introduction of more accurate shear distribution factors, the current beamline and strength-of-materials approach to design will yield reasonably accurate design shear stresses.

Based on the results of this investigation, future research on the following topics would be valuable:

- Additional picture frame specimens should be manufactured and tested to failure in shear. These specimens should have doublers adhered to both sides of both face sheets to preclude bearing failure or otherwise strengthened edges, and a new picture frame test fixture with a higher maximum capacity and looser fitment tolerances should be designed and manufactured for this testing.

- FE simulations should be conducted of the aforementioned additional tests for comparison and to gain additional behavioral insight

- Details of typical specimen defects should be cataloged, and these specific defects modeled to determine their effects on critical shear buckling stresses.

- Girder-scale tests should be conducted to assess the shear capacity of a full girder web.

- A full CT-girder bridge should be tested under high shear load to calibrate additional full-bridge FE models for the purposes of developing empirical shear distribution factors.

- Results of the above-mentioned tests and analyses should be implemented within subsequent editions of a CT girder design guide specification.

3 CT Girder Design Specification

3.1 Introduction

The purpose of this section is to provide basic guidance on the structural analysis and design of composite tub (CT) girders consisting of open-section hybrid fiber reinforced composite (FRP) girders that are composite with reinforced concrete decks for bridge applications. This section is modeled after design guides from the American Association of State Transportation Officials (AASHTO), which are referenced throughout for both load and resistance guidance. The design guidance and procedures contained within this section include:

- Determination of elastic properties of FRP composite components
- Appropriate limit states and corresponding load and resistance factors
- Determination of girder moment capacity
- Determination of girder shear capacity
- Shear connector design
- Limitation of deflections

It should be noted that since the CT girder system is still in active development (see for instance Davids et al. 2022a, Davids et al. 2022b, Davids & Schanck 2022, Guzzi 2019, Schanck 2021), the provisions in this document should be considered preliminary and subject to change based on additional research and development. Additionally, while some design topics have been well characterized, leading to in-depth design procedures, others are less certain and so the guidance provided requires greater levels of scrutiny and judgement by the engineer of record.

3.2 FRP-Concrete Composite Tub Girders

3.2.1 Scope

This section contains provisions for the design of simply supported CT girders for use as the main structural components of a bridge. The provisions apply for CT girders that are made composite with normal-weight cast-in-place or precast concrete decks having compressive strengths f'_c between 2.5 ksi and 10.0 ksi.

3.2.2 Definitions and Notation

$A_{bf} =$ cross-sectional area of the bottom flange (in.^{2})

$A_{sc} =$ cross-sectional area of a single stud connector in bearing connection (in.^{2})

$A_{vf} =$ area of clamping studs in a friction connection (in.^{2})

$b_c =$ effective width of the deck over the CT girder (in.)

$b_i =$ width of a discretized layer of a composite section (in.)

$b_t =$ width of individual top flange (in.)

$C =$ compressive force resultant from concrete (kip)

$C_E =$ environmental reduction factor

$c =$ composite section neutral axis depth (in.)

$c_{cf} =$ cohesion factor between concrete and FRP

$D =$ height of composite section (in.)

$d =$ height of non-composite section (in.)

$d_s =$ shear stud diameter (in.^{2})

$dA =$ differential area over which an infinitesimal stress, σ_i acts (in.^{2})

$E_c =$ elastic modulus of concrete (ksi)

$E_{bf} =$ longitudinal elastic modulus of bottom flange laminate (ksi)

$E_{tf} =$ longitudinal elastic modulus of top flange laminate (ksi)

$E_w =$ longitudinal elastic modulus of web laminate (ksi)

$E_1 =$ elastic modulus of FRP lamina in longitudinal direction (ksi)

$E_2 =$ elastic modulus of FRP lamina in transverse direction (ksi)

$f'_c =$ 28-day specified compressive strength of concrete (ksi)

$f_{ct} =$ stress at the top of the deck (ksi)

$f_{cb} =$ stress at the bottom of the deck (ksi)

$f_{tb} =$ FRP top flange bearing strength (ksi)

$f_u =$ minimum specified tensile strength of a stud connector (ksi)

$f_{vr} =$ shear strength of the resin making up the connection ridges (ksi)

$f_y =$ yield strength of clamping studs (ksi)

f_{1c} = design compressive strength of FRP lamina in longitudinal direction considering reductions for service environment (ksi)

f_{1c}^{*} = compressive strength of FRP lamina in longitudinal direction for product certification as reported by manufacturers (ksi)

f_{1t} = design tensile strength of FRP lamina in longitudinal direction considering reductions for service environment (ksi)

f_{1t}^{*} = tensile strength of FRP lamina in longitudinal direction for product certification as reported by manufacturers (ksi)

f_{1tbf} = tensile strength of FRP lamina making up CT girder bottom flange in longitudinal direction for product certification as reported by manufacturers (ksi)

f_{1tw} = tensile strength of FRP lamina making up CT girder web in longitudinal direction for product certification as reported by manufacturers (ksi)

f_{2c} = design compressive strength of FRP lamina in transverse direction considering reductions for service environment (ksi)

f_{2c}^{*} = compressive strength of FRP lamina in transverse direction for product certification as reported by manufacturers (ksi)

f_{2t} = design tensile strength of FRP lamina in transverse direction considering reductions for service environment (ksi)

f_{2t}^{*} = tensile strength of FRP lamina in transverse direction for product certification as reported by manufacturers (ksi)

f_{6} = design in-plane shear strength of FRP lamina considering reductions for service environment (ksi)

f_{6}^{*} = in-plane shear strength of FRP lamina for product certification as reported by manufacturers (ksi)

f_{6w} = design ultimate shear stress of the webs (ksi)

G_{6} = in-plane shear modulus of FRP lamina (ksi)

h_{web} = web height (in)

I_{C} = moment of inertia (second moment of area) of the composite CT girder (in.^{4})

I_{NC} = moment of inertia (second moment of area) of the non-composite FRP section (in.^{4})

$K_1 =$ fraction of concrete strength available to resist interface shear

$K_2 =$ limiting shear stress (ksi)

$L_{vi} =$ spacing of intermediate clamping studs (in.)

$M_n =$ nominal flexural resistance (kip-in.)

$M_1 =$ nominal flexural resistance of a composite section based on concrete crushing (kip-in.)

$M_2 =$ nominal flexural resistance of a composite section based on bottom flange rupture (kip-in.)

$M_n^c =$ nominal flexural resistance of the composite section (kip-in.)

$M_r =$ design flexural resistance (kip-in.)

$M_u =$ ultimate flexural load (kip-in.)

$M^+ =$ nominal flexural resistance of portion of non-composite CT girder under tensile stress (kip-in.)

$M^- =$ nominal flexural resistance of portion of non-composite CT girder under compressive stress (kip-in.)

N_{xycr} critical shear buckling shear stress resultant (kip/in.)

$n =$ total number of shear studs spaced at s, number of layers into which a composite section is discretized

$n_{bf} =$ modular ratio of bottom flange

$n_{tf} =$ modular ratio of top flange

$P_c =$ permanent net compressive force normal to shear plane (kip)

$Q_n =$ nominal horizontal shear resistance (kip)

$Q_r =$ design horizontal shear resistance (kip)

$Q_{int} =$ first moment of area of the composite CT girder section about its neutral axis evaluated at the top of the web (in^3)

$Q_1 =$ nominal horizontal shear resistance – concrete crushing (kip)

$Q_2 =$ nominal horizontal shear resistance – stud tensile failure (kip)

$Q_3 =$ nominal horizontal shear resistance – FRP bearing failure (kip)

$R =$ residual (unbalanced) force in composite section (kip)

$s =$ shear stud spacing (in.)

$s_r =$ shear ridge spacing (in.)

$T =$ tensile resultant from bottom flange (kip)

$t_{bf} =$ thickness of bottom flange laminate (in.)

$t_c =$ thickness of the deck above the CT girder (in.)

$t_{core} =$ thickness of web's core material (in.)

$t_{tf} =$ thickness of top flange laminate (in.)

$t_{web} =$ thickness of web (in.)

$t_{w-fs} =$ thickness of the web, less the thickness of any sandwich core material (in.)

$V_n =$ nominal shear resistance (kip)

$V_r =$ design shear resistance (kip)

$V_u =$ ultimate shear load, (kip)

$v_n =$ nominal shear flow resistance (kip/in.)

$v_r =$ design shear flow resistance (kip/in.)

$w_r =$ width of shear ridges (in.)

$y_i =$ height of a discretized layer of composite section above the base (in.)

$\bar{y}_{NC} =$ neutral axis height of non-composite section (in.)

$Z_r =$ fatigue resistance of a single shear stud (kip)

$\beta_1 =$ Whitney's stress block ratio (5.7.2.2)

$\gamma_6 =$ design ultimate in-plane shear strain of FRP lamina considering reductions for service environment (in./in.)

$\gamma_6^* =$ ultimate in-plane shear strain of FRP lamina for product certification as reported by manufacturers (in./in.)

$\delta y =$ thickness of a discretized layer of composite section (in.)

$\varepsilon_c =$ maximum strain in concrete prior to the onset of significant softening (in./in.)

$\varepsilon_{ct} =$ strain at the top of the deck (in./in.)

$\varepsilon_{cb} =$ strain at the bottom of the deck (in./in.)

$\varepsilon_f =$ ultimate strain (in./in.)

$\varepsilon_i =$ strain in a discretized layer of composite section (in./in.)

$\varepsilon_{cu} =$ concrete crushing strain (in./in.)

$\varepsilon_0 =$ concrete compressive strain at peak compressive stress (in./in.)

$\varepsilon_{1c} =$ design ultimate compressive strain of FRP lamina in longitudinal direction considering reductions for service environment (in./in.)

$\varepsilon_{1c}^* =$ ultimate compressive strain of FRP lamina in longitudinal direction for product certification as reported by manufacturers (in./in.)

$\varepsilon_{1ctf} =$ ultimate compressive strain of top flange FRP laminate in longitudinal direction (in./in.)

$\varepsilon_{DC} =$ tensile strain due to factored, non-composite dead-loads (in./in.)

$\varepsilon_{1t} =$ design ultimate tensile strain of FRP lamina in longitudinal direction considering reductions for service environment (in./in.)

$\varepsilon_{1t}^C =$ tensile strain in the bottom flange corresponding to failure due to moment acting on the composite section (in./in.)

$\varepsilon_{1t}^* =$ ultimate tensile strain of FRP lamina in longitudinal direction for product certification as reported by manufacturers (in./in.)

$\varepsilon_{1tbf} =$ ultimate tensile strain of bottom flange FRP laminate in longitudinal direction (in./in.)

$\varepsilon_{2c} =$ design ultimate compressive strain of FRP lamina in transverse direction considering reductions for service environment (in./in.)

$\varepsilon_{2c}^* =$ ultimate compressive strain of FRP lamina in transverse direction for product certification as reported by manufacturers (in./in.)

$\varepsilon_{2t} =$ design ultimate tensile strain of FRP lamina in transverse direction considering reductions for service environment (in./in.)

$\varepsilon_{2t}^{*} =$ ultimate tensile strain of FRP lamina in transverse direction for product certification as reported by manufacturers (in./in.)

$\kappa =$ composite section curvature at failure (in.$^{-1}$)

$\mu =$ friction factor between FRP ridges and concrete

$\sigma_i =$ stress in a discretized layer of composite section (ksi)

$\phi =$ resistance factor

$\phi_i =$ resistance factor associated with flexural failure of an individual component of a composite section or assumed failure mode

3.2.3 Limitations

Seismic design is not addressed in this document. However, where applicable, it shall be considered as one of the loading cases. CT girders shall not be used as ductile earthquake resisting elements. These provisions are intended for the design of simply supported CT girders comprised of glass, carbon, aramid or other fiber reinforcements in a polymer matrix with sufficient durability and resistance to environmental stressors.

3.2.4 Material Properties

3.2.4.1 FRP Girder

3.2.4.1.1 Material Ultimate Strengths and Strains

The design ultimate tensile strength of any lamina from which a FRP tub girder is constructed in the longitudinal direction, f_{1t}, and transverse direction, f_{2t} shall be taken as:

$$f_{1t} = C_E f_{1t}^{*} \quad (3.2.4.1.1\text{-}1)$$

$$f_{2t} = C_E f_{2t}^{*} \quad (3.2.4.1.1\text{-}2)$$

The design ultimate compressive strength of any lamina from which a FRP tub girder is constructed in the longitudinal direction, f_{1c}, and transverse direction, f_{2c} shall be taken as:

$$f_{1c} = C_E f_{1c}^{*} \quad (3.2.4.1.1\text{-}3)$$

$$f_{2c} = C_E f_{2c}^{*} \quad (3.2.4.1.1\text{-}4)$$

The design ultimate shear strength of any lamina from which a FRP tub girder is constructed, f_6, shall be taken as:

$$f_6 = C_E f_6^* \quad (3.2.4.1.1\text{-}5)$$

The design ultimate tensile strain of any lamina from which a FRP tub girder is constructed in the longitudinal direction, ε_{1t}, and transverse direction, ε_{2t} shall be taken as:

$$\varepsilon_{1t} = C_E \varepsilon_{1t}^* \quad (3.2.4.1.1\text{-}6)$$

$$\varepsilon_{2t} = C_E \varepsilon_{2t}^* \quad (3.2.4.1.1\text{-}7)$$

The design ultimate compressive strain of lamina from which a FRP tub girder is constructed in the longitudinal direction, ε_{1c}, and transverse direction, ε_{2c} shall be taken as:

$$\varepsilon_{1c} = C_E \varepsilon_{1c}^* \quad (3.2.4.1.1\text{-}8)$$

$$\varepsilon_{2c} = C_E \varepsilon_{2c}^* \quad (3.2.4.1.1\text{-}9)$$

The design ultimate shear strain of lamina from which a FRP tub girder is constructed, γ_6, shall be taken as:

$$\gamma_6 = C_E \gamma_6^* \quad (3.2.4.1.1\text{-}10)$$

In Equations 2.4.1.1-1 through 2.4.1.1-10, C_E shall be taken as 0.85 for a carbon-based FRP, 0.65 for glass, and 0.75 for aramid.

The quantities $f_{1t}^*, f_{2t}^*, f_{1c}^*, f_{2c}^*, f_6^*, \varepsilon_{1t}^*, \varepsilon_{2t}^*, \varepsilon_{1c}^*, \varepsilon_{2c}^*,$ and γ_6^* are the ultimate tensile strengths and strains in the longitudinal and transverse directions, the ultimate compressive strengths and strains in the longitudinal and transverse directions, and ultimate shear strengths and strains for product certification as reported by the manufacturer, accounting for statistical reliability. In hybrid girders, where different types of fibers are used, different values of C_E shall be used for the corresponding materials. These values shall be confirmed or updated based on the results of coupon-level testing of witness panel samples manufactured concurrently with CT girders.

3.2.4.1.2 Modulus of Elasticity

The FRP tub girder material shall be treated as linearly elastic in tension, compression, and shear. The modulus of elasticity in the longitudinal direction, E_1, and the modulus of elasticity in the transverse direction, E_2, shall be calculated as:

$$E_1 = f_{1t}/\varepsilon_{1t} \quad (3.2.4.1.2\text{-}1)$$

$$E_2 = f_{2t}/\varepsilon_{2t} \quad (3.2.4.1.2\text{-}2)$$

and the shear modulus, G_6, shall be calculated as:

$$G_6 = f_6/\gamma_6 \qquad (3.2.4.1.2\text{-}3)$$

3.2.5 Distribution of Live Load to Girders

For the design of new structures and analysis of existing structures, vehicular live-load effects shall be distributed to individual girders by live-load distribution factors following AASHTO LRFD Section 4.6.2, calculated by:

- The approximate method of Section 4.6.2.2, assuming CT girders to behave as concrete box girders (type "c" sections in Table 4.6.2.2.1-1) in Tables 4.6.2.2.2b-1, 4.6.2.2.2d-1, 4.6.2.2.2e-1, 4.6.2.2.3a-1, 4.6.2.2.3b-1, and 4.6.2.2.3c-1, subject to corresponding limits of applicability
- Results of detailed, three-dimensional finite element analysis
- Other approved structural analysis techniques such as the grillage method which adequately capture lateral load distribution

3.2.6 Limit States

3.2.6.1 Service Limit State

Under service loads, CT members shall be analyzed as linearly elastic structures. Checks to be performed at the service limit state shall be related to and limited by deformations as specified in Article 2.11 for CT girders under flexure. The loads to be considered in this analysis shall be as defined in Section 3 of AASHTO LRFD.

3.2.6.2 Fatigue and Creep Rupture Limit State

The maximum longitudinal tensile stress in portions of a CT girder consisting of FRP under all sustained loads plus fatigue loading shall not exceed the following limits given by AASHTO LRFD CFFT (2012):

- For carbon-based FRP: $0.55f_{1t}$
- For glass-based FRP: $0.20f_{1t}$
- For aramid-based FRP: $0.30f_{1t}$

The loads to be considered in this analysis consist of all permanent loads, and the fatigue load as defined in Article 3.6.1.4 of AASHTO LRFD. The load factors for DC, DW, EV, and EH shall be 1.0 and the fatigue load factor shall be 1.0 with an impact allowance of 1.15. This check is made on the base cross-section, and the cyclic fatigue resistance in accordance with the AASHTO Fatigue I or II limit state shall also be assessed for specific details if deemed necessary by the engineer.

3.2.6.3 Strength Limit State

3.2.6.3.1 General

The strength limit states shall consider material strength and stability. Design resistance shall be the product of nominal resistance as determined in accordance with the applicable provisions of Articles 3.2.8, 3.2.9, and 3.2.10 unless another limit state is specifically identified, and the resistance factor as specified in Article 3.2.6.3.2. and AASHTO LRFD CFFT (2012). The loads to be considered in this analysis shall be as defined in Section 3 of AASHTO LRFD.

3.2.6.3.2 Resistance Factors

For CT girders in flexure the resistance factor ϕ shall be taken as 0.75 for FRP rupture, FRP compressive failure, and concrete crushing.

For CT girders in shear the strength resistance factor ϕ shall be taken as 0.75.

For CT girder webs subject to shear buckling, the resistance factor ϕ shall be taken as 0.35.

For concrete crushing around shear studs due to horizontal shear, the resistance factor ϕ shall be taken as 0.85.

For steel shear studs in bearing carrying horizontal shear the resistance factor ϕ shall be taken as 0.75.

For friction connections between the girder and deck that are subject to horizontal shear and that rely on interaction between purposely deformed surfaces, the resistance factor ϕ shall be taken as 0.90.

3.2.6.3.3 Stability

The structure consisting of CT girders as a whole and its components shall be designed to resist sliding, overturning, and uplift. Effects of load eccentricity shall be considered in the analysis and design. The girder shall be proportioned and/or braced to ensure stability during all phases of construction and while in service.

3.2.6.4 Extreme Event Limit State

The structure consisting of CT girder members as a whole and its components shall be proportioned to resist collapse due to extreme events, specified in Table 3.4.1-1 of AASHTO LRFD, as may be appropriate to the site and application.

3.2.7 Design Considerations

3.2.7.1 General

Components and connections shall be designed to resist load combinations as specified in Section 3 of AASHTO LRFD, at all stages during the life of the structure, including those during construction. Load factors shall be specified in Section 3 of AASHTO LRFD, with additional permanent load factors as defined in Article 3.2.6.2 for the fatigue and creep rupture limit state.

As specified in Section 4 of AASHTO LRFD, equilibrium and strain compatibility shall be maintained in the analysis.

3.2.7.2 Effect of Imposed Deformation

The effect of imposed deformation due to shrinkage, temperature change, creep and support movement shall be included as required by specific limit states defined in Section 3 of AASHTO LRFD.

3.2.8 Design for Flexure

3.2.8.1 General

The following assumptions may be used to determine the flexural resistance of CT girders at the limit states indicated:

3.2.8.1.1 Assumptions for Service, Fatigue and Creep Rupture Limit States

- CT girder stresses and deflections due to loads applied prior to the time at which the girder behaves compositely with the concrete deck are computed based only on the FRP girder section
- CT girder stresses and deflections due to loads applied after the time at which the girder behaves compositely with the concrete deck are computed assuming full composite action between the CT girder and concrete deck
- Longitudinal strains vary linearly over the depth of the section and are proportional to the distance from the neutral axis
- The tensile strength of concrete is neglected

3.2.8.1.2 Assumptions for Strength and Extreme Event Limit States

- CT girder stresses and deflections due to loads applied prior to the time at which the girder behaves compositely with the concrete deck are computed based only on the FRP girder section
- CT girder stresses and deflections due to loads applied after the time at which the girder behaves compositely with the concrete deck are computed assuming full composite action between the CT girder and concrete deck
- Longitudinal strains vary linearly over the depth of the section and are proportional to the distance from the neutral axis
- The tensile strength of concrete is neglected
- Concrete experiences crushing at a compressive strain $\varepsilon_{cu} = 0.003$
- Tensile failure is defined by tensile rupture of the CT girder's bottom flange under uniaxial longitudinal stresses. Compressive failure is defined by the crushing of the concrete under uniaxial longitudinal stresses.
- The concrete stress-strain relationship proposed by Hognestad (1951), AASHTO (2012), or another representation of the concrete stress-strain relationship that has been

experimentally validated, is used when calculating the ultimate moment capacity based on equilibrium and strain compatibility.

3.2.8.2 Non-Composite Flexural Resistance

Between placing of the concrete deck and its full cure or attachment to the girders, the deck and girders are assumed not to act compositely, with the weight of wet concrete being applied fully to the bare CT girders, and the section is assumed to be adequately proportioned and braced to prevent any local or global buckling. In this condition, the flexural resistance of the CT girder is taken as:

$$M_r = \min(\phi M^+, \phi M^-) \tag{3.2.8.2-1}$$

where:

$$M^+ = \frac{E_{bf}\varepsilon_{1tbf}I_{NC}}{n_{bf}\bar{y}_{NC}} \tag{3.2.8.2-2}$$

$$M^- = \frac{E_{tf}\varepsilon_{1ctf}I_{NC}}{n_{tf}(d - \bar{y}_{NC})} \tag{3.2.8.2-3}$$

where:

$E_{bf} =$	effective bending modulus of the bottom flange (ksi)
$E_{tf} =$	effective bending modulus of the bottom flange (ksi)
$\varepsilon_{1tbf} =$	reduced ultimate tensile strain for the bottom flange
$\varepsilon_{1ctf} =$	reduced ultimate compressive strain for the top flange
$n_{bf} =$	modular ratio of the bottom flange
$n_{tf} =$	modular ratio of the top flange
I_{NC}	transformed moment of inertia of the non-composite section (in.^{4})
$\bar{y}_{NC} =$	height of the neutral axis (measured from the bottom of the section) of the non-composite section (in.)

$d =$ depth of the non-composite CT girder section (in.)

3.2.8.3 Composite Flexural Resistance

Once the CT girder's deck is fully connected to the girder after sufficient concrete curing, the deck is assumed to act compositely with the girders. In general, the girder section can fail by either bottom flange tensile rupture or concrete crushing at the extreme fiber. However, flexural stresses in the girder due to girder self-weight and wet concrete acting on the non-composite section must be considered for bottom flange tensile rupture. The controlling failure mode will be the mode that corresponds to the lowest moment that can be carried by the composite section.

In the case of tensile rupture, the tensile strain in the bottom flange corresponding to failure due to moment acting on the composite section, ε_{1t}^{C}, is given by Equation 3.2.8.3-1. The nominal moment capacity of the composite section corresponding to the occurrence of ε_{1t}^{C} is denoted by M_n^C, and the Strength I moment limit state can then be expressed as shown in Equation 3.2.8.3-2. Factored temperature or shrinkage-induced strains may also be subtracted from ε_{1t} in Equation 3.2.8.3-1 but are not shown here for clarity.

$$\varepsilon_{1t}^{C} = \varepsilon_{1t} - \varepsilon_{DC} \tag{3.2.8.3-1}$$

$$M_r^C = \phi M_n^C \geq \gamma_{LL} M_{LL+IM} + \gamma_{DC} M_{DC} + \gamma_{DW} M_{DW} \tag{3.2.8.3-2}$$

where:

$\phi =$ resistance factor for flexure

$\varepsilon_{1t} =$ ultimate tensile strain reduced by C_E and appropriate statistical reliability factors

$\varepsilon_{DC} =$ bottom flange strain caused by factored dead load moments acting on the non-composite section

$M_{DC} =$ dead load moment of components and attachments acting on the composite section (kip-in.)

$M_{DW} =$ dead load moment due to wearing surface acting on the composite section (kip-in.)

$M_{LL+IM} =$ live load moment with impact acting on the composite section (kip-in.)

$\gamma_{LL}, \gamma_{DC}, \gamma_{DW} =$ load factors for appropriate loadings

In contrast to tension failure, failure due to concrete crushing will be caused only by factored moments acting on the composite section. The flexural capacity of the composite CT girder can be determined by either the detailed or simplified methods presented here.

3.2.8.4 Detailed Method for Computing Composite Flexural Resistance

In the detailed method, the flexural capacity of the composite section is found by determining the smallest design moment at which any of its components experience flexural failure while rigorously accounting for the nonlinear stress-strain behavior of the concrete deck in compression. The assumption of plane sections is enforced. These determinations require the use of moment-curvature analysis, an iterative procedure that locates the section neutral axis at failure by ensuring internal force equilibrium followed by the summation of the contributions of all components to the resisting moment. Details of this method as implemented assuming a Hognestad curve (Hognestad 1951) for the concrete in compression are presented in Appendix B. Other concrete compressive stress-strain curves that are in agreement with experimental data may be used at the discretion of the engineer.

3.2.8.5 Composite Flexural Resistance – Simplified Analysis

Assumptions:

- Webs and top flange carry no longitudinal stress

- Bottom flange carries tensile stress uniformly

- Deck carries compressive stress (no tension) assuming a rectangular distribution if section fails by concrete crushing, or linearly varying stresses if section fails by bottom flange rupture

The linearly varying stress distribution used in the case of bottom flange rupture conservatively approximates the parabolic distribution of concrete in compression as described by Equation 3.2.8.5.2-3, which only requires the determination of stresses at the top and bottom of the deck. This parabolic distribution is given by AASHTO (2012), which references Desayi and Krishnan (1964) and Todeschini et al (1964).

The section's moment capacity is determined as the smaller of M_{n1} and M_{n2}, the capacities calculated assuming failure by concrete crushing and bottom flange rupture, respectively.

3.2.8.6 Failure by Concrete Crushing

For this check, the section is assumed to fail due to concrete crushing with an extreme compression fiber strain equal to 0.003 with additional strain capacity available in the bottom flange prior to rupture. Using plane section assumptions, the depth of the neutral axis at concrete crushing, c, is determined by solving:

$$0.85f'_c b_c \beta_1 c^2 + 0.003 A_{bf} E_{bf} c - 0.003 A_{bf} E_{bf} \left(D - \frac{t_{bf}}{2} \right) = 0 \quad (3.2.8.5.1\text{-}1)$$

where:

$b_c =$ effective width of the deck over the CT girder (in.)

$A_{bf} =$ cross-sectional area of the bottom flange (in.^{2})

$\beta_1 =$ Whitney's stress block ratio (5.7.2.2)

Once determined, c is used to calculate moment capacity as:

$$M_1 = A_{bf} E_{bf} \varepsilon_{bf} \left(D - \frac{t_{bf} + \beta_1 c}{2} \right) \quad (3.2.8.5.1\text{-}2)$$

where:

$\varepsilon_{bf} = 0.003 * \dfrac{D - c - {t_{bf}}/{2}}{c}$ strain in the center of the bottom flange at concrete crushing

3.2.8.6.1 Failure by Bottom Flange Rupture

For this check, the section is assumed to fail due to bottom flange rupture with an extreme tension fiber strain equal to ε_{1t}^*, the ultimate tensile strain of the bottom flange's main longitudinal reinforcement, with additional strain capacity available in the deck prior to concrete crushing.

Using plane section assumptions, the depth of the neutral axis at bottom flange rupture, c, is determined iteratively until internal force equilibrium is achieved. For a given estimate of c, the strains at the top and bottom of the deck are calculated, respectively, as:

$$\varepsilon_{ct} = \frac{\varepsilon_{1t}^C c}{D - c} \quad (3.2.8.5.2\text{-}1)$$

$$\varepsilon_{cb} = \frac{\varepsilon_{1t}^C (c - t_c)}{D - c} \quad (3.2.8.5.2\text{-}2)$$

where:

$t_c =$ thickness of the deck above the CT girder (in.)

The general expression for the corresponding stresses at the top and bottom of the deck is found are given in Equation 3.2.8.5.2-3, although for the case where ε_{cb} is tensile, the lower part of the deck is in tension and $f_{cb} = 0$:

$$f_{ct,cb} = \frac{1.8{f'}_c \, {\varepsilon_{ct,cb}}/{\varepsilon_0}}{1 + \left({\varepsilon_{ct,cb}}/{\varepsilon_0}\right)^2} \tag{3.2.8.5.2-3}$$

where the concrete strain corresponding to peak compressive stress is expressed as:

$$\varepsilon_0 = 1.71\frac{{f'}_c}{E_c} \tag{3.2.8.5.2-4}$$

The compressive force resultant provided by the concrete is then determined as:

$$C = \frac{1}{2} f_{ct} c b_c, \qquad c \le t_c \tag{3.2.8.5.2-5a}$$

$$C = \frac{1}{2} b_c t_c (f_{ct} + f_{cb}), \qquad c > t_c \tag{3.2.8.5.2-5b}$$

The value of *C* is compared with the tensile force resultant provided by the bottom flange, found as:

$$T = \varepsilon_{1t}^{aC} E_{bf} A_{bf} \tag{3.2.8.5.2-6}$$

and c updated until $T = C$ within a reasonable tolerance. The moment capacity under this failure assumption is then found as:

$$M_2 = \varepsilon_{1t}^{C} E_{bf} A_{bf} \left(D - \frac{t_{bf}}{2} - \frac{c}{3}\right), \qquad c \le t_c \tag{3.2.8.5.2-7a}$$

$$M_2 = \varepsilon_{1t}^{C} E_{bf} A_{bf} \left(D - \frac{t_{bf}}{2} - \frac{t_c(2f_{ct} + f_{cb})}{3(f_{ct} + f_{cb})}\right), \qquad c > t_c \tag{3.2.8.5.2-7b}$$

After the composite moment under assumed failure of each component has been calculated, the controlling, available composite moment resistance of the section is found as

$$M_r^C = \phi M_n^C = \min(\phi M_1, \phi M_2) \tag{3.2.8.5.2-8}$$

3.2.9 Design for Shear

3.2.9.1 General

The critical section for shear in a CT girder member shall be determined in accordance with the provisions of AASHTO LRFD for reinforced concrete members.

In lieu of the method specified here, the resistance of members in shear may be determined by satisfying the conditions of equilibrium and compatibility of strains and by using experimentally verified stress-strain relationships for FRP webs.

3.2.9.2 Nominal Shear Resistance

The section's shear resistance is found assuming negligible contributions from the flanges and deck as:

$$V_r = \phi V_n \tag{3.2.9.2-1}$$

$$V_n = \frac{I_c t_{w-fs} f_{6w}}{Q_t} \tag{3.2.9.2-2}$$

where:

$\phi =$ resistance factor for FRP in shear

$I_C =$ moment of inertia (second moment of area) of the composite girder section (in.^{4})

$t_{w-fs} =$ thickness of the webs, less the thickness of the sandwich core (in.)

$f_{6w} =$ reduced ultimate shear stress of the webs (ksi)

$Q_t =$ first moment of area of the portion of the girder section above the location of maximum web shear stress taken about the girder neutral axis (in.^{3})

This approach does not rigorously incorporate the fact that loads acting on the non-composite section will produce shear stresses at a different location within the web based on non-composite response, and the maximum shear stress acting on the non-composite section is therefore under-estimated. However, this is offset by the assumption that all shear stresses act on the composite section and therefore maximum stresses due to all phases of loading are assumed to be at the same location.

3.2.9.3 Web Shear Buckling

Slender CT girder webs can be subject to web shear buckling. Shear buckling itself is a complex phenomenon, which is further complicated by the orthotropic nature of FRP and the interaction between face sheets and the core in sandwich composites. For these reasons, and the highly case-dependent nature of the problem, a rational, closed form solution for web shear buckling is not available. Therefore, numerical techniques such as finite-element analysis must be used to rigorously assess web shear buckling. As an example, several web laminate architectures based on a typical 24.2 oz/yd^2 biaxial, E-glass fabric were modeled and analyzed for eigenvalue shear buckling. Development of these models is detailed in Appendix C. The models assumed orthotropic, elastic response of the face sheets with moduli of 5340 ksi and 1650 ksi in the local 1 (fiber) and 2 (normal to fiber) directions respectively. When the web face sheets are oriented at ±45°, the resulting moduli are 2780 ksi in both the global *x* (girder span) and *y* (web depth) directions. The modulus of the isotropic, elastic foam core web was taken to be 15.9 ksi. The results of these analyses are presented in the figures below which cover a wide range of common web designs using these typical E-glass and foam core materials, with intermediate web heights available by interpolation. In these figures, the term "Face Sheet" refers to the thickness of a single face sheet t_{sheet}; a single girder web will therefore have two face sheets, and a CT girder will have a total of four face sheets. Other variables are defined below.

$t_{sheet} =$	thickness of single face sheet (in.)
$t_{core} =$	thickness of core material (in.)
$t_{web} =$	total web thickness (in.), or $2t_{sheet} + t_{core}$
$N_{xy-cr} =$	critical shear buckling stress resultant for a single web (kip/in.)
$h_{web} =$	web height (in.)

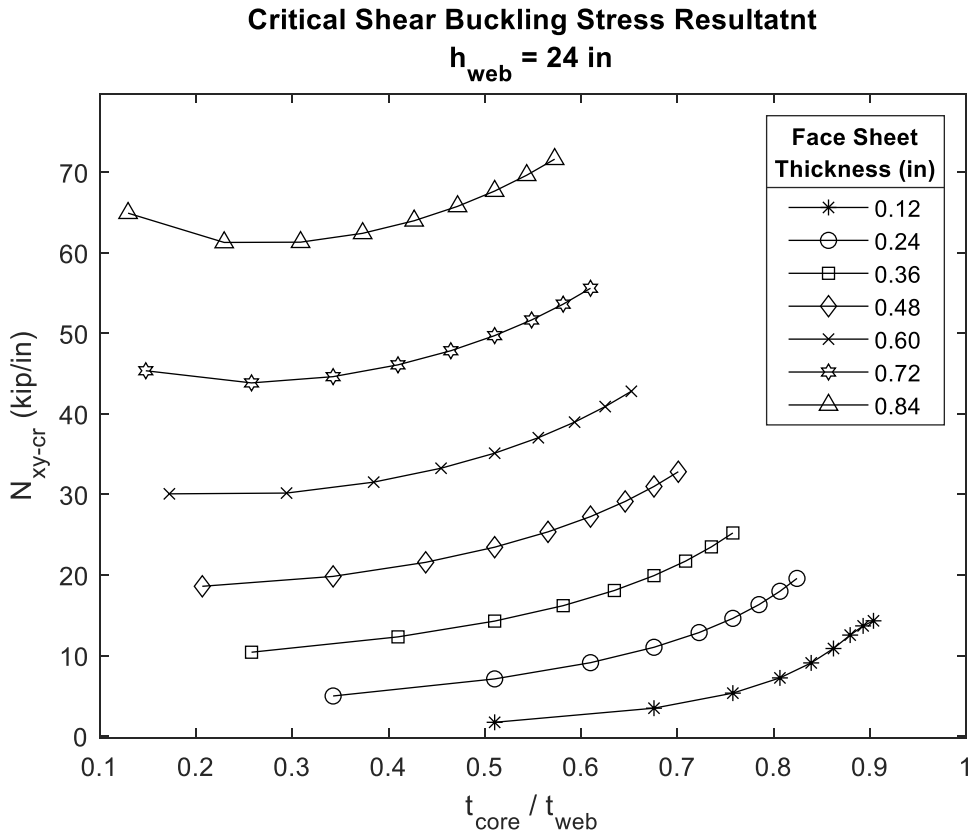
Critical Shear Buckling Stress Resultatnt
h_web = 24 in
Face Sheet Thickness (in)
0.12
0.24
0.36
0.48
0.60
0.72
0.84
N_xy-cr (kip/in)
t_core / t_web
0
10
20
30
40
50
60
70
0.1
0.2
0.3
0.4
0.5
0.6
0.7
0.8
0.9
1

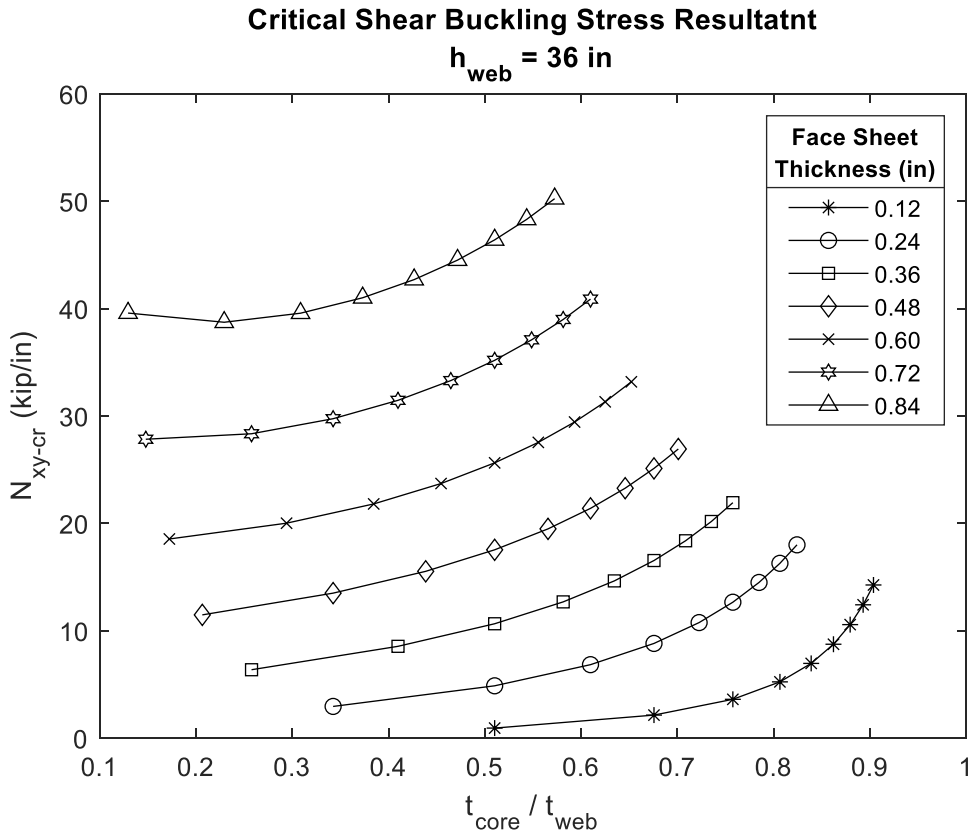
Critical Shear Buckling Stress Resultatnt
h_web = 36 in
Face Sheet Thickness (in)
0.12
0.24
0.36
0.48
0.60
0.72
0.84
N_xy-cr (kip/in)
t_core / t_web
0
10
20
30
40
50
60
0.1
0.2
0.3
0.4
0.5
0.6
0.7
0.8
0.9
1

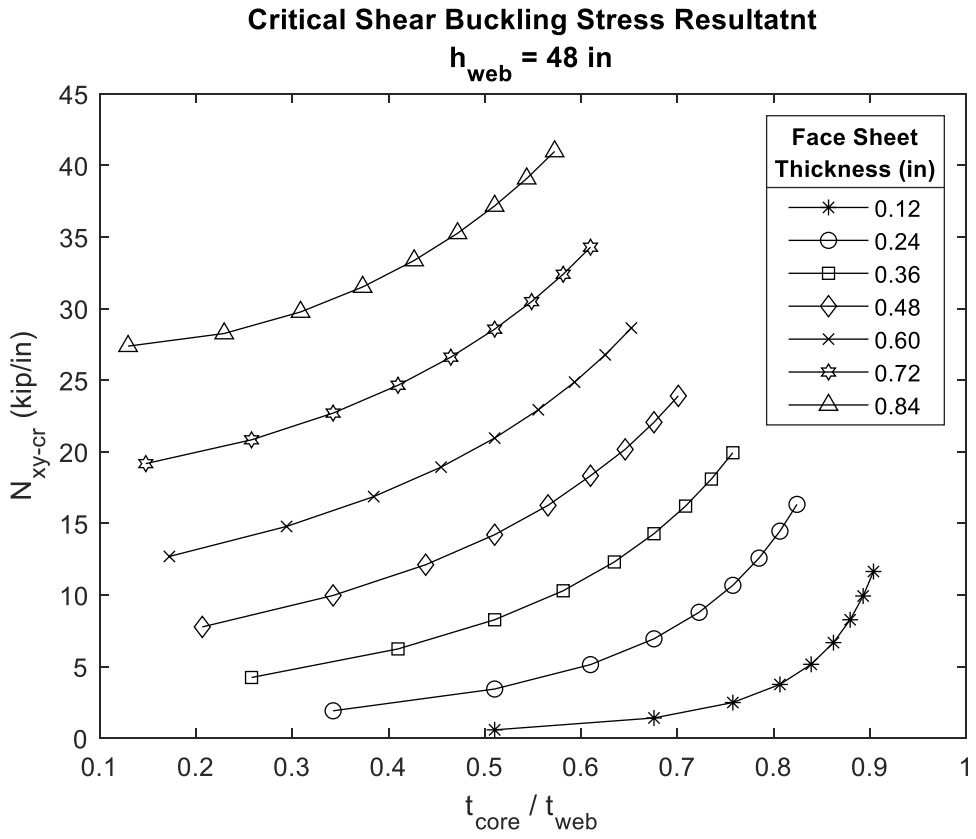
Critical Shear Buckling Stress Resultatnt
h_web = 48 in
N_xy-cr (kip/in)
t_core / t_web
Face Sheet Thickness (in)
0.12
0.24
0.36
0.48
0.60
0.72
0.84

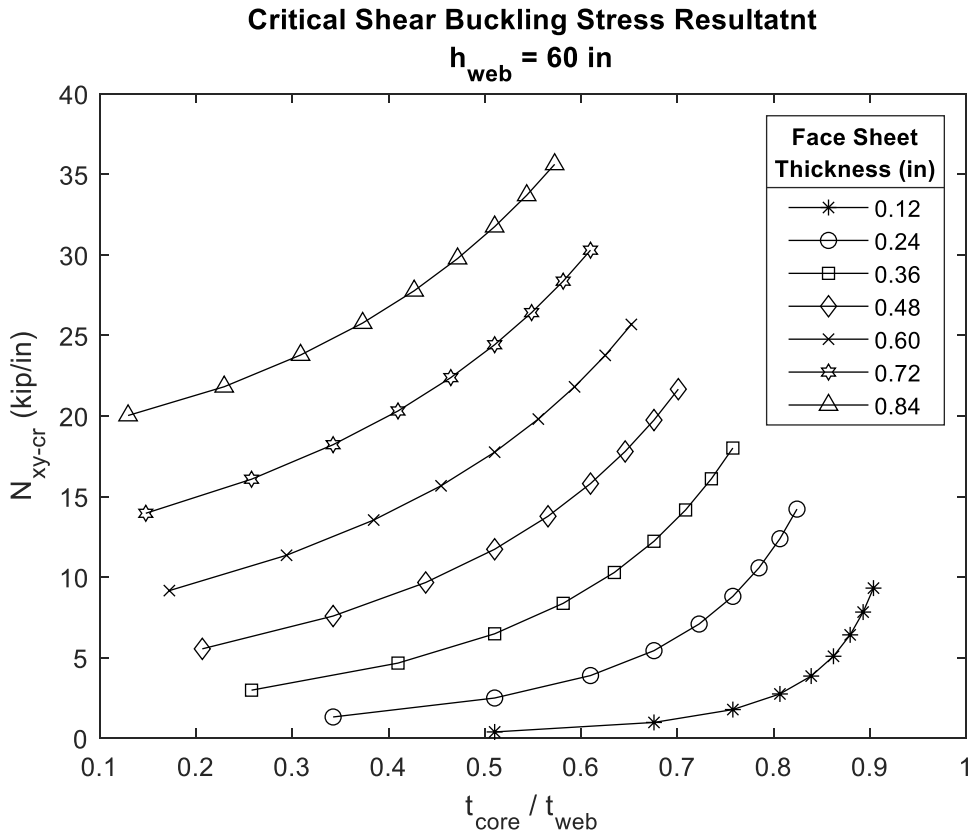
Critical Shear Buckling Stress Resultatnt
h_web = 60 in
N_xy-cr (kip/in)
t_core / t_web
Face Sheet Thickness (in)
0.12
0.24
0.36
0.48
0.60
0.72
0.84

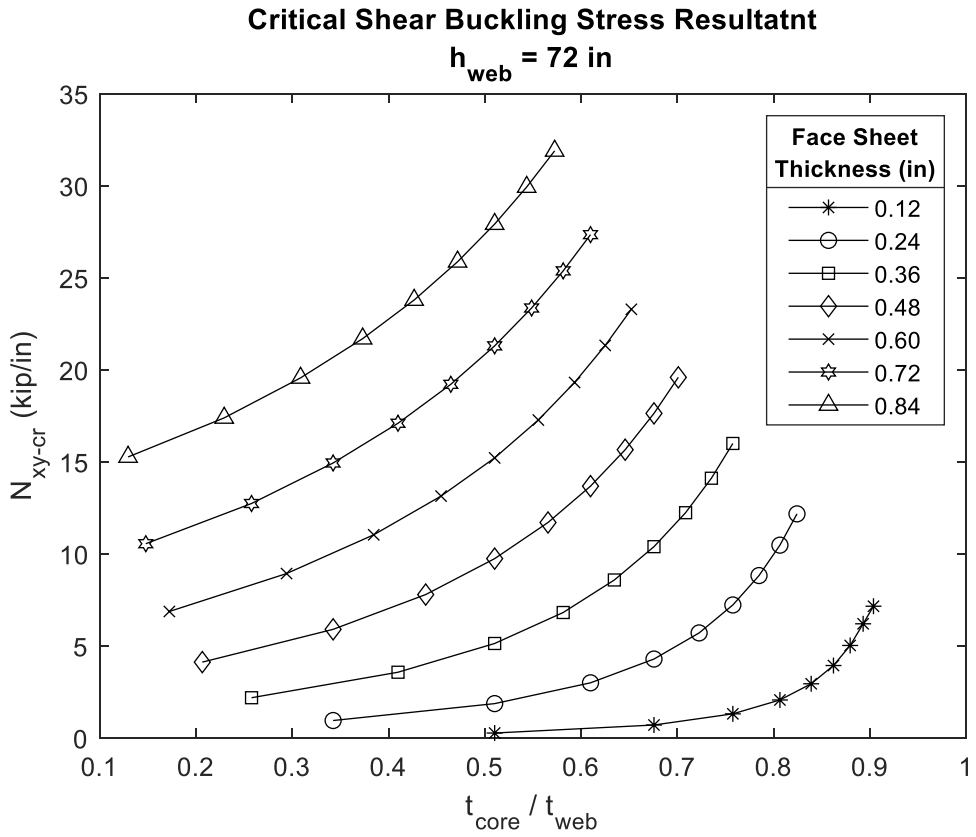

Using the charts provided above (or similar charts produced by finite-element simulation for other girder dimensions and/or face sheet properties), the value of the shear stress resultant causing shear buckling is found and when multiplied by the web height, h_{web}, gives the critical load causing shear buckling of a single web. Examples of the use of these charts to assess web buckling in design are provided in Appendix D.

3.2.10 Shear Connectors

3.2.10.1 General

The FRP tub girder and reinforced concrete deck shall be made composite with bearing-type shear studs or ridged friction connections that have been experimentally demonstrated to provide adequate fatigue and strength resistance as defined here. The ridged friction connection requires a deformed or rough upper surface on the tops of the girder top flanges. Other girder-deck shear connectors shall only be used if they have been experimentally demonstrated to provide adequate strength and fatigue resistance.

3.2.10.2 Bearing Shear Connectors

Where bearing-type stud shear connectors are used for girder-deck shear connection, they shall be designed for the limit states of fatigue and strength in accordance with section 6.10.10 of AASHTO LRFD. Stud spacing *s* will be constant along the entire girder span unless a more

sophisticated analysis that meets the standards of AASHTO LFRD is performed that justifies varying *s* along the girder span.

3.2.10.2.1 Strength Limit State

The design shear resistance of a single stud connector, Q_r, at the strength limit state shall be taken as:

$$Q_r = \phi Q_n \qquad (3.2.10.2.1\text{-}1)$$

where:

$\phi =$ resistance factor for stud shear connectors

$Q_n =$ nominal shear resistance of a single shear connector determined as specified below (kip)

The nominal shear resistance of one stud connector, Q_n, embedded in a concrete deck shall be taken as the minimum of Q_1, Q_2 and Q_3 as defined below.

$$Q_1 = 0.5 A_{sc} \sqrt{f'_c E_c} \qquad (3.2.10.2.1\text{-}2a)$$

$$Q_2 = A_{sc} f_u \qquad (3.2.10.2.1\text{-}2b)$$

$$Q_3 = f_{tb} d_s t_{tf} \qquad (3.2.10.2.1\text{-}2c)$$

where:

$A_{sc} =$ cross-sectional area of a stud connector (in.^{2})

$f'_c =$ specified 28-day compressive strength of the deck concrete (ksi)

$E_c =$ modulus of elasticity of the deck concrete determined as specified in Article 5.4.2.4 of AASHTO LRFD

$f_u =$ specified minimum tensile strength of a stud connector (ksi)

$f_{tb} =$ bearing strength of the FRP making up the girder's upper flanges (ksi)

$d_s =$ diameter of a stud connector (in.)

$t_{tf} =$ thickness of the girder's upper flanges (in.)

At the strength limit state, the design strength of the most heavily loaded shear stud shall equal or exceed the shear flow (including appropriate load factors) to which it is subjected. That is,

$$Q_r \geq \frac{V_u Q_{int}}{n I_c} s \qquad (3.2.10.2.1\text{-}3)$$

where:

$n =$ total number of shear studs spaced at s

$V_u =$ maximum factored shear load (kip)

$Q_{int} =$ first moment of area of the concrete deck taken about the interface between the top flange and deck (in.^{3})

$I_c =$ moment of inertia (second moment of area) of the composite girder section (in.^{4})

$s =$ Shear stud spacing (in.)

3.2.10.2.2 Fatigue Limit State

Only the Fatigue I load combination corresponding to infinite fatigue life shall be used. The shear stud grade and type shall have been experimentally demonstrated to possess adequate fatigue resistance (for example, see Davids et al. 2022a, where ASTM A490 fasteners with no threads in the shear plane were demonstrated to possess sufficient fatigue resistance in a bearing-type connection).

3.2.10.3 Ridged Friction Connections

Where ridged friction-type connectors are used, they shall be designed under the strength limit state as a frictional interface shear transfer mechanism as described in section 5.7.4 of AASHTO LRFD. The upper surface of the girder flanges shall have surface deformations (typically ridges) with sufficient size and spacing to ensure interlock between the concrete deck and girders and strain compatibility at the girder-deck interface. As such, intermittent shear reinforcement in the form of shear studs at a spacing L_{vi} shall be provided to apply a clamping force between the girder 's upper flange and deck.

3.2.10.3.1 Strength Limit State

The design interface shear flow resistance, v_r, shall be taken as:

$$v_r = \phi v_n \tag{3.2.10.3-1}$$

where:

$\phi =$ resistance factor for interface shear transfer

$v_n =$ nominal interface shear flow resistance (kip/in.)

The nominal shear flow resistance of the ridged connection shall be taken as:

$$v_n = c_{cf} b_t + \mu \frac{A_{vf} f_y + P_c}{L_{vi}} \tag{3.2.10.3-2}$$

but shall not be taken greater than the least of:

$$v_n \leq K_1 f'_c b_t \tag{3.2.10.3-3}$$

$$v_n \leq K_2 b_t \tag{3.2.10.3-4}$$

$$v_n \leq \frac{f_{vr} w_r b_t}{s_r} \tag{3.2.10.3-5}$$

where:

$c_{cf} =$ cohesion factor between concrete and FRP, taken as zero unless determined by laboratory test

$b_t =$ width of the girder's top flanges (in.)

$\mu =$ friction factor between FRP ridges and concrete, taken equal to one

$A_{vf} =$ area of clamping studs within L_{vi} (in.^{2})

$f_y =$ yield strength of clamping studs, not to exceed 60 (ksi)

$P_c =$ permanent net compressive force normal to shear plane; if tensile, $P_c = 0$ (kip)

$K_1 =$ fraction of concrete strength available to resist interface shear, specified in Article 5.7.4.3 of AASHTO LRFD

$f'_c =$	specified 28-day compressive strength of the deck concrete (ksi)
$K_2 =$	limiting shear resistance, specified in Article 5.7.4.3 of AASHTO LRFD (ksi)
$f_{vr} =$	shear strength of the resin making up the connection ridges (ksi)
$w_r =$	width of shear ridges (in.)
$s_r =$	shear ridge spacing (in.)

3.2.10.3.2 Fatigue Limit State

The ridged friction-type connectors must be experimentally or analytically demonstrated to satisfy requirements of the Fatigue I limit state.

3.2.11 Control of Deflections

CT girder sections shall be designed with adequate stiffness to ensure deflections are less than maximum values set by the Owner. Typical deflection limits enforced by Owners are defined in AASHTO LRFD, Article 3.2.5.2.6, with the analysis method used conforming to the requirements of Section 4.4, and linearly elastic behavior (as outlined in AASHTO LRFD, Article 4.5.2.2) assumed.

Deflections can be decreased by increasing the effective flexural stiffness of the section through modification of its material properties, dimensions, or both as long as the section retains adequate strength and stability. Some possible alterations are:

- Increasing the number of longitudinal, uniaxial laminae in the bottom flange
- Using a higher percentage of stiffer laminae (for instance carbon laminae as opposed to glass laminae) in the bottom flange
- Increasing the section's depth by increasing the web's depth, decreasing its splay angle, or both
- Increasing the thickness of the deck slab

4 References

AASHTO (2012). *Guide Specifications for Design of Bonded FRP Systems for Repair and Strengthening of Concrete Bridge Elements*. Washington, D.C.: AASHTO.

AASHTO (2017). *LRFD Bridge Design Guide*. Washington, D.C.: AASHTO.

AASHTO (2012). *LRFD Guide Specifications for Design of Concrete-Filled FRP Tubes for Flexural and Axial Members*. Washington, D.C.: AASHTO.

Airtex. (2020). *Airex T92 Technical Data Sheet*. 3A Composites, Nigh Point, NC.

AIT (2019). *Calculation Package for Grist Mill Bridge No. 2334 Over Soudabscook Stream Hampden, Maine.* Advanced Infrastructure Technologies, Brewer, ME.

ASTM International. (2015). *D3917-15a: Standard Specification for Dimensional Tolerance of Thermosetting Glass-Reinforced Plastic Pultruded Shapes*. West Conshohocken, PA.

ASTM International. (2017). *D8067/D8067M-17: Standard Test Method for In-Plane Shear Properties of Sandwich Panels Using a Picture Frame Fixture*. West Conshohocken, PA.

Dagher HJ, Anderson J, Davids WG, & Clapp JD (2019). "Hybrid composite concrete bridge and method of assembling." U.S. Patent No. 10,494,779, issued Dec. 3, 2019.

Davids WG, Diba A, Dagher HD, Guzzi D, & Schanck AP (2022). Development, assessment and implementation of a novel FRP composite girder bridge. *Construction and Building Materials*, 340(July), 127818.

Dassault Systèmes. (2019). *ABAQUS 2019* [Computer Software]; Vélizy-Villacoublay, France.

Davids, W.G., Diba, A., Dagher, H.J., Guzzi, D., & Schanck, A.P. (2022a). Development, assessment and implementation of a novel FRP composite girder bridge. *Construction and Building Materials*, Volume 340: https://doi.org/10.1016/j.conbuildmat.2022.127818.

Davids WG, Guzzi D and Schanck AP (2022b). Development and experimental assessment of friction-type shear connectors for FRP bridge girders with concrete decks. *Materials* 15(9), 3014; https://doi.org/10.3390/ma15093014.

Davids, W.G. & Schanck, A.P. (2022). Field load testing and analysis of a new FRP composite tub girder bridge with a concrete deck. *Proceedings of the IBAMAS 11th International Conference on Bridge Maintenance, Safety and Management*. Barcelona, Spain.

Desayi, P. & Krishnan, S. (1964). Equation for the stress-strain curve of concrete. *Journal of the American Concrete Institute*. 61(3):345-350.

Diba, A. & Hepler I. (2019). *Milestone 12: Structural testing of first prototype*. University of Maine, Orono, ME.

GOM. (2019). *GOM Correlate/ARAMIS* [Computer Software]. GOM; Braunschweig, Germany.

Guzzi, D. (2019). *Shear Connectors for Hybrid Composite FRP-Concrete Bridge Girders*. Master's thesis, University of Maine, Orono, Maine, USA.

Hognestad, E. (1951). *A study of combined bending and axial load in reinforced concrete members*. Urbana, IL: University of Illinois.

Morgenthaler, M., Berger, L., Feichtinger, K., & Elkin, R. (2005). Dependence of Inplane Sandwich Shear Deformation on Core Material, Type, and Thickness. In: Sandwich Structures 7: Advancing with Sandwich Structures and Materials. Aalborg, Denmark.

Oludare, E. & Toubia, E.A. (2019). In-Plane Shear Characterization of Composite GFRP-Foam Sandwich Panels. Jounral of Composite for Construction. 23(5): 04019034-2.

Schanck, A.P. (2021). *Determination of Bridge Behavior through Live-load Testing and Advanced Numerical Analysis.* Doctoral dissertation, University of Maine, Orono, Maine, USA.

Schanck, A. & Davids W. (2021). *Testing, Monitoring, and Analysis of FRP Girder Bridge with Concrete Deck*. University of Maine, Orono ME.

Stoll, F.C., & Johnston, N.G. (2016). In-plane shear characterization of sandwich laminates using a picture-frame test configuration, presented at American Society of Composites 31st Technical Conference, Williamsburg, VA.

Todeschini, C.E., Bianchini, A.C., & Kesler, C.E. (1964). Behavior of concrete columns reinforced with high strength steels. *ACI Journal*. 61(6):701-716.

Vectorply. (2015). *E-LR 2410 Technical Data Sheet.* Vectorply Corporation, Phenix City, AL.

Appendix A: Average Strain Plots

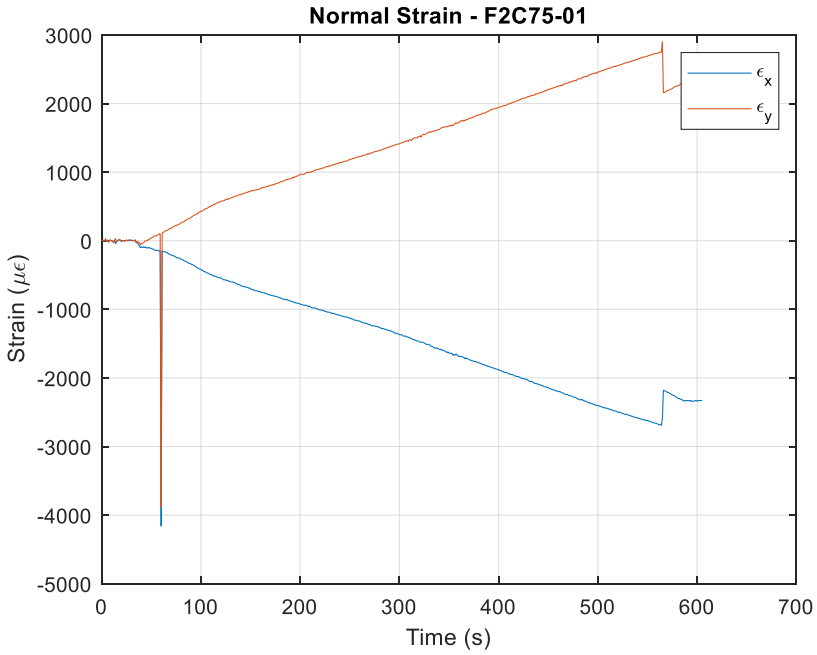

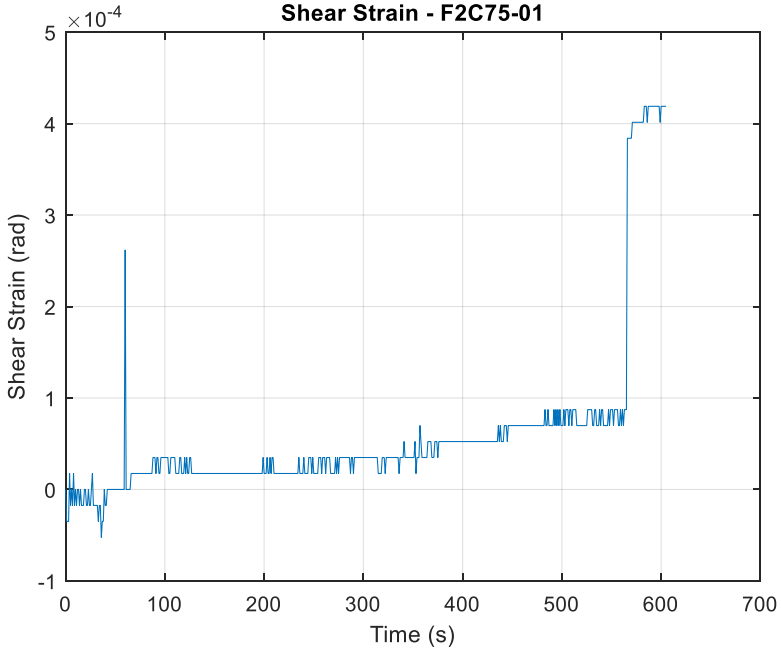

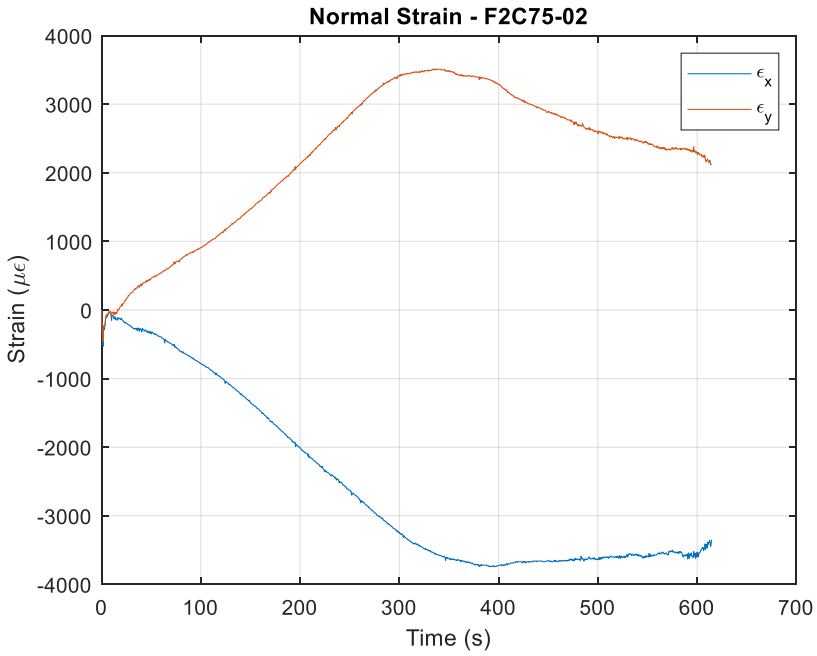
Normal Strain - F2C75-02
Strain ($\mu\epsilon$)
Time (s)
ϵ_x
ϵ_y
4000
3000
2000
1000
0
-1000
-2000
-3000
-4000
0
100
200
300
400
500
600
700

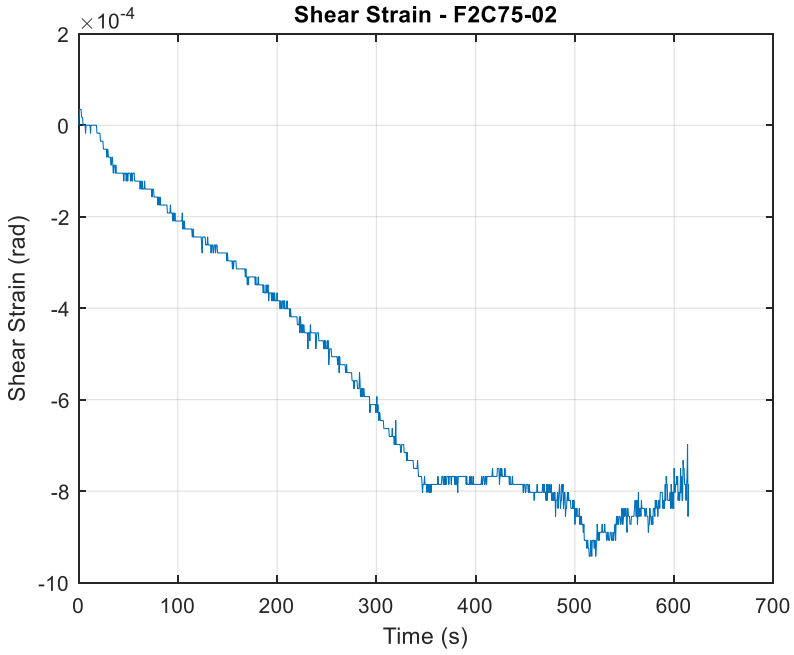
Shear Strain - F2C75-02
$\times 10^{-4}$
Shear Strain (rad)
Time (s)
2
0
-2
-4
-6
-8
-10
0
100
200
300
400
500
600
700

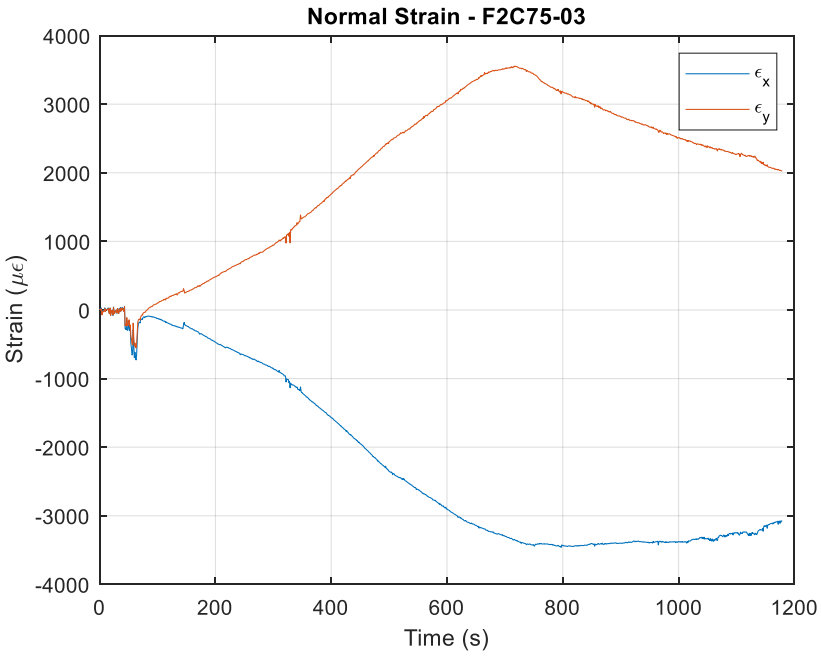
Normal Strain - F2C75-03
Strain ($\mu\epsilon$)
Time (s)
ϵ_x
ϵ_y
4000
3000
2000
1000
0
-1000
-2000
-3000
-4000
0
200
400
600
800
1000
1200

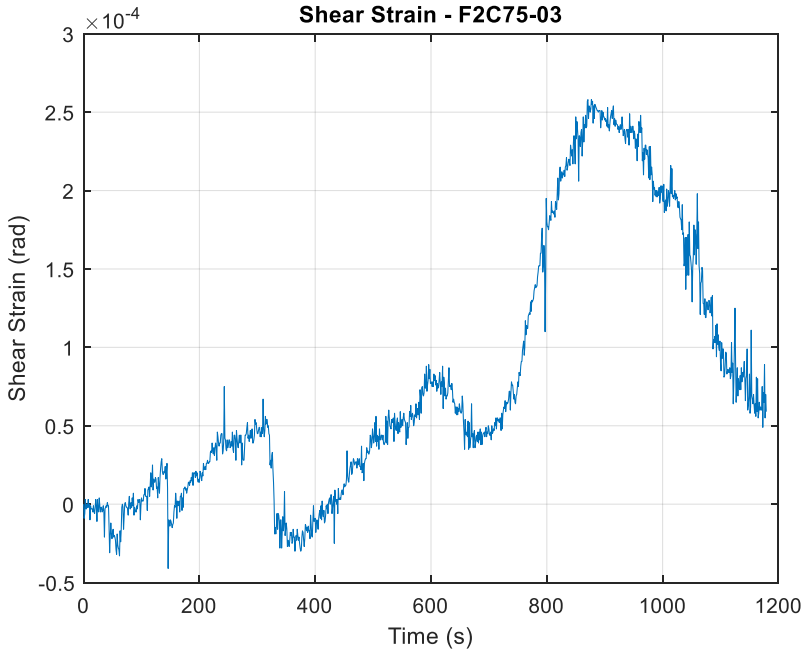
Shear Strain - F2C75-03
$\times 10^{-4}$
Shear Strain (rad)
Time (s)
3
2.5
2
1.5
1
0.5
0
-0.5
0
200
400
600
800
1000
1200

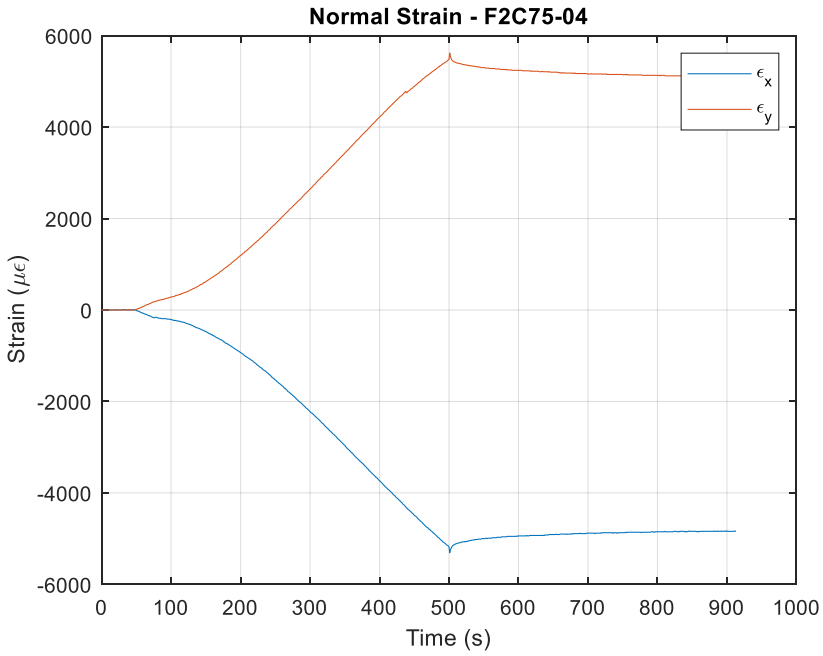
Normal Strain - F2C75-04
Strain ($\mu\epsilon$)
Time (s)
ϵ_x
ϵ_y
6000
4000
2000
0
-2000
-4000
-6000
0
100
200
300
400
500
600
700
800
900
1000

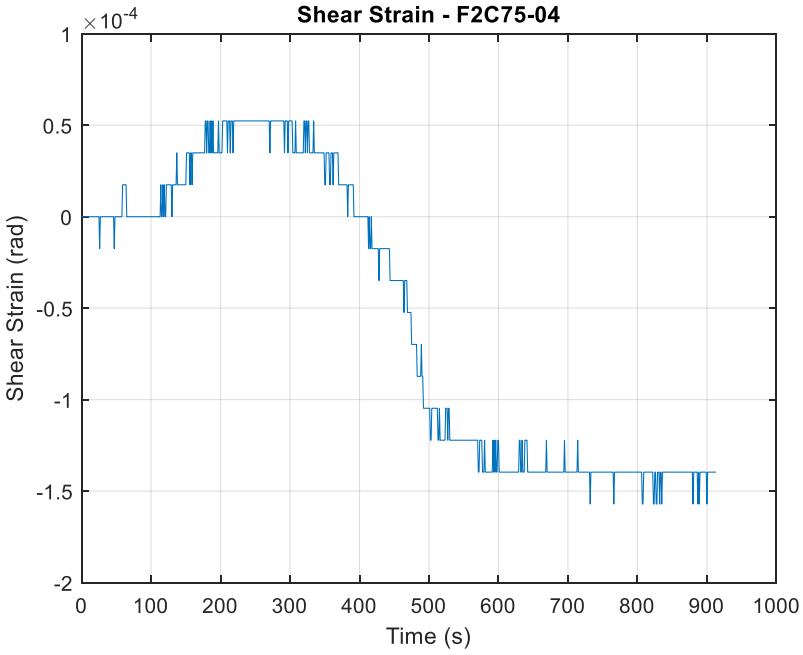
Shear Strain - F2C75-04
$\times 10^{-4}$
Shear Strain (rad)
Time (s)
1
0.5
0
-0.5
-1
-1.5
-2
0
100
200
300
400
500
600
700
800
900
1000

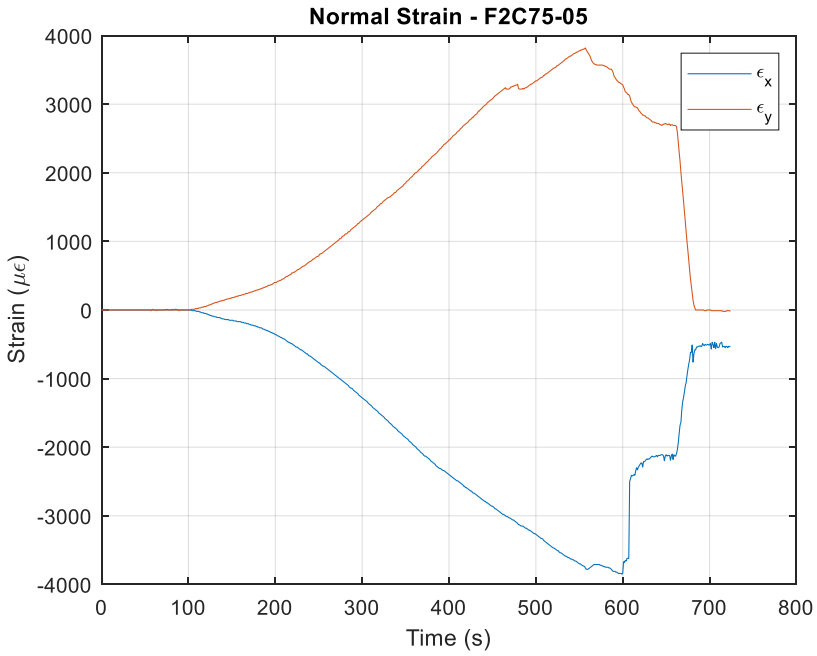
Normal Strain - F2C75-05
Strain ($\mu\epsilon$)
Time (s)
ϵ_x
ϵ_y
4000
3000
2000
1000
0
-1000
-2000
-3000
-4000
0
100
200
300
400
500
600
700
800

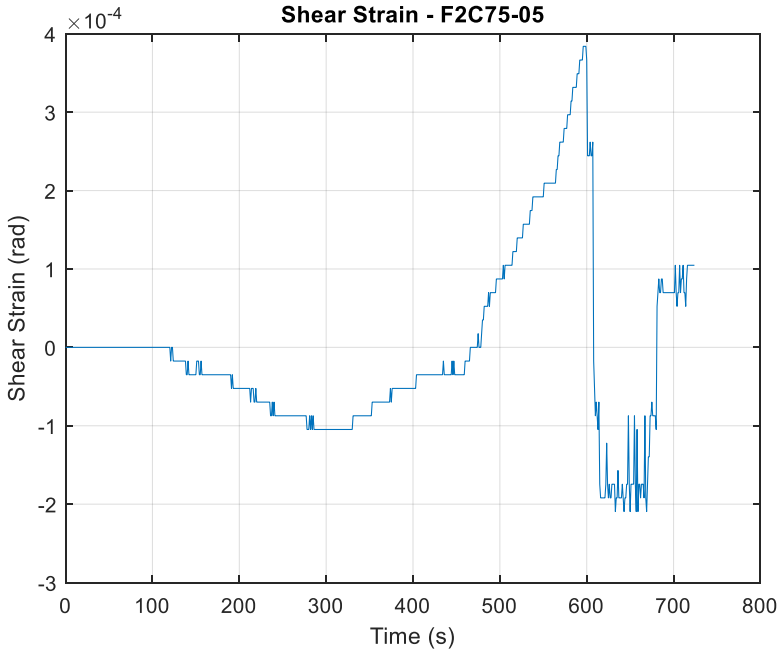
Shear Strain - F2C75-05
$\times 10^{-4}$
Shear Strain (rad)
Time (s)
4
3
2
1
0
-1
-2
-3
0
100
200
300
400
500
600
700
800

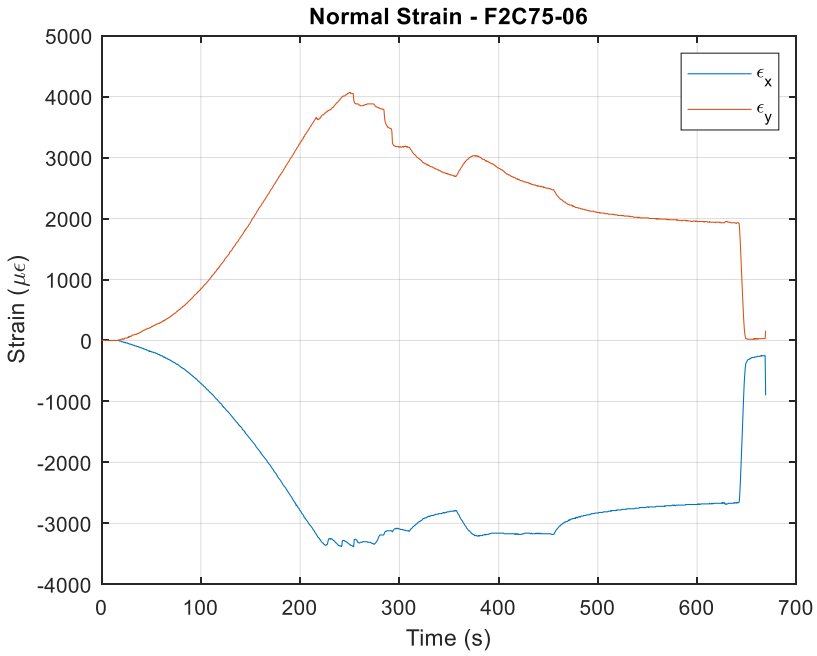
Normal Strain - F2C75-06
Strain ($\mu\epsilon$)
Time (s)
ϵ_x
ϵ_y
5000
4000
3000
2000
1000
0
-1000
-2000
-3000
-4000
0
100
200
300
400
500
600
700

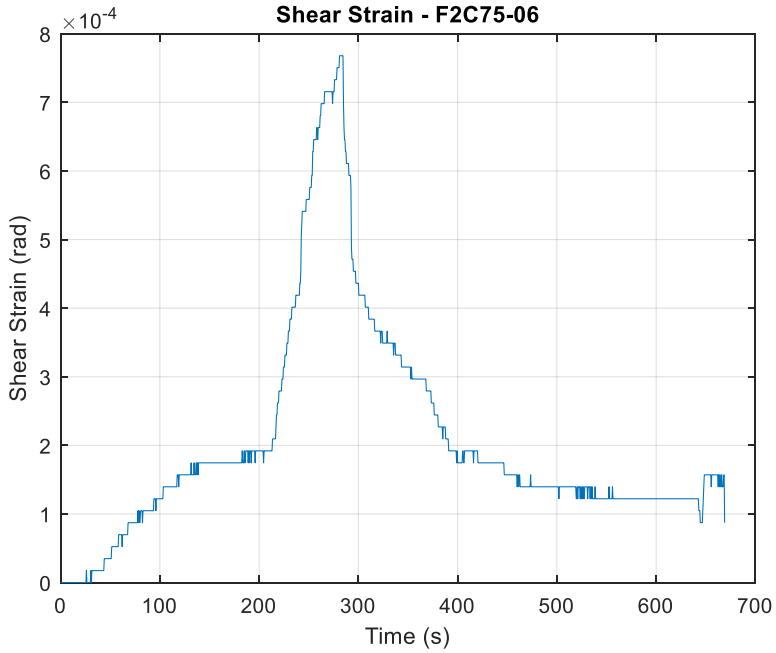
Shear Strain - F2C75-06
$\times 10^{-4}$
Shear Strain (rad)
Time (s)
8
7
6
5
4
3
2
1
0
0
100
200
300
400
500
600
700

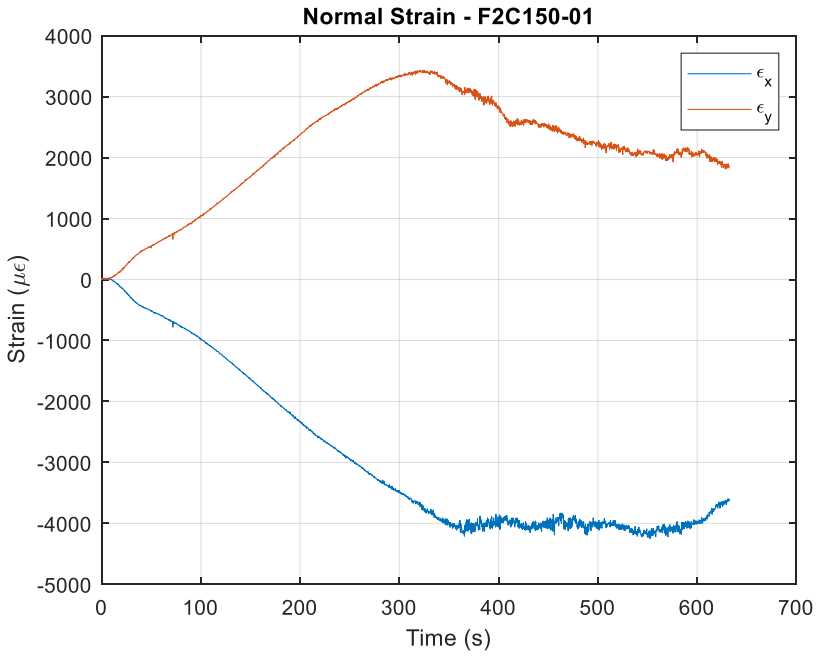
Normal Strain - F2C150-01
Strain ($\mu\epsilon$)
Time (s)
ϵ_x
ϵ_y
4000
3000
2000
1000
0
-1000
-2000
-3000
-4000
-5000
0
100
200
300
400
500
600
700

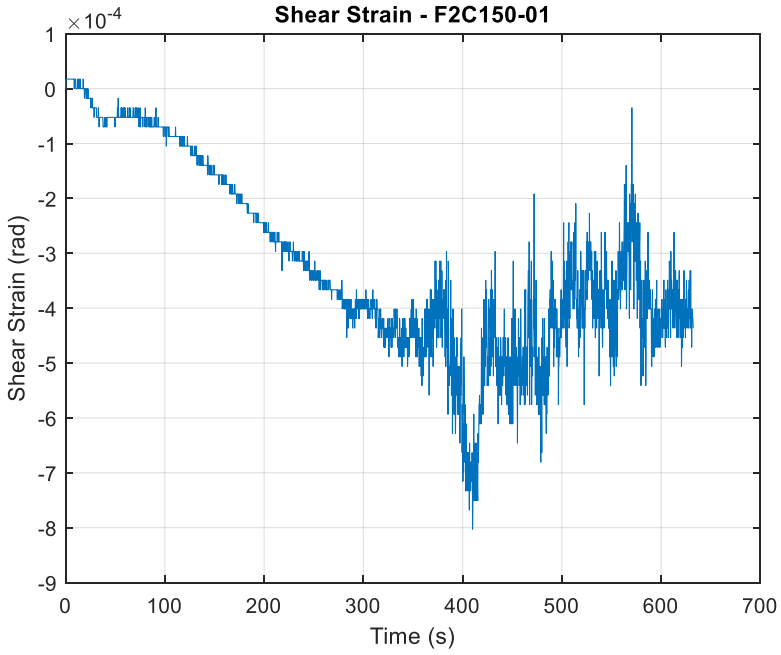
Shear Strain - F2C150-01
$\times 10^{-4}$
Shear Strain (rad)
Time (s)
1
0
-1
-2
-3
-4
-5
-6
-7
-8
-9
0
100
200
300
400
500
600
700

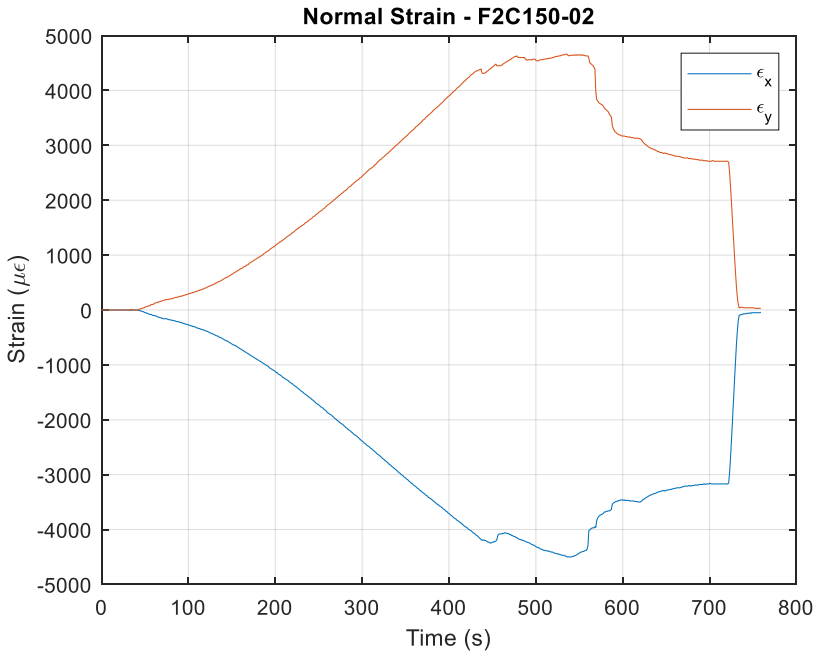
Normal Strain - F2C150-02
Strain ($\mu\epsilon$)
Time (s)
ϵ_x
ϵ_y
5000
4000
3000
2000
1000
0
-1000
-2000
-3000
-4000
-5000
0
100
200
300
400
500
600
700
800

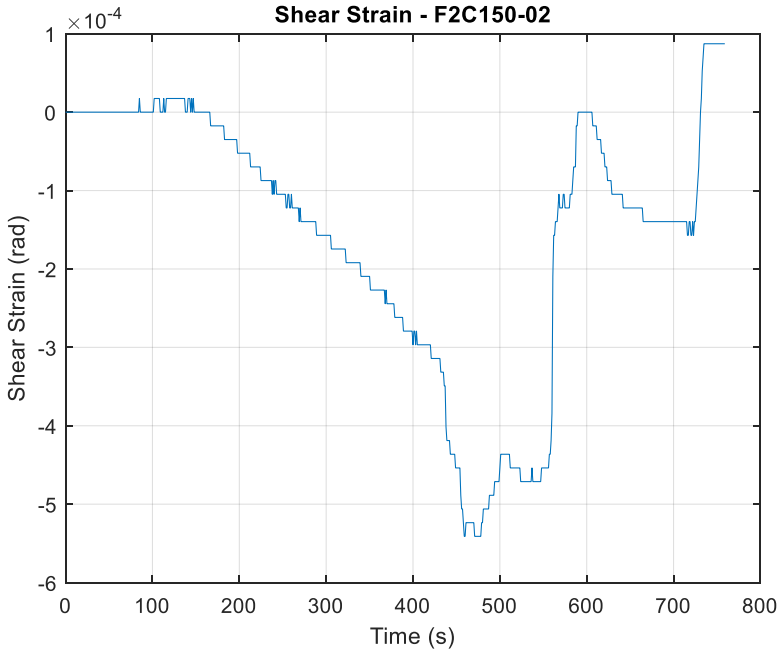
Shear Strain - F2C150-02
$\times 10^{-4}$
Shear Strain (rad)
Time (s)
1
0
-1
-2
-3
-4
-5
-6
0
100
200
300
400
500
600
700
800

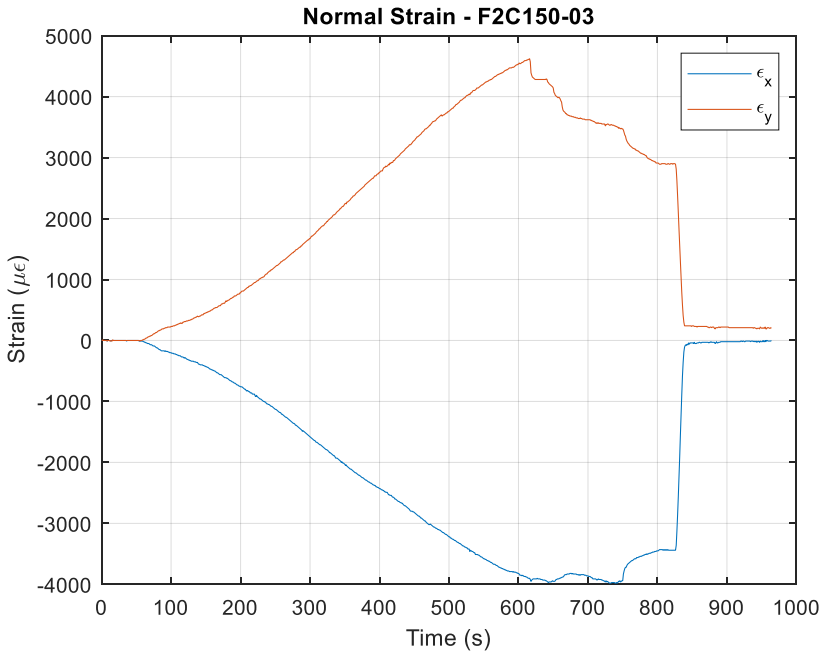
Normal Strain - F2C150-03
Strain ($\mu\epsilon$)
Time (s)
ϵ_x
ϵ_y
5000
4000
3000
2000
1000
0
-1000
-2000
-3000
-4000
0
100
200
300
400
500
600
700
800
900
1000

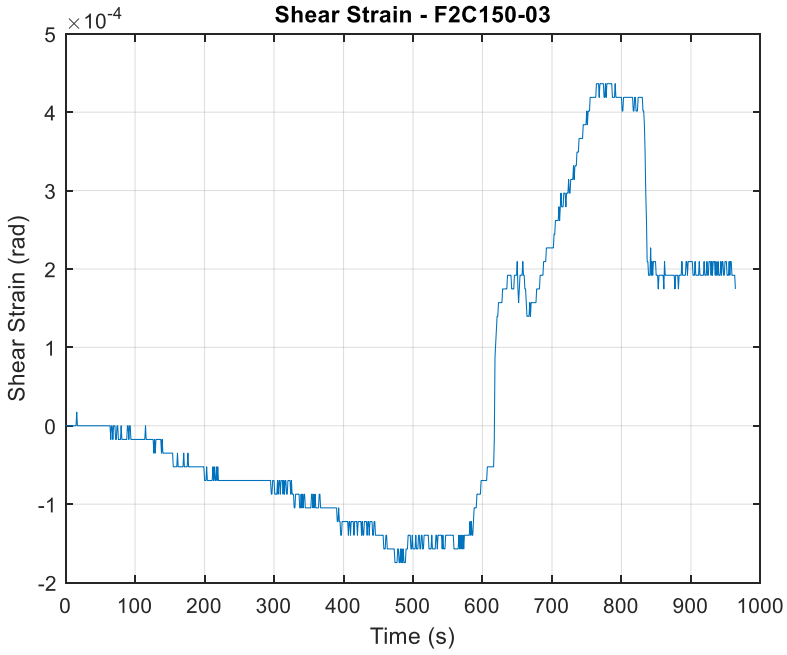
Shear Strain - F2C150-03
$\times 10^{-4}$
Shear Strain (rad)
Time (s)
5
4
3
2
1
0
-1
-2
0
100
200
300
400
500
600
700
800
900
1000

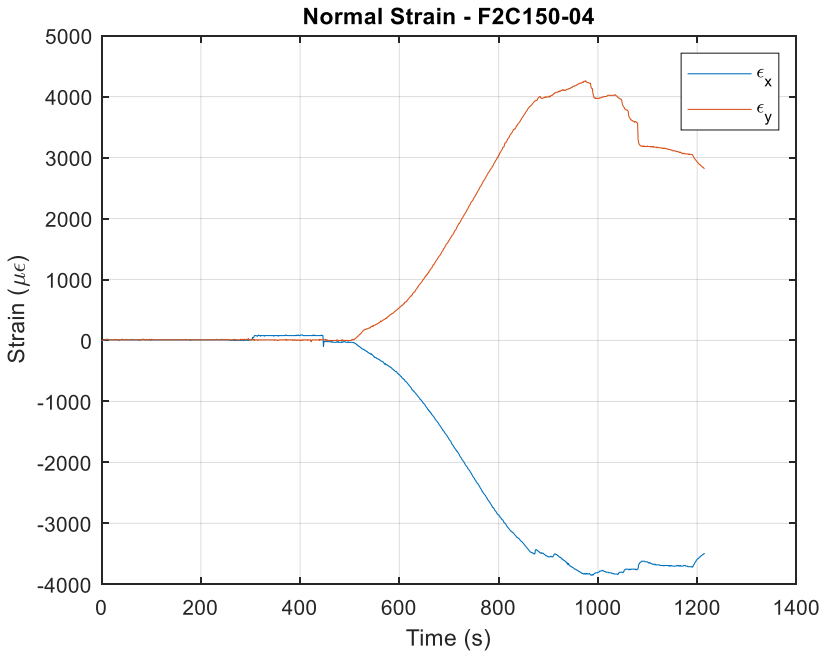
Normal Strain - F2C150-04
Strain ($\mu\epsilon$)
Time (s)
ϵ_x
ϵ_y
5000
4000
3000
2000
1000
0
-1000
-2000
-3000
-4000
0
200
400
600
800
1000
1200
1400

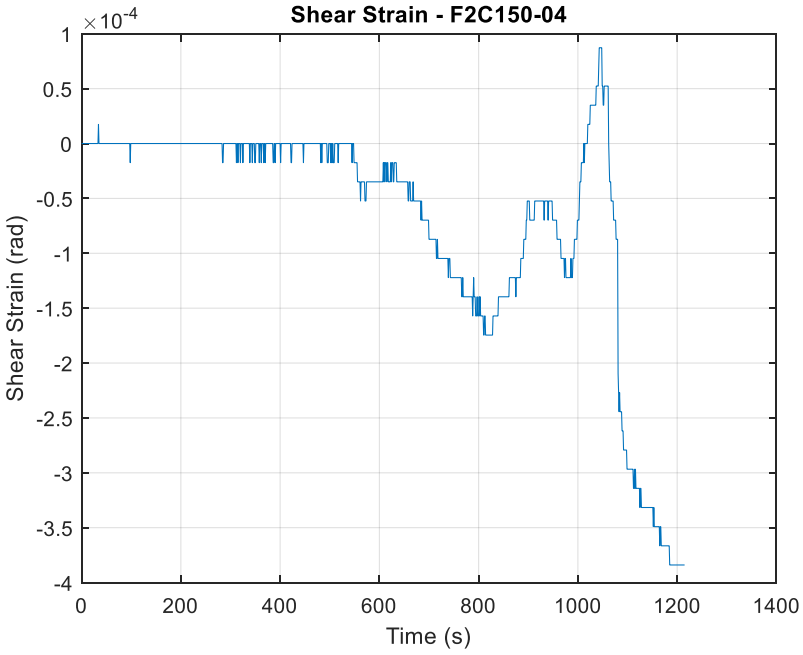
Shear Strain - F2C150-04
$\times 10^{-4}$
Shear Strain (rad)
Time (s)
1
0.5
0
-0.5
-1
-1.5
-2
-2.5
-3
-3.5
-4
0
200
400
600
800
1000
1200
1400

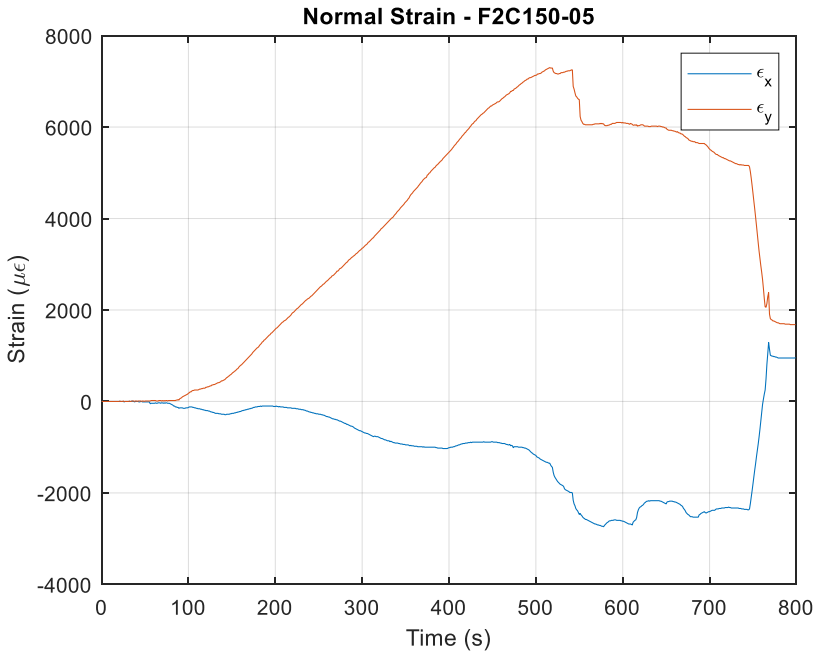
Normal Strain - F2C150-05
8000
6000
4000
2000
0
-2000
-4000
Strain ($\mu\epsilon$)
0
100
200
300
400
500
600
700
800
Time (s)
ϵ_x
ϵ_y

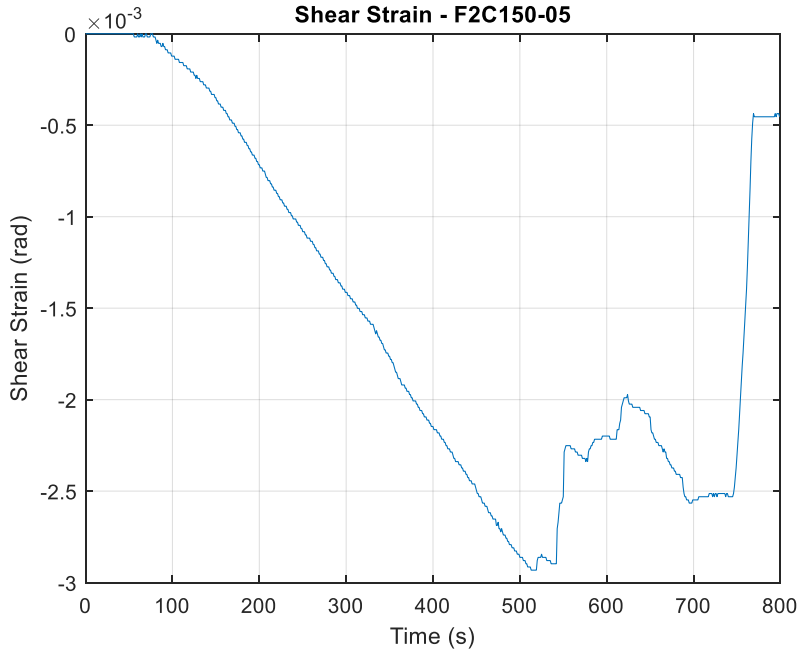
Shear Strain - F2C150-05
$\times 10^{-3}$
0
-0.5
-1
-1.5
-2
-2.5
-3
Shear Strain (rad)
0
100
200
300
400
500
600
700
800
Time (s)

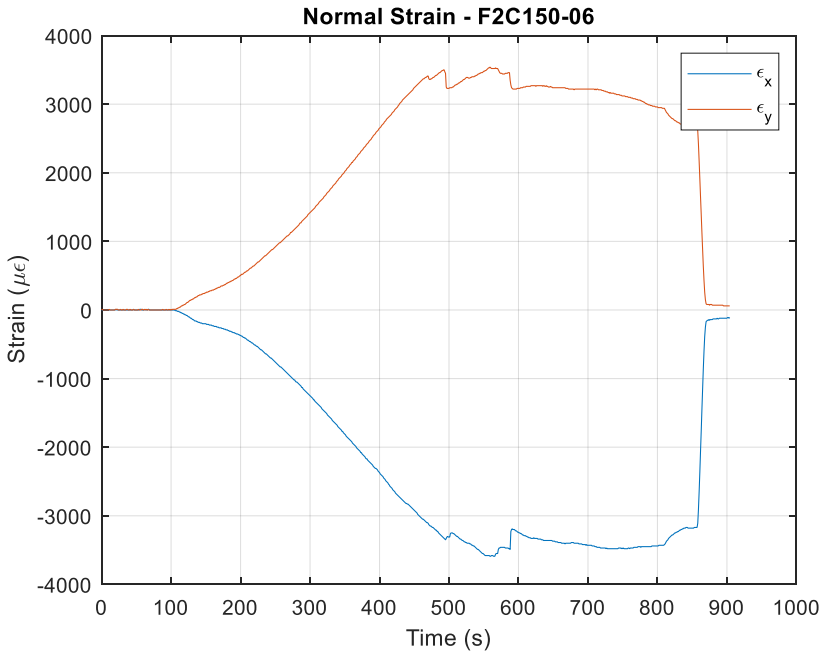
Normal Strain - F2C150-06
Strain ($\mu\epsilon$)
Time (s)
ϵ_x
ϵ_y
4000
3000
2000
1000
0
-1000
-2000
-3000
-4000
0
100
200
300
400
500
600
700
800
900
1000

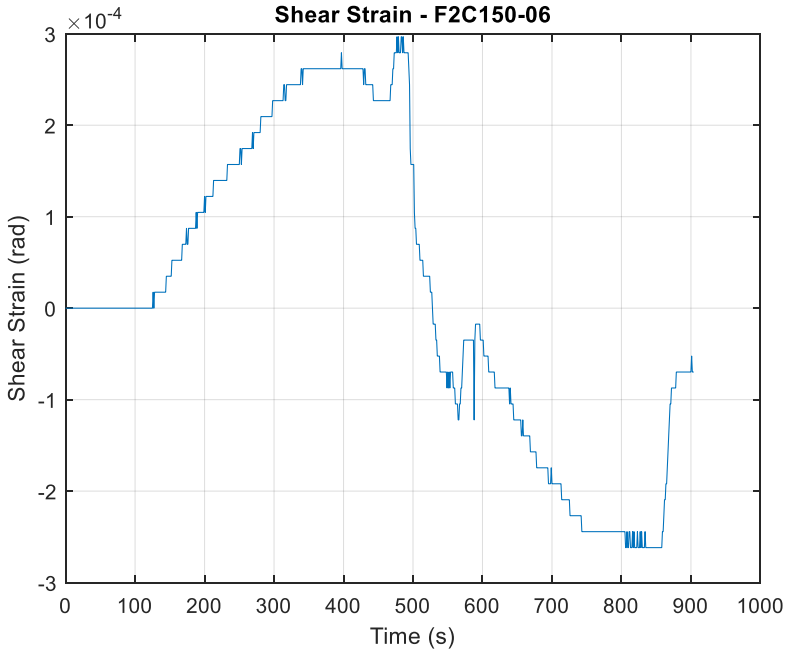
Shear Strain - F2C150-06
$\times 10^{-4}$
Shear Strain (rad)
Time (s)
3
2
1
0
-1
-2
-3
0
100
200
300
400
500
600
700
800
900
1000

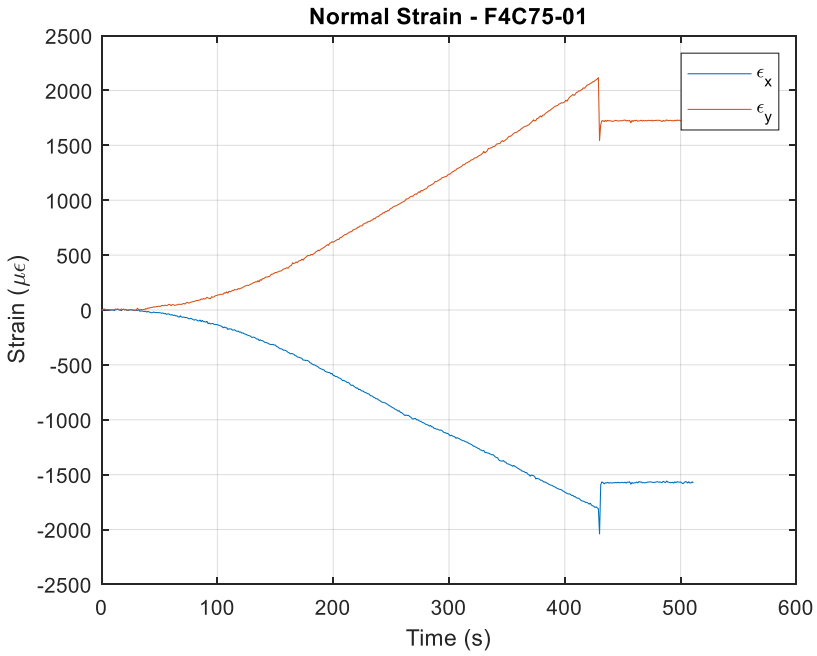
Normal Strain - F4C75-01
Strain ($\mu\epsilon$)
Time (s)
ϵ_x
ϵ_y
2500
2000
1500
1000
500
0
-500
-1000
-1500
-2000
-2500
0
100
200
300
400
500
600

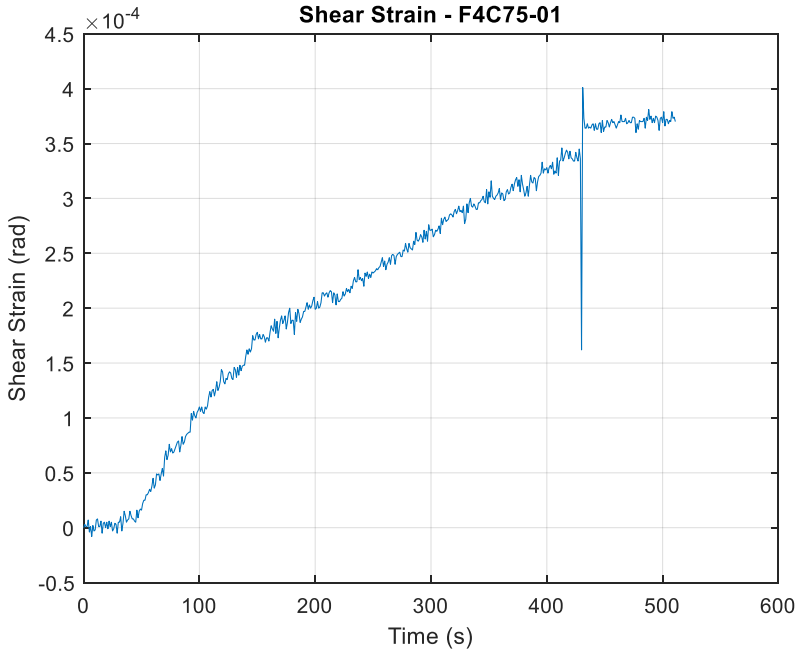
Shear Strain - F4C75-01
$\times 10^{-4}$
Shear Strain (rad)
Time (s)
4.5
4
3.5
3
2.5
2
1.5
1
0.5
0
-0.5
0
100
200
300
400
500
600

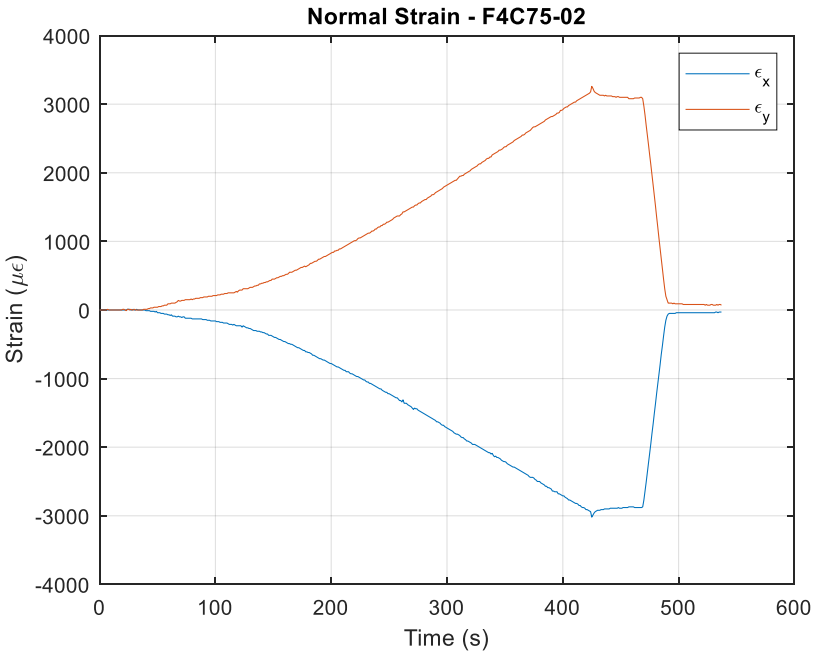
Normal Strain - F4C75-02
Strain ($\mu\epsilon$)
Time (s)
ϵ_x
ϵ_y
4000
3000
2000
1000
0
-1000
-2000
-3000
-4000
0
100
200
300
400
500
600

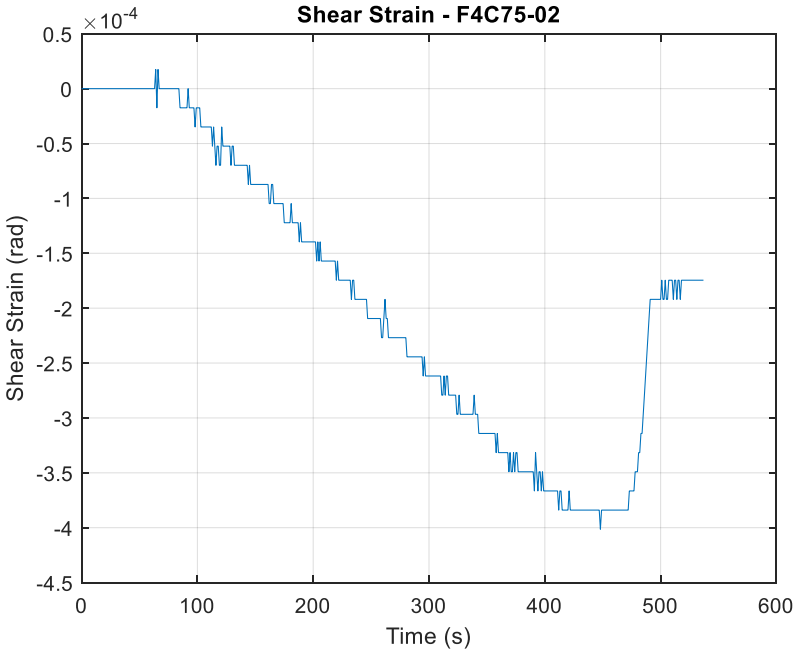
Shear Strain - F4C75-02
$\times 10^{-4}$
Shear Strain (rad)
Time (s)
0.5
0
-0.5
-1
-1.5
-2
-2.5
-3
-3.5
-4
-4.5
0
100
200
300
400
500
600

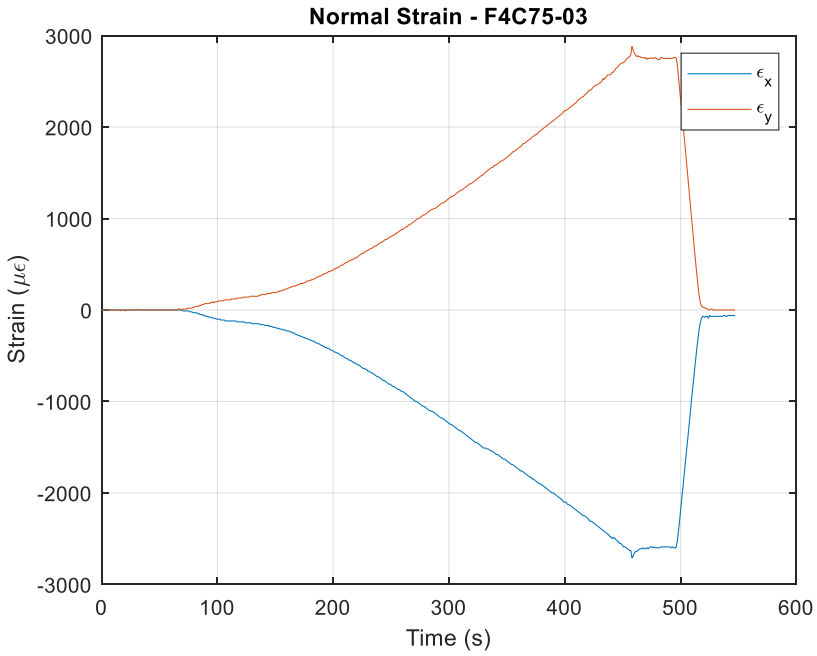
Normal Strain - F4C75-03
Strain ($\mu\epsilon$)
Time (s)
ϵ_x
ϵ_y
3000
2000
1000
0
-1000
-2000
-3000
0
100
200
300
400
500
600

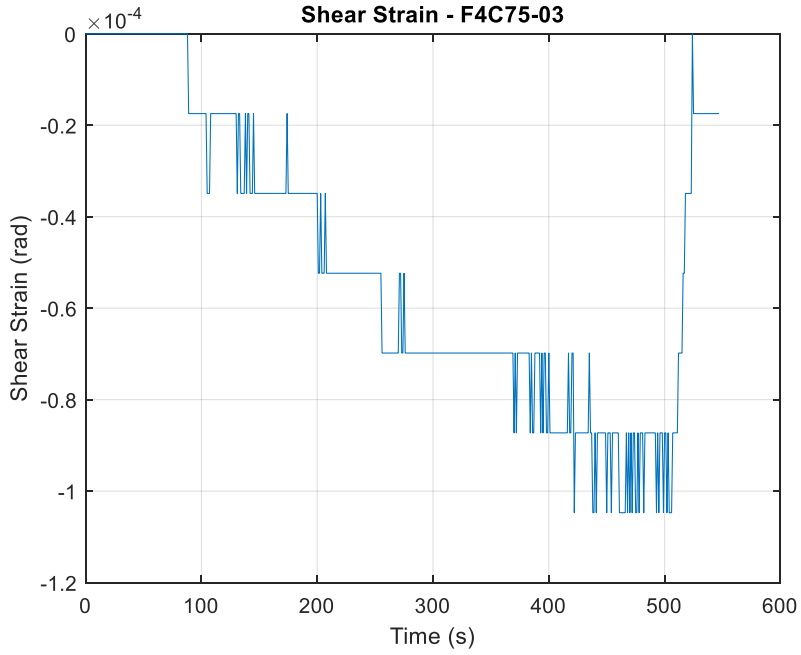
Shear Strain - F4C75-03
$\times 10^{-4}$
Shear Strain (rad)
Time (s)
0
-0.2
-0.4
-0.6
-0.8
-1
-1.2
0
100
200
300
400
500
600

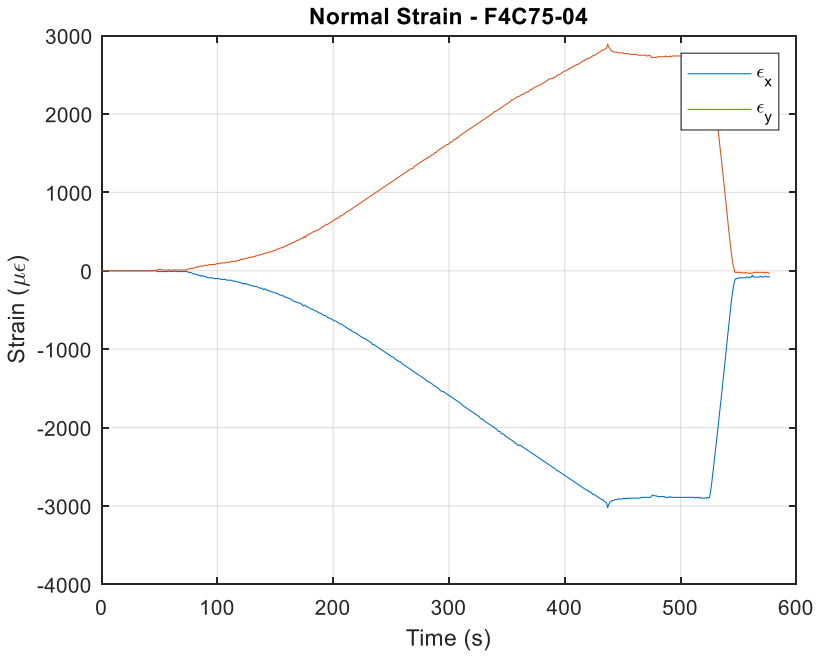
Normal Strain - F4C75-04
Strain ($\mu\epsilon$)
Time (s)
ϵ_x
ϵ_y
3000
2000
1000
0
-1000
-2000
-3000
-4000
0
100
200
300
400
500
600

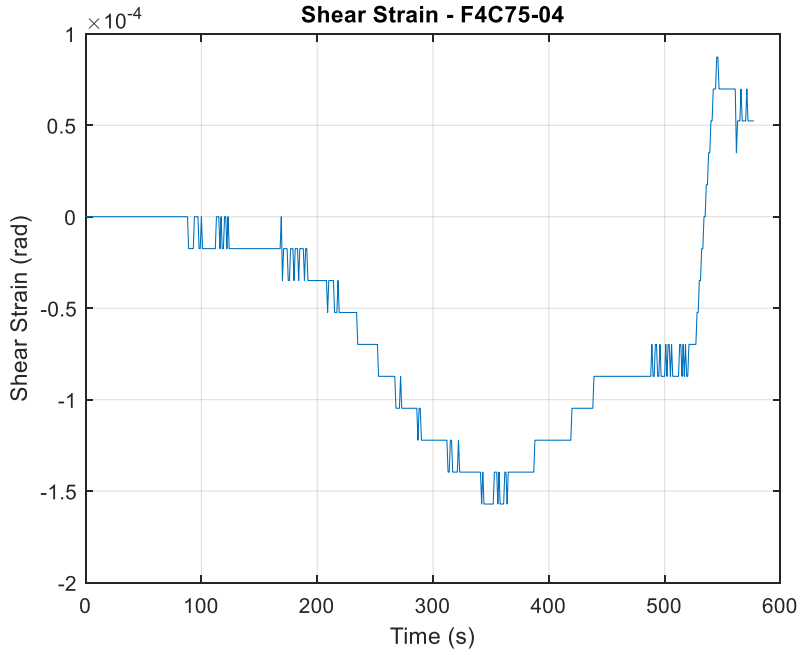
Shear Strain - F4C75-04
$\times 10^{-4}$
Shear Strain (rad)
Time (s)
1
0.5
0
-0.5
-1
-1.5
-2
0
100
200
300
400
500
600

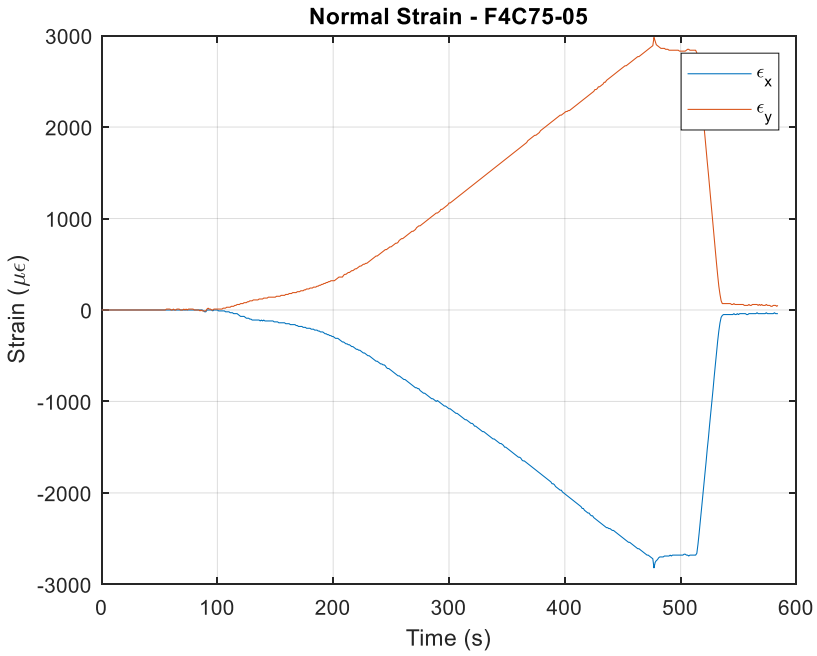
Normal Strain - F4C75-05
Strain ($\mu\epsilon$)
Time (s)
ϵ_x
ϵ_y
3000
2000
1000
0
-1000
-2000
-3000
0
100
200
300
400
500
600

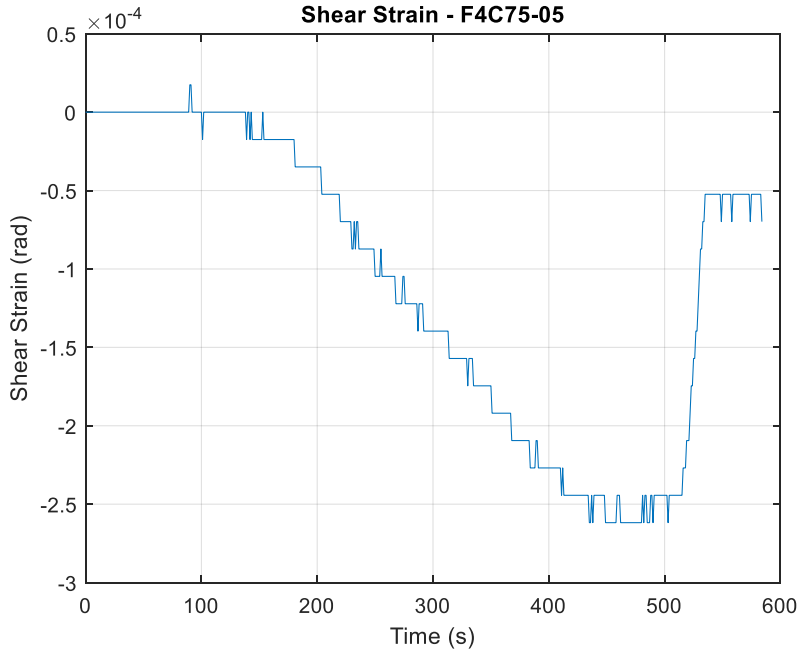
Shear Strain - F4C75-05
$\times 10^{-4}$
Shear Strain (rad)
Time (s)
0.5
0
-0.5
-1
-1.5
-2
-2.5
-3
0
100
200
300
400
500
600

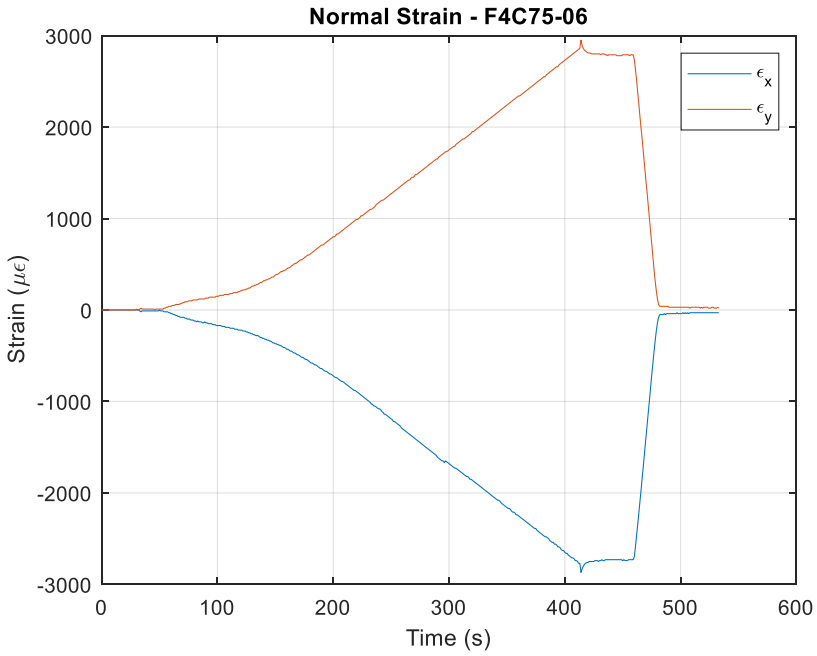
Normal Strain - F4C75-06
Strain ($\mu\epsilon$)
Time (s)
ϵ_x
ϵ_y
3000
2000
1000
0
-1000
-2000
-3000
0
100
200
300
400
500
600

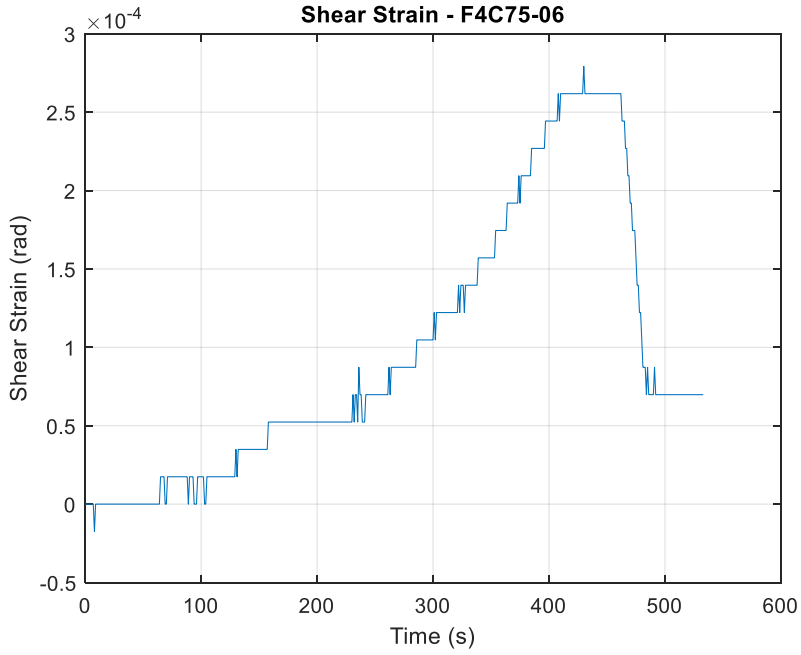
Shear Strain - F4C75-06
$\times 10^{-4}$
Shear Strain (rad)
Time (s)
3
2.5
2
1.5
1
0.5
0
-0.5
0
100
200
300
400
500
600

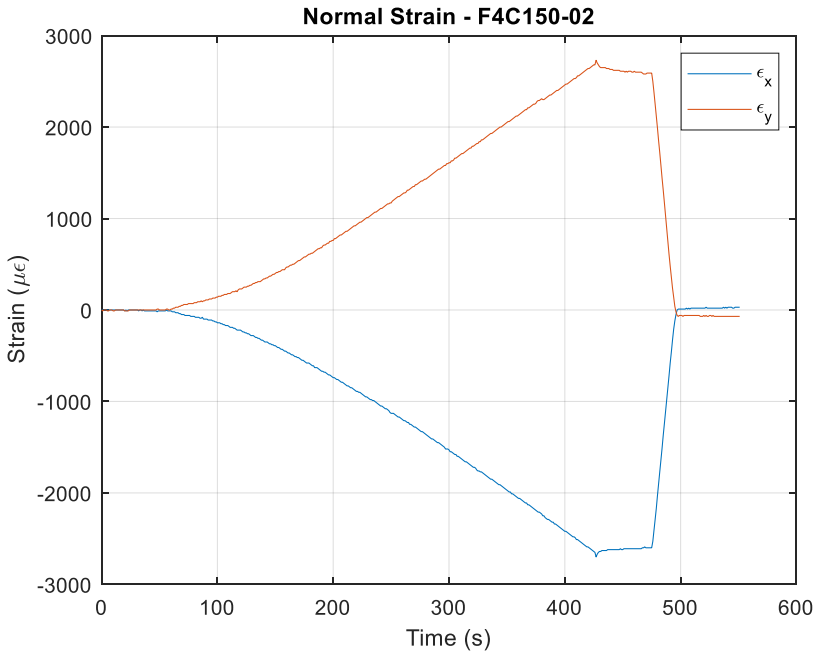
Normal Strain - F4C150-02
Strain ($\mu\epsilon$)
Time (s)
ϵ_x
ϵ_y
3000
2000
1000
0
-1000
-2000
-3000
0
100
200
300
400
500
600

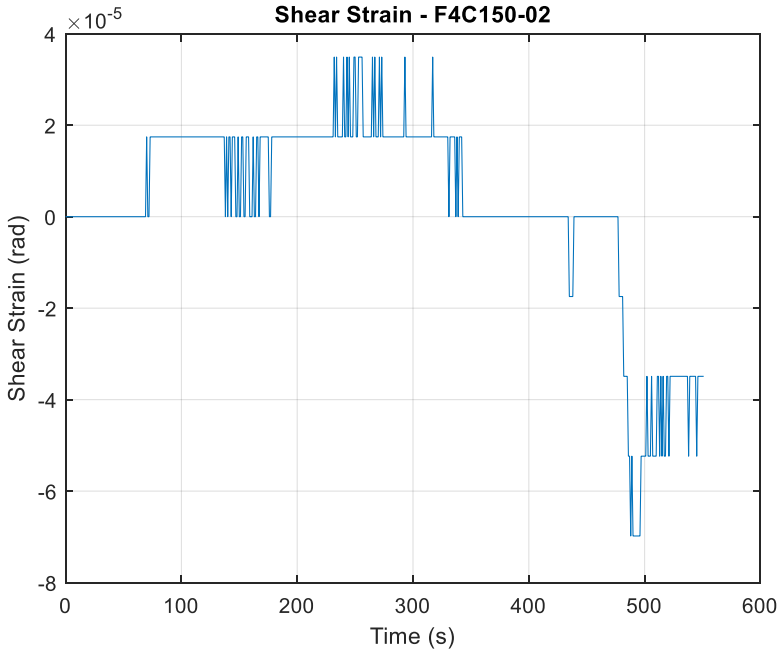
Shear Strain - F4C150-02
$\times 10^{-5}$
Shear Strain (rad)
Time (s)
4
2
0
-2
-4
-6
-8
0
100
200
300
400
500
600

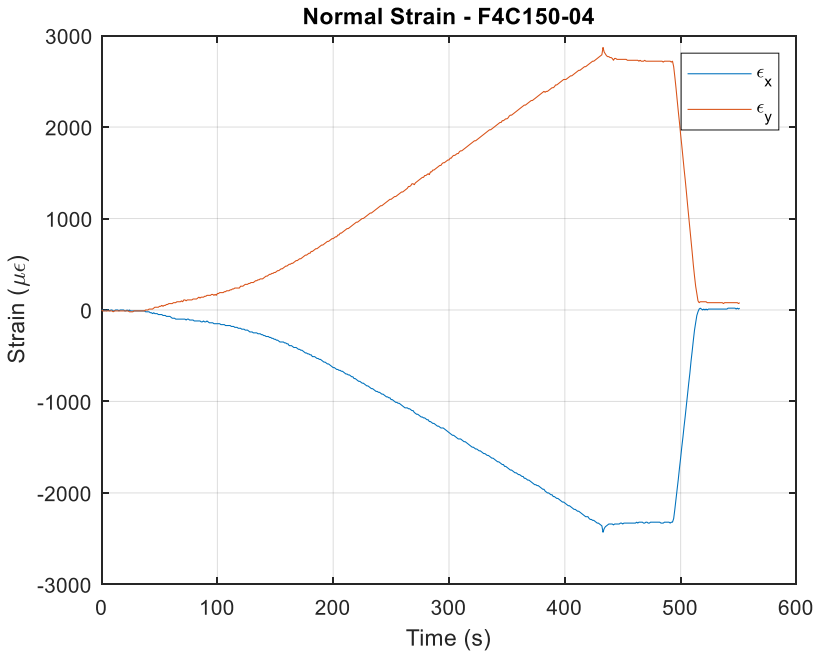
Normal Strain - F4C150-04
Strain ($\mu\epsilon$)
Time (s)
ϵ_x
ϵ_y
3000
2000
1000
0
-1000
-2000
-3000
0
100
200
300
400
500
600

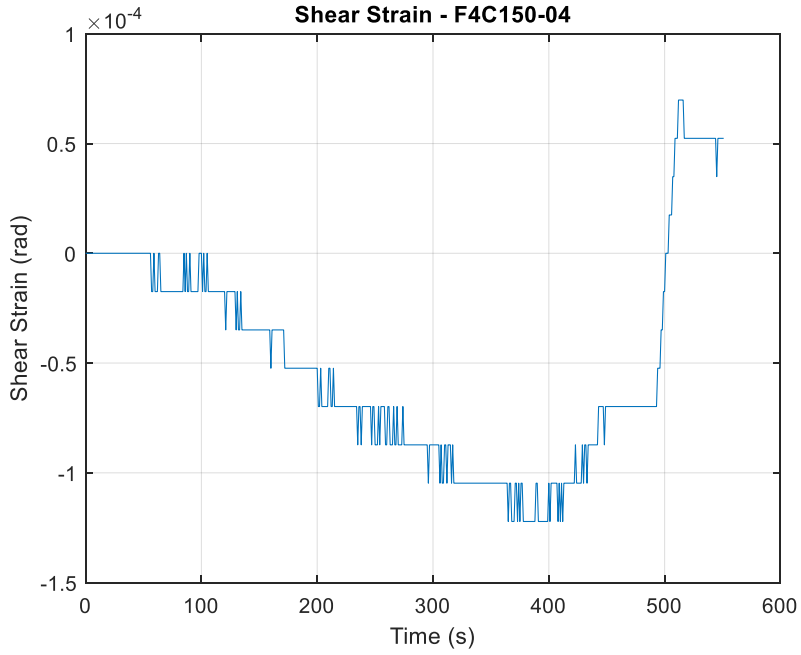
Shear Strain - F4C150-04
$\times 10^{-4}$
Shear Strain (rad)
Time (s)
1
0.5
0
-0.5
-1
-1.5
0
100
200
300
400
500
600

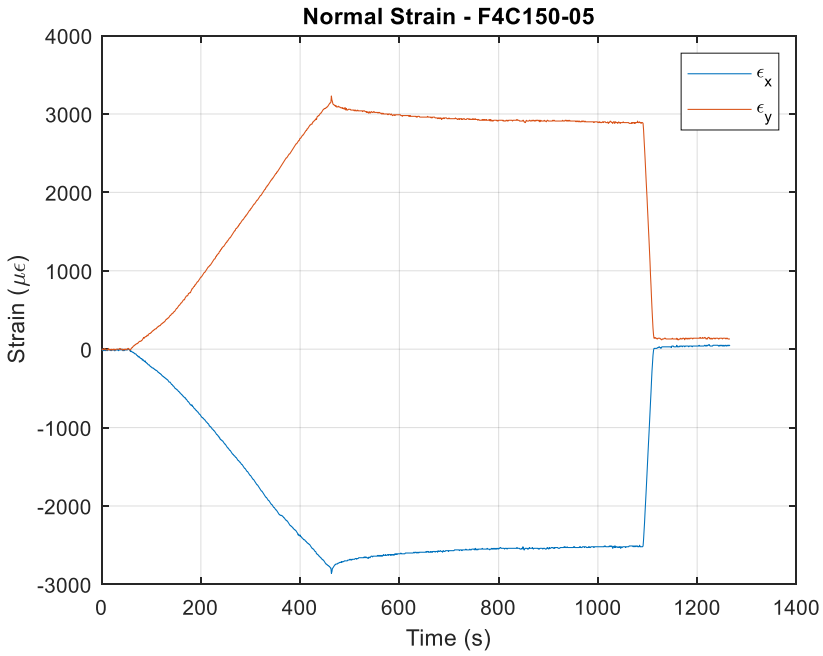
Normal Strain - F4C150-05
Strain ($\mu\epsilon$)
Time (s)
ϵ_x
ϵ_y
4000
3000
2000
1000
0
-1000
-2000
-3000
0
200
400
600
800
1000
1200
1400

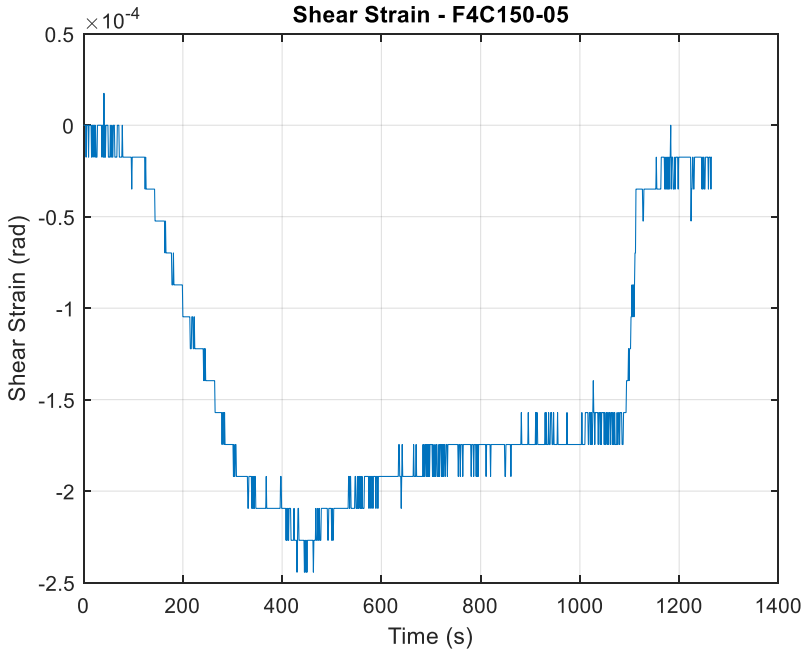
Shear Strain - F4C150-05
$\times 10^{-4}$
Shear Strain (rad)
Time (s)
0.5
0
-0.5
-1
-1.5
-2
-2.5
0
200
400
600
800
1000
1200
1400

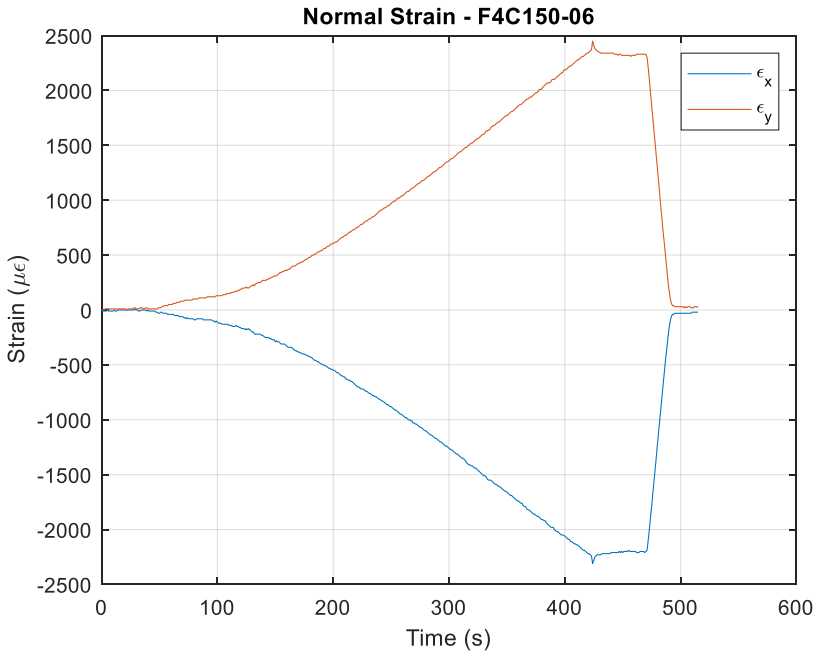
Normal Strain - F4C150-06
Strain ($\mu\epsilon$)
Time (s)
ϵ_x
ϵ_y
2500
2000
1500
1000
500
0
-500
-1000
-1500
-2000
-2500
0
100
200
300
400
500
600

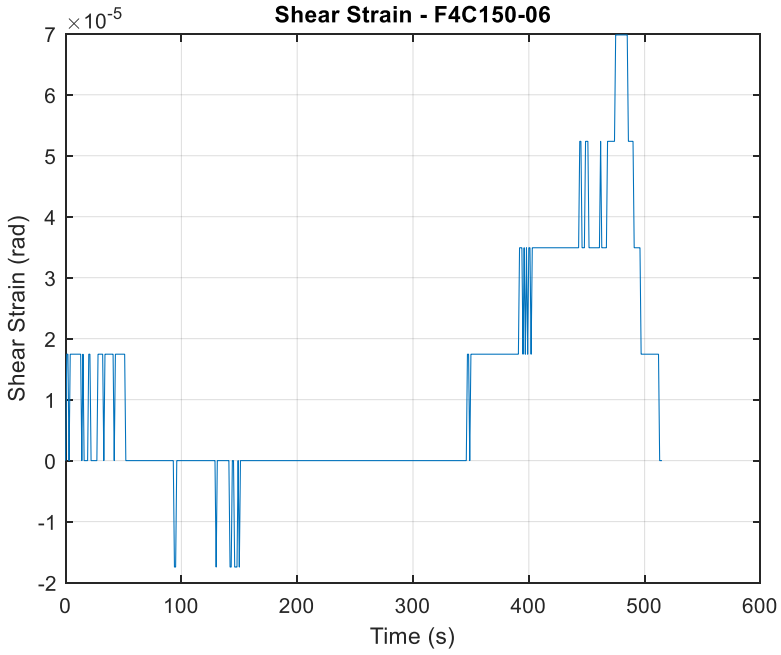
Shear Strain - F4C150-06
$\times 10^{-5}$
Shear Strain (rad)
Time (s)
7
6
5
4
3
2
1
0
-1
-2
0
100
200
300
400
500
600

Appendix B: Description of Detailed Method for Flexural Analysis and Comparison with Simplified Method

B.1 Detailed Method

The detailed method for flexural analysis must consider the effects of staged construction, wherein strains due to the self-weight of the girder and wet concrete are permanently locked into the girder alone. To account for this, this locked-in strain is calculated as:

$$\varepsilon_{DC} = \frac{M_{DC}}{E_{bf} S_{NC}} \tag{B.1-1}$$

where:

$M_{DC} =$	factored moment due to non-composite dead-load (kip-in.)
$E_{bf} =$	elastic modulus of the bottom flange (ksi)
$S_{NC} =$	non-composite section modulus (in.^{3})

For each component for which tensile or compressive failure due to flexure can occur (bottom flange, web just above the web-bottom flange fillet, and deck), determine ultimate strain, ε_f. For tensile rupture of the bottom flange the ultimate strain available for to carry loads acting on the composite section is:

$$\varepsilon_{1t}^{C} = \varepsilon_{1t} - \varepsilon_{DC} \tag{B.1-2}$$

For crushing of the deck, the maximum usable concrete compressive strain $\varepsilon_{cu} = 0.003$.

Select a trial neutral axis depth, c, and use it to determine the section's curvature at failure, κ. For tensile rupture of the bottom flange:

$$\kappa = \frac{\varepsilon_f}{D - c} \tag{B.1-3a}$$

for crushing of the deck:

$$\kappa = \frac{\varepsilon_f}{c} \tag{B.1-3b}$$

where:

$D =$ total depth of the composite section (in.)

$t_{bf} =$ thickness of the bottom flange (in.)

Using plane section assumptions, determine the strain at every height y_i above the bottom of the section. The section can be analyzed continuously, but it is more convenient to discretize the section into layers within which strain and stress are constant, where layers are denoted here by the subscript i.

$$\varepsilon_i = -\kappa(D - c - y_i) \tag{B.1-4}$$

The corresponding stress is σ_i. For y_i falling within the bottom flange:

$$\sigma_i = \frac{\varepsilon_i}{E_{bf}} \tag{B.1-5a}$$

for y_i falling within the web:

$$\sigma_i = \frac{\varepsilon_i}{E_w} \tag{B.1-5b}$$

for y_i falling within the top flange:

$$\sigma_i = \frac{\varepsilon_i}{E_{tf}} \tag{B.1-5c}$$

For y_i falling within the deck:

$$\sigma_i = \begin{cases} f'_c * \left(\frac{2\varepsilon_i}{\varepsilon_c} - \left(\frac{\varepsilon_i}{\varepsilon_c}\right)^2\right), & \varepsilon_i \le \varepsilon_c \\ f'_c * \left(1 - 0.15 * \frac{\varepsilon_i - \varepsilon_c}{\varepsilon_u - \varepsilon_c}\right), & \varepsilon_c < \varepsilon_i \le \varepsilon_u \\ 0.95\varepsilon_u, & \varepsilon_i > \varepsilon_u \end{cases} \tag{B.1-5d}$$

where:

$E_{bf} =$ effective bending modulus of the bottom flange (ksi)

$E_w =$ effective bending modulus of the web (ksi)

$f'_c =$	specified 28-day compressive strength of the concrete making up the deck (ksi)
$\varepsilon_c = 1.8\frac{f'_c}{E_c}$	maximum strain in concrete prior to the onset of significant softening
$E_c = 1820\sqrt{f'_c}$	elastic modulus of concrete (ksi)
$\varepsilon_u = 0.003$	crushing strain of concrete

If analyzing the section continuously, find the residual force imbalance R by integrating stresses through the section height:

$$R = \int_0^D \sigma_i dA \tag{B.1-6a}$$

or if analyzing the section as discrete layers, by summing the force contribution from each layer through the section height:

$$R = \sum_{i=1}^{n} \sigma_i b_i \delta y \tag{B.1-6b}$$

where:

$dA =$	differential area over which the infinitesimal stress, σ_i acts (in.^{2})
$n =$	number layers into which the section is discretized
$b_i =$	width of the current layer (in.)
δy	thickness of each layer (in.)

Iteratively update the estimate of c until the residual force imbalance is eliminated, ensuring internal force equilibrium.

If analyzing the section continuously, integrate the stresses and their moment arms through the section height to find the section's moment resistance for the given failure mode

$$M_r^C = \phi M_n^C = \phi \int_0^D \sigma_i y_i dA \tag{B.1-7a}$$

or if analyzing the section discretely, sum the force contribution from each layer multiplied by its distance from the section bottom y_i:

$$M_r^C = \phi M_n^C = \phi \sum_{i=1}^{n} \sigma_i b_i y_i \delta y \qquad \text{(B.1-7b)}$$

The nominal moment capacity available to carry factored loads acting on the composite section, ϕM_n^C, will correspond to the moment causing either tensile rupture of the bottom flange at a strain of ε_{1t}^C or crushing of the concrete deck at a compressive strain of $\varepsilon_{cu} = 0.003$, whichever occurs first.

B.2 Flexural Design Examples with Comparison to Simplified Method

B.2.1 Example 1

The CT girder cross-section shown below was designed for bottom flange tension control and was analyzed using the detailed method given above, and the simplified method detailed in Section 2.9.6. Factored non-composite dead-load moment at midspan of the 75 foot span $\gamma_{DC}M_{DC} = 783\ kip - ft$. Factored moment applied to the composite section, $\gamma_{LL}M_{LL+IM} + \gamma_{DW}M_{DW} = 2690\ ft - kip$.

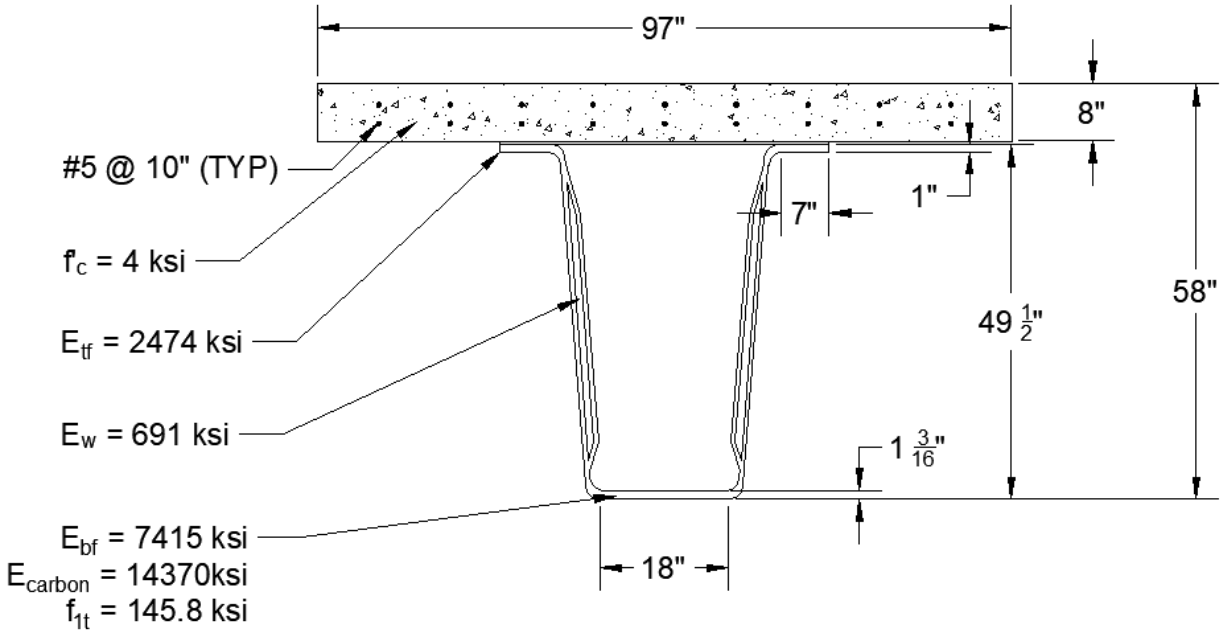

B.2.1.1 Detailed Method

Using the detailed method as implemented with layered moment-curvature analysis as described in A.1, the section has a factored, available composite moment resistance ϕM_n^C =4500 kip-ft. Details are not provided here, as software specifically implementing moment-curvature analysis was developed to generate this moment capacity. For details and examples on the implementation of moment-curvature analysis, see, for instance, Davids et al. (2000), Davids (2001), Lou & Xiang (2006), Schanck and Davids (2020, 2021), Kwak & Kim (2002), Kara & Ashour (2013), among many others.

B.2.1.2 Simplified Method

As the section was designed for tension control using the detailed method, so concrete crushing should not control when using the simplified method. This is verified by examining the strain at the top of the concrete at tensile rupture as shown below.

$$\varepsilon_{1t}^{C} = \frac{f_{1t}{}^{*} C_E}{E_1} - \frac{M_{DC}}{E_{bf} S_{NC}} = \frac{145.8\ ksi * 0.85}{14370\ ksi} - \frac{783\ kip - ft * 12\ \frac{in}{ft}}{7415\ ksi * 922\ in^3} = 7.25 * 10^{-3}$$

$$E_c = 1820\sqrt{f'_c} = 1820\sqrt{4\ ksi} = 3640\ ksi$$

$$\varepsilon_0 = 1.71\frac{f'_c}{E_c} = 1.71 * \frac{4\ ksi}{3640\ ksi} = 0.00188$$

Begin with a guess for neutral axis depth – say 8 in. from the top of the section (at the bottom of the deck).

$$c = 8\ in$$

Calculate the strain at the top and bottom of the concrete slab

$$\varepsilon_{ct} = \frac{\varepsilon_{1t}^{C} * c}{D - c} = \frac{7.25 * 10^{-3} * 8\ in}{58in - 8\ in} = 0.0012$$

$$\varepsilon_{cb} = \frac{\varepsilon_{1t}^{C} * (c - t_c)}{D - c} = \frac{5.09 * 10^{-3} * (8\ in - 8i\ n)}{58\ in - 8\ in} = 0$$

and use these to determine the stress at the top and bottom of the slab

$$f_{ct} = \frac{1.8 * f'_c * {}^{\varepsilon_{ct}}/_{\varepsilon_0}}{1 + \left({}^{\varepsilon_{ct}}/_{\varepsilon_0}\right)^2} = \frac{1.8 * 4\ ksi * {}^{0.0012}/_{0.00188}}{1 + \left({}^{0.0012}/_{0.00188}\right)^2} = 3.22\ ksi$$

$$f_{cb} = \frac{1.8 * f'_c * {}^{\varepsilon_{cb}}/_{\varepsilon_0}}{1 + \left({}^{\varepsilon_{cb}}/_{\varepsilon_0}\right)^2} = \frac{1.8 * 4ksi * {}^{0}/_{0.00188}}{1 + \left({}^{0}/_{0.00188}\right)^2} = 0\ ksi$$

The current estimate of the neutral axis falls at the interface between the CT girder and the slab, so the compressive force is calculated as

$$C = \frac{1}{2} f_{ct} c b_c = \frac{1}{2}(3.22\ ksi)(8\ in)(97\ in) = 1248\ kip$$

The tensile force in the bottom flange is calculated as

$$T = \varepsilon_{1t}^{C} E_{bf} A_{bf} = 5.09 * 10^{-3} * 7417\ ksi * 21.096\ in^2 = 1134\ kip$$

The compressive force exceeds the tensile force. Therefore, the initial guess for neural axis depth is too low. Iterate with a lower neutral axis – say:

$$c = 6\ in$$

Following the same procedure:

$$\varepsilon_{ct} = \frac{\varepsilon_{1t}^{C} * c}{D - c} = \frac{5.09 * 10^{-3} * 9\ in}{58\ in - 9i\ n} = 0.00084$$

$$\varepsilon_{cb} = \frac{\varepsilon_{1t}^{C} * (c - t_c)}{D - c} = \frac{5.09 * 10^{-3} * (9\ in - 8\ in)}{58\ in - 9\ in} = -2.79 * 10^{-4}$$

$$f_{ct} = \frac{1.8 * f'_c * {}^{\varepsilon_{ct}}/_{\varepsilon_0}}{1 + \left({}^{\varepsilon_{ct}}/_{\varepsilon_0}\right)^2} = \frac{1.8 * 4\ ksi * {}^{0.00070}/_{0.00188}}{1 + \left({}^{0.00070}/_{0.00188}\right)^2} = 2.67\ ksi$$

$$f_{cb} = 0ksi$$

(concrete is assumed to carry no tension)

The neutral axis falls within the slab. Therefore,

$$C = \frac{1}{2} f_{ct} c b_c = \frac{1}{2}(2.05\ ksi)(6\ in)(97\ in) = 778kip$$

The tensile force now exceeds the compressive force. Continue iterating by bisection:

Iteration	c (in.)	ε_{ct}	ε_{cb}	f_{ct} (ksi)	f_{cb} (ksi)	C (kip)	$T - C$ (kip)
1	8	0.0012	0	3.21	0	1248	-114
2	6	0.00084	-0.00028	2.67	0	778	356
3	7	0.0010	-0.00014	2.98	0	1011	123
4	7.5	0.0011	-0.00072	3.11	0	1130	4.61

For a neutral axis depth of 7.5 in, the difference between tensile and compressive forces is acceptably small. Therefore, internal force equilibrium is achieved. Because the neutral axis depth is below the bottom of the slab, the moment capacity can now be calculated as:

$$M_2 = \varepsilon_{1t}^{C} E_{bf} A_{bf} \left(D - \frac{t_{bf}}{2} - \frac{c}{3}\right)$$

$$= 7.25 * 10^{-3} * 7415\ ksi * 21.096 in^2 * \left(58\ in - \frac{1.1875i\ n}{2} - \frac{7.5\ in}{3}\right)$$

$$= 62270\ kip - in = 5190\ kip - ft$$

Checking for compression control,

$$0.85f'_c b_c \beta_1 c^2 + 0.003A_{bf}E_{bf}c - 0.003A_{bf}E_{bf}\left(D - \frac{t_{bf}}{2}\right) = 0$$

Solving,

$$c = 9\ in$$

$$\varepsilon_{bf} = 0.003 * \frac{D - c - {}^{t_{bf}}/_2}{c}$$

$$= 0.003 * \frac{58\ in - 9\ in - {}^{1.1875\ in}/_2}{9\ in} = 0.0161 > \varepsilon_{1t}^C$$

The section cannot be compression controlled as concrete cannot reach crushing strain before FRP rupture.

$$\phi M_n^C = 0.75 * 5190\ kip - ft = 3890\ kip - ft$$

This example demonstrates that the simplified method is straightforward and easy to implement by spreadsheet calculation and that both methods lead to adequate designs. However, implementation of the detailed method results in a 16% increase in design moment resistance for this section.

B.2.2 Example 2

The CT girder cross-section shown below was designed for bottom flange tension control and was analyzed using the detailed method given above, and the simplified method detailed in Section 2.9.6. Factored non-composite dead-load moment at midspan of the 38 foot span $\gamma_{DC}M_{DC} = 160\ kip - ft$. Factored moment applied to the composite section, $\gamma_{LL}M_{LL+IM} + \gamma_{DW}M_{DW} = 950\ kip - ft$.

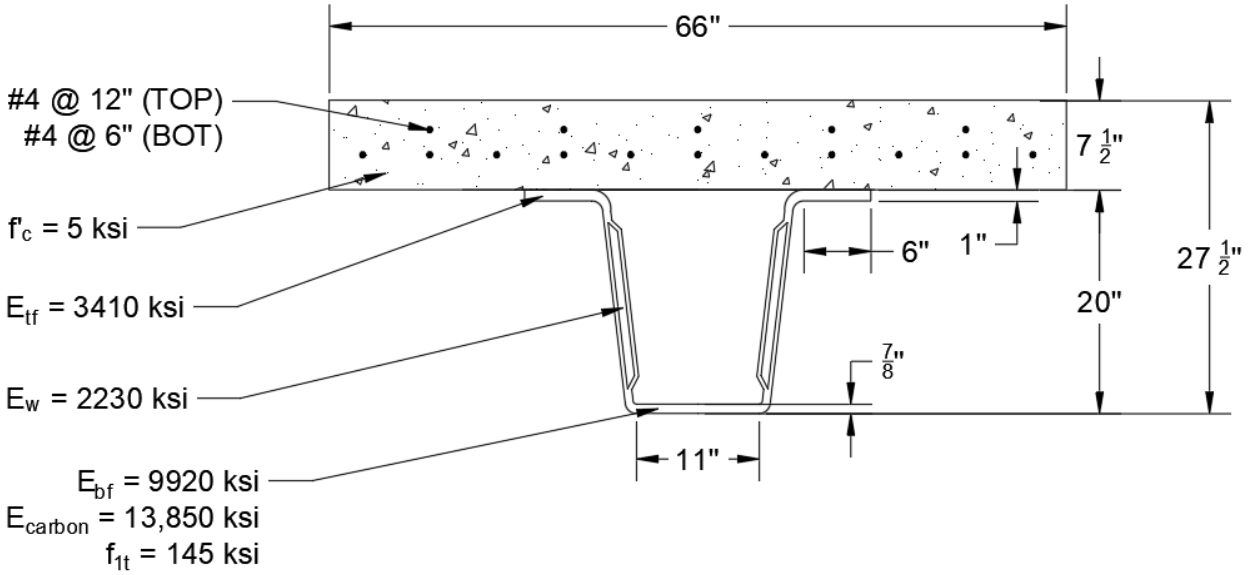

B.2.2.1 Detailed Method

Using the detailed method, the section has a factored, available composite moment resistance ϕM_{nf}^{C} =1390 kip-ft

B.2.2.2 Simplified Method

As the section was designed for tension control using the detailed method, concrete crushing will likely not control. This is verified by examining the strain at the top of the concrete at tensile rupture as shown below.

$$\varepsilon_{1t}^{C} = \frac{f_{1t}{}^{*}C_E}{E_1} - \frac{M_{DC}}{E_{bf}S_{NC}} = \frac{145\ ksi * 0.85}{13950\ ksi} - \frac{160\ kip - ft * 12\frac{in}{ft}}{9920\ ksi * 169\ in^3} = 7.75 * 10^{-3}$$

$$E_c = 1820\sqrt{f'_c} = 1820\sqrt{5\ ksi} = 4070 ksi$$

$$\varepsilon_0 = 1.71\frac{f'_c}{E_c} = 1.71 * \frac{5\ ksi}{4070\ ksi} = 0.00210$$

Begin with a guess for neutral axis depth – say 7.5 in. from the top of the section (at the bottom of the deck).

$$c = 7.5\ in$$

Calculate the strain at the top and bottom of the concrete slab

$$\varepsilon_{ct} = \frac{\varepsilon_{1t}^{C} * c}{D - c} = \frac{7.75 * 10^{-3} * 7.5\ in}{27.5i\ n - 7.5\ in} = 0.0029$$

$$\varepsilon_{cb} = \frac{\varepsilon_{1t}^{C} * (c - t_c)}{D - c} = \frac{7.75 * 10^{-3} * (7.5in - 7.5n)}{27.5in - 7.5in} = 0$$

and use these to determine the stress at the top and bottom of the slab

$$f_{ct} = \frac{1.8 * f'_c * {}^{\varepsilon_{ct}}/_{\varepsilon_0}}{1 + \left({}^{\varepsilon_{ct}}/_{\varepsilon_0}\right)^2} = \frac{1.8 * 5\ ksi * {}^{0.0029}/_{0.0021}}{1 + \left({}^{0.0029}/_{0.0021}\right)^2} = 4.27\ ksi$$

$$f_{cb} = \frac{1.8 * f'_c * {}^{\varepsilon_{cb}}/_{\varepsilon_0}}{1 + \left({}^{\varepsilon_{cb}}/_{\varepsilon_0}\right)^2} = \frac{1.8 * 5ksi * {}^{0}/_{0.0021}}{1 + \left({}^{0}/_{0.0021}\right)^2} = 0ksi$$

The current estimate of the neutral axis falls at the interface between the CT girder and the slab, so the compressive force is calculated as

$$C = \frac{1}{2} f_{ct} c b_c = \frac{1}{2}(4.27\ ksi)(7.5\ in)(66\ in) = 1057\ kip$$

The tensile force in the bottom flange is calculated as

$$T = \varepsilon_{1t}^{C} E_{bf} A_{bf} = 7.75 * 10^{-3} * 9920\ ksi * 9.24\ in^2 = 710\ kip$$

The compressive force exceeds the tensile force. Therefore, the initial guess for neural axis depth is too low. Iterate with a lower neutral axis – say:

$$c = 4\ in$$

Following the same procedure:

$$\varepsilon_{ct} = \frac{\varepsilon_{1t}^{C} * c}{D - c} = \frac{7.75 * 10^{-3} * 4\ in}{27.5\ in - 4i\ n} = 0.0013$$

$$\varepsilon_{cb} = \frac{\varepsilon_{1t}^{C} * (c - t_c)}{D - c} = \frac{7.75 * 10^{-3} * (4\ in - 7.5\ in)}{27.5\ in - 4\ in} = -0.0012$$

$$f_{ct} = \frac{1.8 * f'_c * {}^{\varepsilon_{ct}}/_{\varepsilon_0}}{1 + \left({}^{\varepsilon_{ct}}/_{\varepsilon_0}\right)^2} = \frac{1.8 * 5\ ksi * {}^{0.0013}/_{0.0021}}{1 + \left({}^{0.0013}/_{0.0021}\right)^2} = 4.05\ ksi$$

$$f_{cb} = 0ksi$$

(concrete is assumed to carry no tension)

The neutral axis falls within the slab. Therefore,

$$C = \frac{1}{2} f_{ct} c b_c = \frac{1}{2}(4.05\ ksi)(4i\ n)(66\ in) = 535\ kip$$

The tensile force now exceeds the compressive force. Continue iterating by bisection:

Iteration	c (in.)	ε_{ct}	ε_{cb}	f_{ct} (ksi)	f_{cb} (ksi)	C (kip)	$T - C$ (kip)
1	7.5	0.0029	0	4.27	0	1057	-347
2	4	0.0013	-0.0012	4.05	0	535	175
3	5.75	0.0020	-0.0006	4.50	0	853.62	-143
4	4.88	0.0017	-0.0009	4.38	0	705	5.04

For a neutral axis depth of 4.88 in., the difference between tensile and compressive forces is acceptably small. Therefore, internal force equilibrium is achieved. Because the neutral axis depth is below the bottom of the slab, the moment capacity can now be calculated as:

$$M_2 = \varepsilon_{1t}^c E_{bf} A_{bf} \left(D - \frac{t_{bf}}{2} - \frac{c}{3}\right)$$

$$= 7.75 * 10^{-3} * 9920\ ksi * 9.24\ in^2 * \left(27.5\ in - \frac{0.84\ in}{2} - \frac{4.88\ in}{3}\right)$$

$$= 18080\ kip - in = 1510\ kip - ft$$

Checking for compression control,

$$0.85 f'_c b_c \beta_1 c^2 + 0.003 A_{bf} E_{bf} c - 0.003 A_{bf} E_{bf} \left(D - \frac{t_{bf}}{2}\right) = 0$$

Solving,

$$c = 5.18\ in$$

$$\varepsilon_{bf} = 0.003 * \frac{D - c - {t_{bf}}/{2}}{c}$$

$$= 0.003 * \frac{27.5\ in - 5.18\ in - {0.84\ in}/{2}}{5.81\ in} = 0.0113 > \varepsilon_{1t}^{C}$$

The section cannot be compression controlled as concrete cannot reach crushing strain before FRP rupture.

$$\phi M_{nf}^{C} = 0.75 * 1510\ kip - ft = 1130\ kip - ft$$

As can be seen, both methods lead to adequate designs. However, the detailed method leads to a composite moment capacity 23% greater than the simplified method.

Appendix C: Shear Buckling Design Chart Development

In creation of a guide specification for the design of hybrid FRP CT girders, web shear – in particular web shear buckling resistance – remains difficult to capture and describe. Due to the orthotropic nature of FRP and the inclusion of a foam core web, standard analytical solutions for shear buckling of isotropic plates are inadequate. Additionally, little experimental data are available on web buckling. Therefore, to establish a preliminary design basis, numerical simulation by finite element analysis is appropriate. This appendix documents the development of the models used to create empirical buckling curves for CT girder webs which, when combined with appropriate load and resistance design bases, can be used in design.

To establish an accurate baseline from which more complex models could be developed, a basic model was first created for which analytical solutions exist and with which comparisons can be made. To this end, a simply supported, homogeneous plate with isotropic material properties, square plane dimensions, and a total thickness small enough to ensure plane stress assumptions would remain accurate was assessed. For such a plate, Timoshenko and Gere (1963) give an analytical equation for the critical shear buckling stress resultant:

$$N_{xy,cr} = k\frac{\pi^2 D}{b^2} \tag{B-1}$$

In B-1, the coefficient k captures the plate's boundary conditions (taken here as 9.4 to account for the model's simply supported conditions), D is the plate's flexural rigidity per unit length and b is its height. For the basic model created here (a simply supported plate with 12 in. square plane dimensions, a thickness of 0.1 in., elastic modulus of 29,000 ksi, and Poisson's ratio of 0.3), B-1 leads to a critical shear buckling stress resultant of 1.71 kip/in.

The baseline model used to simulate this analytically comparable model used S8R, quadratic 8-node shell elements with 6 degrees of freedom per node and reduced integration. A relatively fine mesh, shown in Figure C1 on the left, was used, which incorporates 576 elements and 2,015 nodes. This discretization was determined by a mesh refinement study, the results of which can be seen in Figure C2. The nodes on the perimeter of the model were restrained from displacement in the direction normal to the plane of the plate itself to mimic simply supported boundaries, and global stability was ensured by restraining the plate's central node against translation in the plane of the plate and rotation about the axis normal to the plate. Load was applied as a unit shear stress resultant to each of the plate's edges. Using a subspace eigenproblem solver, the predicted shear buckling stress resultant equaled 1.68 k/in (for a 1.5% error), verifying the appropriateness and accuracy of the model. Figure C1 on the right presents the model's predicted, buckled mode shape.

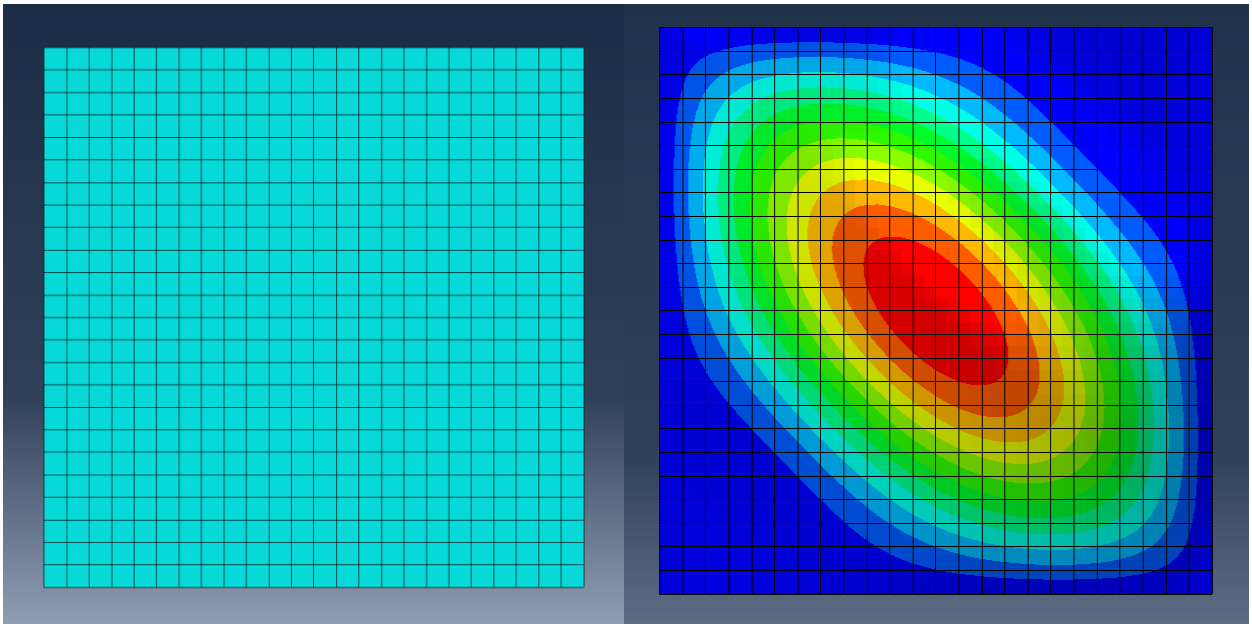

Figure C1: Initial, Isotropic Plate Model: (Left: Element Mesh; Right: Predicted Mode Shape)

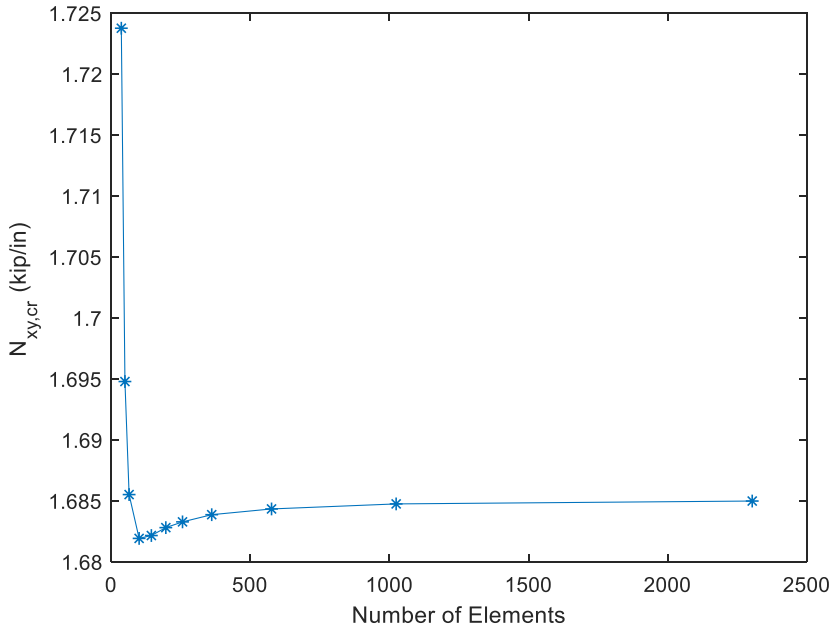

Figure C2: Steel Plate Model Mesh Refinement Study

The first level of complexity added to the model was to use a pseudo-sandwich composite rather than a single plate. The original plate was split into three sections: a thicker "core" modeled discretely with C3D8R 8-node brick elements, and two "face-sheets" again modeled with S8R shell elements. A total of 10,800 elements with 48,739 nodes were used, determined by a mesh refinement study, the results of which can be seen in Figure C3. These elements were assigned the

same isotropic, homogeneous constitutive model as the previous single shell, and were connected to one another using kinematic constraints. The core was given a thickness of 0.08 in. and the face-sheets a thickness of 0.01 in. each, giving a total thickness of 0.1 in. – the same as the initial model. This formed a sandwich composite, although one made from a single, isotropic material which would theoretically behave exactly the same as the uniform plate. The meshed model and predicted buckled shape can be seen in Figure C4.

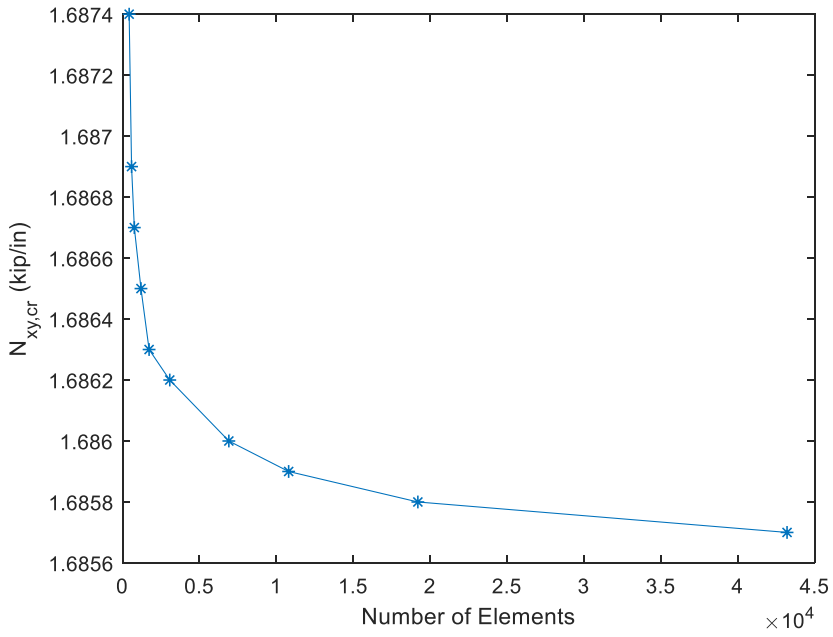

Figure C3: Steel Composite Model Mesh Refinement Study

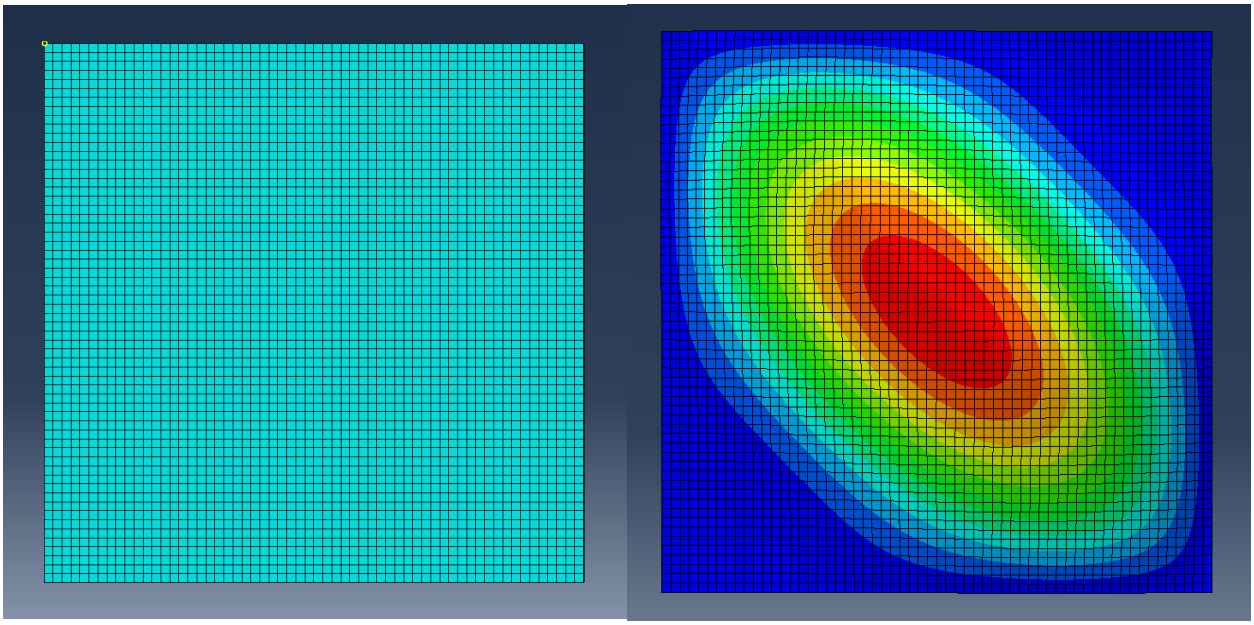

Figure C4: Pseudo-Sandwich Model Predicted Buckled Mode Shape

Loading and boundary conditions were applied to mimic the conditions of a sandwich web section part of a CT girder section. Simple support conditions were enforced by restraining out-of-plane displacement both on the edges of the face sheets and the core. The central node of each face sheet was restrained against displacement in both in-plane directions and against rotation about the normal direction to maintain global stability. Loading was provided by unit shell edge loading on the outside edges of the face sheets. The core and face sheets were kinematically constrained to displace identically, effectively simulating a perfect adhesive bond between them. This modeling scheme with the converged discretization led to a predicted buckling shear stress resultant of 1.69 kip/in., a 1.8% error compared to the analytical solution.

When the ability to match an analytical solution for shear buckling of isotropic plates and equivalent sandwiches was confirmed, a true FRP – foam core sandwich representing a CT girder sandwich web was modeled. Two initial models were produced which emulated thin specimens with 2-layer face sheets and 0.75 in. thick cores (F2C75) and thick specimens with 4-layer face sheets and 1.50 in. thick cores (F4C150). The cores were modeled as isotropic solids with elastic properties of an extruded polyurethane core with an elastic modulus of 15.9 ksi. The face sheets were assigned a composite layup of individual orthotropic 24.2 oz/yd^2 biaxial woven E-glass lamina with elastic moduli of 5340 ksi and 1650 ksi in the 1 and 2 directions, respectively and individual thickness of 0.024 in. oriented at ±45°. It should be noted that each biaxial layer was modeled as two individual, half-thickness uniaxial layers offset by 90°. Plan dimensions were set to 12 in. by 12 in. Mesh refinement studies performed for both models (and presented in Figures C5 and C6) showed that an element size of around 0.375 in. (leading to a mesh density of 4096 and 6144 for the thick and thin models respectively) produced converged predictions of buckling strength.

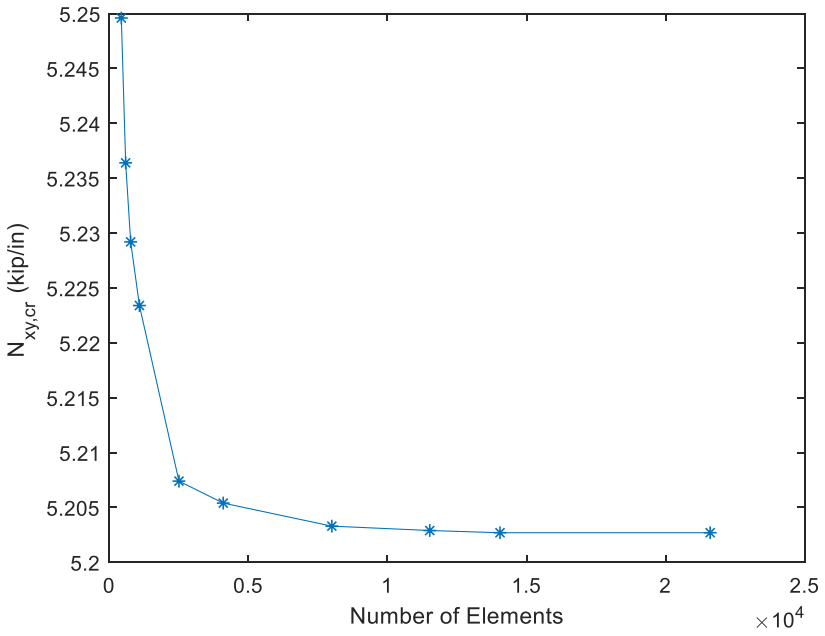

Figure C5: F2C75 Sandwich Mesh Refinement Study

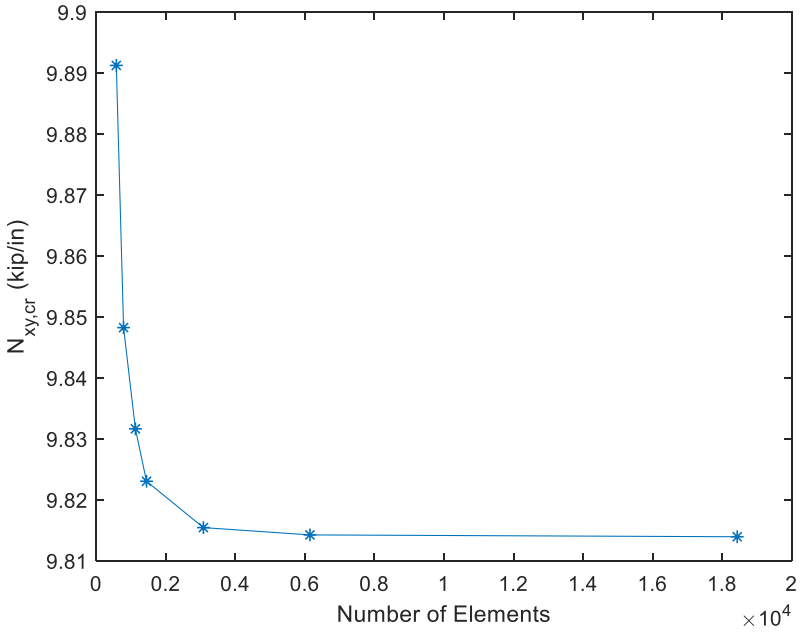

Figure C6: F4C150 Sandwich Mesh Refinement Study

As a theoretical solution to the shear buckling strength of a foam core sandwich composite is not available, an alternative metric was needed by which the models could be verified. Therefore, rather than comparing with theoretical predictions of buckling, the models were used to predict the results of picture frame testing by Schanck et al (2021). To accomplish this, the models were re-

solved using a standard Newton solver and were loaded with the maximum shear stress resultant applied during picture frame testing. Table C1 presents a comparison of measured and predicted in-plane strains for a test specimen identical to the F2C75 model. As can be seen, the predicted strains are reasonable compared to the measured strains considering the numerous simplifications inherent in the models. Additionally, the computed strains are larger than the measured strains. This could be due to the difference in real and assumed boundary conditions and the FRP face sheet modulus being higher than the value used in the simulations, suggesting that predicted shear buckling strengths will be conservative.

Table C1: Comparison of Measured and Predicted Facesheet Strains

Load Response	X - Strain	Y - Strain	Shear Strain
Measured	-4.10e-3	3.50e-3	-5.00e-4
Predicted	-5.88e-3	5.94e-3	2.0e-7

To further validate the models' predictions, the results presented in two previous studies were recreated. In the first study by Oluwabusi and Toubia (2019), a series of FRP sandwich composites were tested using the picture frame method. During this series of tests, two specimens tested failed due to shear buckling at critical shear stress resultants of 2.13 kip/in. and 2.30 kip/in. respectively. Using the geometric and material parameters given by Oluwabusi and Toubia (2019) (12 in. x 12 in. specimens with transformed elastic moduli in the global longitudinal and transverse directions of 2050 ksi), the model presented here predicted buckling corresponding to a shear stress resultant of 2.16 kip/in., very close to the experimentally observed values. In the second study, Pandit et al. (2008) describe a purpose-made, shear deformable finite element for predicting the buckling strength of sandwich plates which, although accurate, is difficult to implement. They used this element to model and analyze the composite sandwich plate analyzed by Yuan and Dawe (2001) using a B-spline finite strip analysis. Pandit et al. (2008) predicted a shear buckling strength of a sandwich composite to be 0.645 kip/in., close to the 0.664 kip/in. from Yuan and Dawe's (2001) finite strip analysis using an example modified from Pearce and Webber (1972). Recreating this, the present model was able to match precisely the 0.664 kip/in. buckling strength reported by Yuan and Dawe (2001).

With the models' validity reasonably confirmed, different parameters' effects on shear buckling were investigated. It is well known that an increase in plate aspect ratio (the ratio of its length to its height) tends to decrease shear buckling load for isotropic plates. In addition, virtually all practical bridge designs with unstiffened webs use girders with web aspect ratios (length to width) exceeding 15. For this reason, a series of buckling analyses were performed on the F2C75 and F4C150 models (with material and thickness properties as given before), with a plan height of 12 in. and increasing aspect ratio from 1:1 to 1:16. The results of these analyses can be seen in

Figures C7 and C8 show that increases in aspect ratio caused decreases in buckling strength. The rate of decrease itself decreased with aspect ratio as well, with a constant buckling strength being approached in the limit. These results suggest that a relatively small aspect ratio (say 5) can characterize the shear buckling strength of sandwich composites of larger aspect ratio. This is fortunate as nearly all practical web designs for slab-on-girder bridges will tend to have aspect ratios greater than 5.

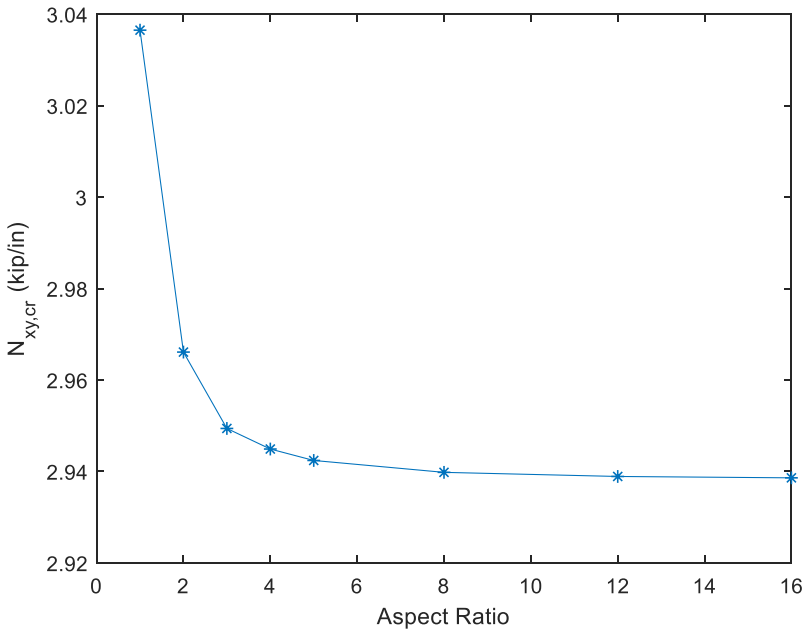

Figure C7: F2C75 Aspect Ratio Study

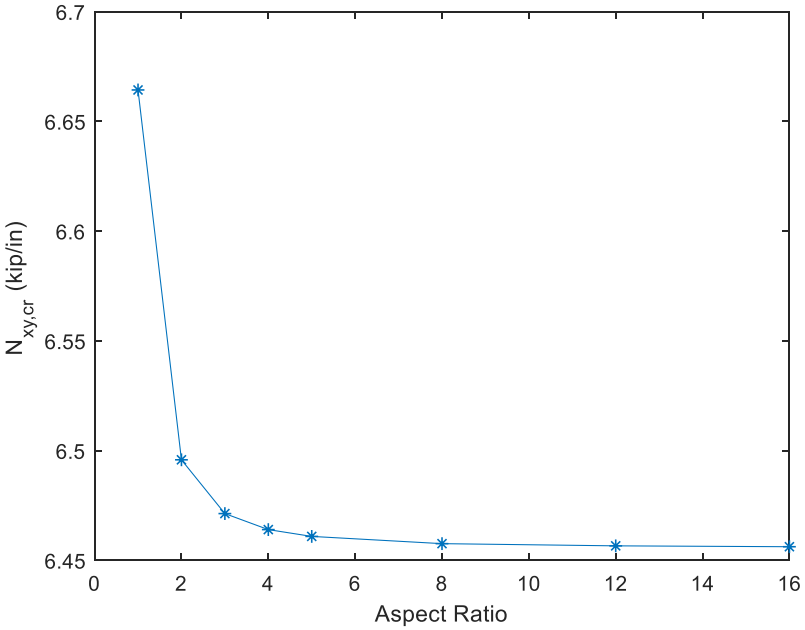

Figure C8: F4C150 Sandwich Aspect Study

With a minimum aspect ratio selected and held constant, other important sandwich web variables, namely web height, core thickness, and face-sheet thickness, were varied to create a series of nomographs quantifying web buckling capacity. These were created to aid in design of sandwich webs for shear buckling as, to date, neither analytical nor empirical expressions have been developed to accurately predict web shear buckling strength. These used the same material properties as noted above and so are not directly applicable to webs of other materials. However, they are typical of the sandwich webs used for CT girders designed and manufactured to date. For 5 web heights, 7 face sheet thicknesses were analyzed, each with 12 different core thicknesses, leading to a total of 420 analyses.

As these nomographs show, each of the tested parameters – web height, core thickness, and facesheet thickness affected the web's shear stability. As expected, increases in facesheet and core thickness led to increases in critical buckling load, whereas increases in web depth led to decreases in buckling load. These nomographs are useful in design, especially when a web height has already been established. For a given web height, a core and facesheet thickness can be chosen to provide adequate material strength and buckling can be checked using the appropriate nomograph. For web heights between these nomographs, linear interpolation may be used with face sheet and core thickness held constant.

Appendix D: Shear Design Examples

D.1 Example 1

The CT girder from the first flexural design example is now designed for shear resistance. Factored maximum shear at the support of the 75 foot span $V_u = 256\ kip$.

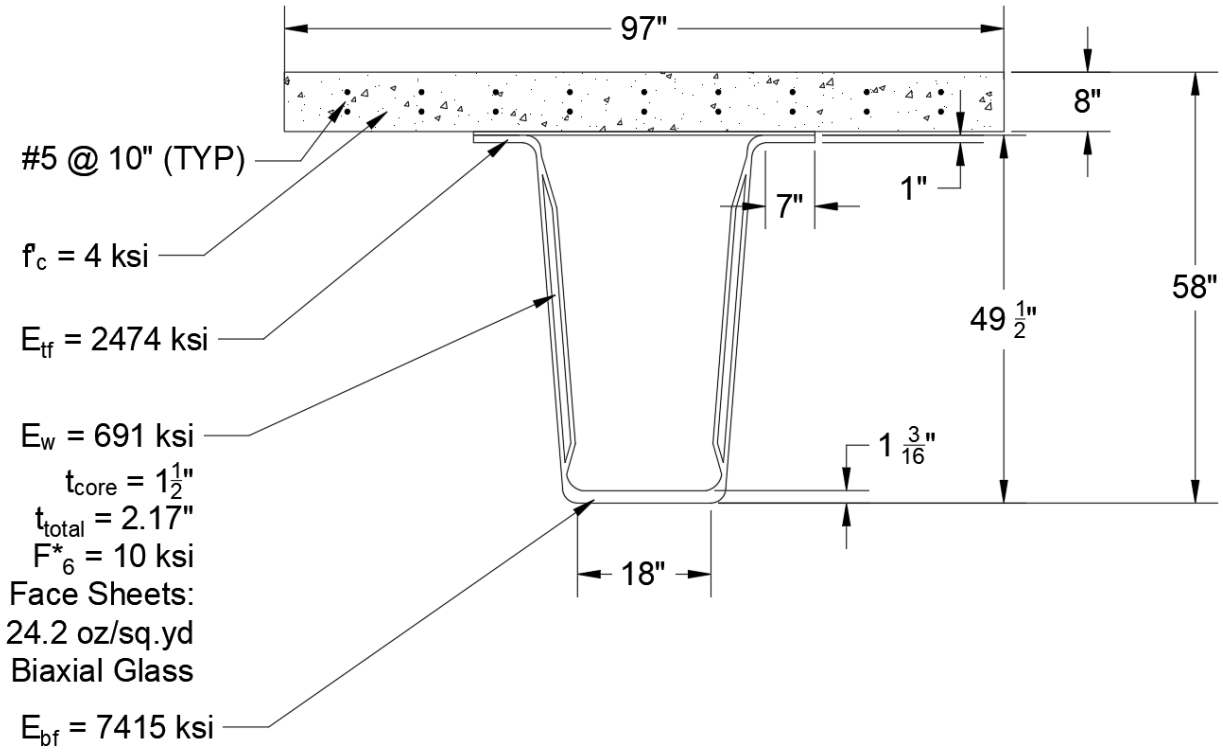

The web shear strength is found by applying the environmental degradation factor to the base-level shear strength:

$$f_6 = f_6^* * C_E = 10\ ksi * 0.65 = 6.5\ ksi$$

Nominal shear resistance is then found as:

$$V_n = \frac{I_c t_{w-fs} f_{6w}}{Q_t} = \frac{153300\ in^4 * 1.344\ in * 6.5\ ksi}{3111\ in^3} = 431\ kip$$

The factored shear resistance is therefore:

$$V_r = \phi V_n = 0.75 * 431\ kip = 323\ kip$$

In addition to the section's shear strength, its resistance to shear buckling must also be investigated. The most appropriate nomograph is that for a web height of 48 in. (the actual web height is 47.3 in., very close to 48 in.). The ratio of core thickness to web thickness is $^{1.5\ in}/_{2.17\ in} = 0.691$, and the face sheet thickness is $^{(2.17\ in - 1.5\ in)}/_{2} = 0.335\ in$:

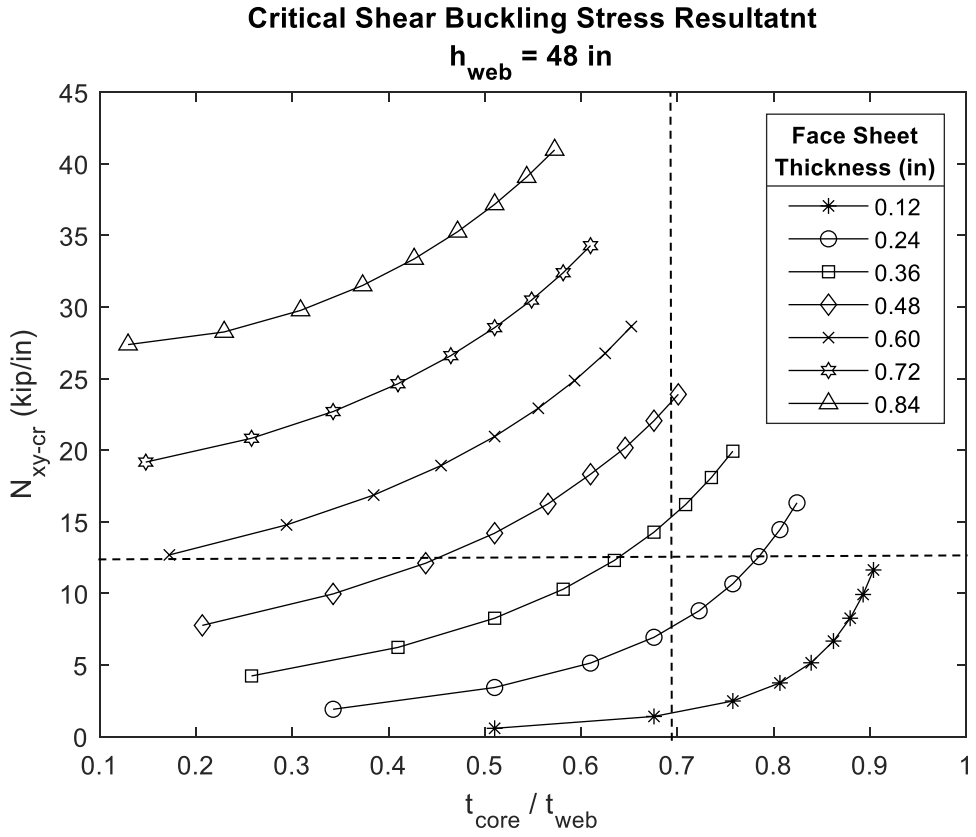

Reading from the nomograph, $N_{xy-cr} = 12.0\ kip/in$. The factored shear buckling resistance is therefore:

$$V_r = \phi N_{xy-cr} * h_{web} * 2 = 0.35 * 12\ \frac{kip}{in} * 47.3\ in * 2 = 397\ kip$$

Shear strength controls the design but both failure modes exceed shear demand. The section is adequate in shear.

D.2 Example 2

The CT girder from the second flexural design example is now designed for shear resistance. Factored non-composite maximum shear at the support of the 38 foot span $V_u = 136\ kip$.

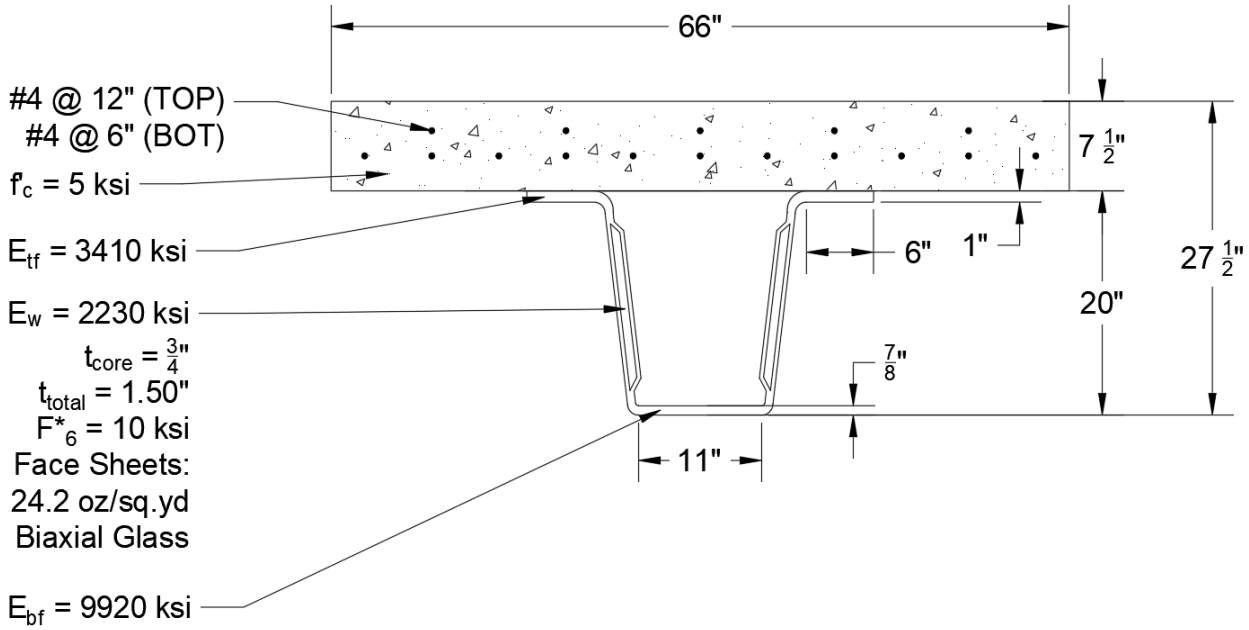

The web shear strength is found by applying the environmental degradation factor to the base-level shear strength:

$$f_6 = f_6^* * C_E = 10\ ksi * 0.65 = 6.5\ ksi$$

Nominal shear resistance is then found as:

$$V_n = \frac{I_c t_{w-fs} f_{6w}}{Q_t} = \frac{17200\ in^4 * 1.50\ in * 6.5\ ksi}{890\ in^3} = 188\ kip$$

The factored shear resistance is therefore:

$$V_r = \phi V_n = 0.75 * 188\ kip = 141\ kip$$

In addition to the section's shear strength, its resistance to shear buckling must also be investigated. Since the nomograph for the smallest web size available is 24 in, use extrapolation. The ratio of core thickness to web thickness is ${}^{0.75\ in}/_{1.5\ in} = 0.5$, and the face sheet thickness is ${}^{(1.5\ in - 0.75\ in)}/_{2} = 0.375\ in$:

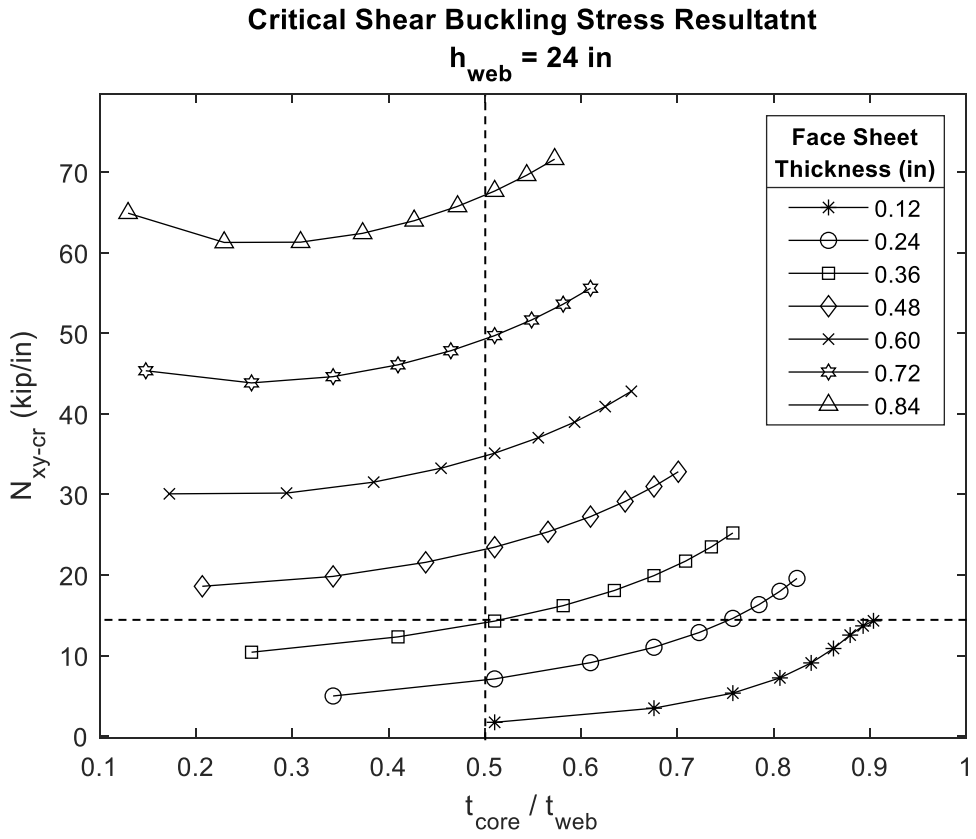
Critical Shear Buckling Stress Resultatnt
h_web = 24 in
Face Sheet Thickness (in)
0.12
0.24
0.36
0.48
0.60
0.72
0.84
N_xy-cr (kip/in)
t_core / t_web
0
10
20
30
40
50
60
70
0.1
0.2
0.3
0.4
0.5
0.6
0.7
0.8
0.9
1

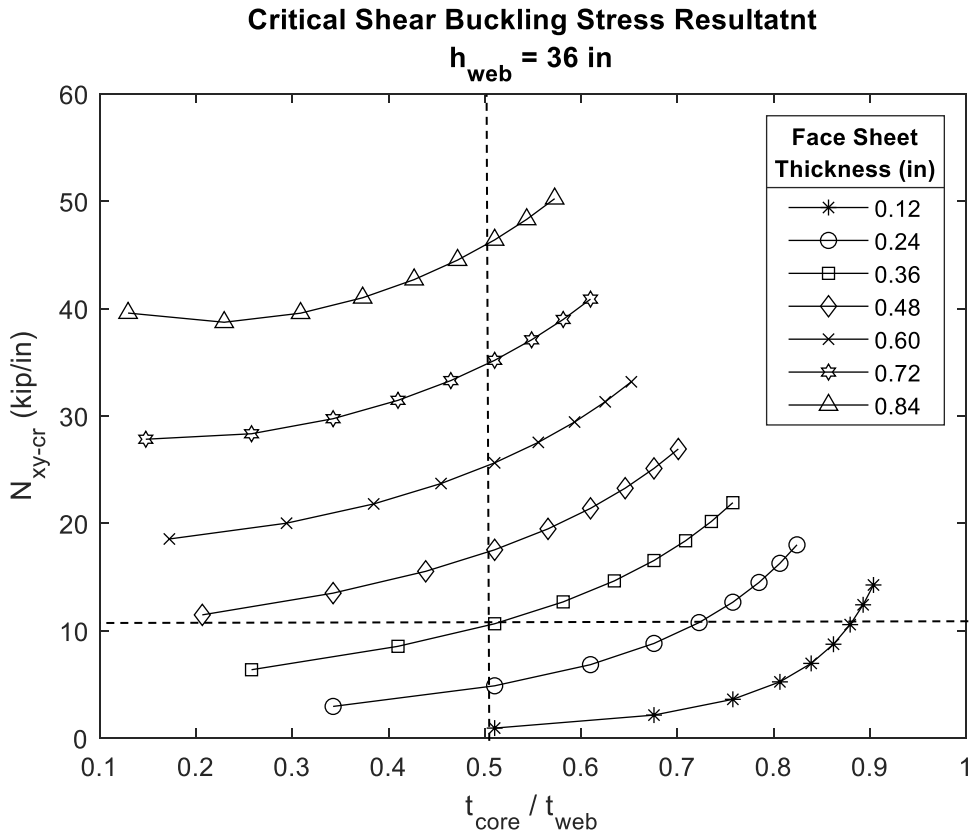
Critical Shear Buckling Stress Resultatnt
h_web = 36 in
Face Sheet Thickness (in)
0.12
0.24
0.36
0.48
0.60
0.72
0.84
N_xy-cr (kip/in)
t_core / t_web
0
10
20
30
40
50
60
0.1
0.2
0.3
0.4
0.5
0.6
0.7
0.8
0.9
1

$$N_{xy-cr} = \frac{15\ \frac{kip}{in} - 10.5\ \frac{kip}{in}}{(36\ in - 24\ in)} * (36\ in - 18.13\ in) + 15\ \frac{kip}{in} = 21.7\ \frac{kip}{in}$$

The factored shear buckling resistance is therefore:

$$V_r = \phi N_{xy-cr} * h_{web} * 2 = 0.35 * 21.7\ \frac{kip}{in} * 18.13\ in * 2 = 275\ kip$$

Shear strength controls the design but both failure modes exceed shear demand. The section is adequate in shear.

Appendix E: References Cited in Appendices

Davids, W.G., Dagher, H.J, & Breton, J. (2000). Modeling creep deformations of FRP-reinforced glulam beams. *Wood and Fiber Science*. 32(4): 426-441.

Davids, W.G. (2001). Nonlinear analysis of FRP-glulam-concrete beams with partial composite action. *Journal of Structural Engineering*. 127(8): 967-971.

Diba, A. & Hepler I. (2019). *Milestone 12: Structural testing of first prototype*. University of Maine, Orono, ME.

Kara, I.F., & Ashour, A.F. (2013). Moment redistribution in continuous FRP reinforced concrete beams. *Construction and Building Materials*. 49(2013): 939-948.

Kwak, H.G., & Kim, S.P. (2002). Nonlinear analysis of RC beams based on moment-curvature relation. *Computers and Structures*. 80(2002): 615-628.

Lou, T., & Xiang, Y. (2006). Finite element modeling of concrete beams prestressed with external tendons. *Engineering Structures*. 28:1919-1926,

Oluwabusi, O.E. & Toubia, E.A. (2019). In-plane shear characterization of composite GFRP-foam sandwich panels. *Journal of Composites for Construction*. 25(5).

Pearce, T.R., & Webber, J.P.H. (1974). Buckling of sandwich panels with laminated faceplates. *Aeronautical Quarterly*. 23(1974): 148-160.

Pandit, M.K., Singh, B.N., & Sheikh, A.H. (2008). Buckling of laminated sandwich plates with soft core based on an improved higher order zigzag theory. *Thin-Walled Structures*. 46(2008): 1183-1191.

Schanck, A. P., & Davids, W.G. (2020). Capacity assessment of older t-beam bridges by nonlinear proxy finite element analysis. *Structures*. 23:267-278.

Schanck, A. & Davids, W. (2021). Flexural load-rating of slab-on-girder bridges by nonlinear proxy finite-element analysis. *Journal of Structural Integrity and Maintenance*. 6(4):209-222.

Timoshenko, S.P. & Gere J.M. (1963). *Theory of Elastic Stability*. McGraw-Hill, London.

Yuan, W.X. & Dawe, D.J. (2001). Overall and local buckling of sandwich plates with laminated faceplates, part II: Applications. *Computational Methods in Applied Mechanical Engineering*. 190(2001): 5215-5131.